University of Alberta

Evaluation of Functional MRI at 4.7 Tesla

by

Ms. Farnaz Khosrow-Khavar©

A thesis submitted to the Faculty of Graduate Studies and Research
in partial fulfillment of the requirements for the degree of **Master of Science**

in

Biomedical Engineering

Edmonton, Alberta
Fall 2007

Library and
Archives Canada

Published Heritage
Branch

395 Wellington Street
Ottawa ON K1A 0N4
Canada

Bibliothèque et
Archives Canada

Direction du
Patrimoine de l'édition

395, rue Wellington
Ottawa ON K1A 0N4
Canada

Your file Votre référence
ISBN: 978-0-494-33277-1
Our file Notre référence
ISBN: 978-0-494-33277-1

NOTICE:
The author has granted a non-exclusive license allowing Library and Archives Canada to reproduce, publish, archive, preserve, conserve, communicate to the public by telecommunication or on the Internet, loan, distribute and sell theses worldwide, for commercial or non-commercial purposes, in microform, paper, electronic and/or any other formats.

The author retains copyright ownership and moral rights in this thesis. Neither the thesis nor substantial extracts from it may be printed or otherwise reproduced without the author's permission.

AVIS:
L'auteur a accordé une licence non exclusive permettant à la Bibliothèque et Archives Canada de reproduire, publier, archiver, sauvegarder, conserver, transmettre au public par télécommunication ou par l'Internet, prêter, distribuer et vendre des thèses partout dans le monde, à des fins commerciales ou autres, sur support microforme, papier, électronique et/ou autres formats.

L'auteur conserve la propriété du droit d'auteur et des droits moraux qui protège cette thèse. Ni la thèse ni des extraits substantiels de celle-ci ne doivent être imprimés ou autrement reproduits sans son autorisation.

In compliance with the Canadian Privacy Act some supporting forms may have been removed from this thesis.

While these forms may be included in the document page count, their removal does not represent any loss of content from the thesis.

Conformément à la loi canadienne sur la protection de la vie privée, quelques formulaires secondaires ont été enlevés de cette thèse.

Bien que ces formulaires aient inclus dans la pagination, il n'y aura aucun contenu manquant.

Canada

اندک اندک جمع مستان میرسند

اندک اندک می پرسدان میرسند

اندک اندک جمع مستان میرسند

اندک اندک می پرسدان میرسند

دل نوازان ناز نازان در رهند

گل گذاران از گلستان میرسند

مولانا جلال الدین محمد رومی
By: Jalaluddin Rumi

To my beloved parents,
Faramarz and Narges Khosrow-Khavar,
Whose infinite love and support has made this possible.

Abstract

The objective of this thesis was to implement and test functional MRI (fMRI) protocol at 4.7T to show the (dis)advantages of fMRI studies at high field. Echo planar imaging sequence was modified and optimized (hardware/software) for the best achievable image quality and fMRI results. Three paradigms were designed to test fMRI performance in (in)homogeneous brain regions. The experiments were replicated at 1.5T. The results show an increase in BOLD signal change and BOLD contrast-to-noise ratio (CNR) in the primary visual cortex, the inferior frontal lobe (BA 44, 45, 47) and fusiform gyrus area at 4.7T. Thus high field fMRI is advantageous when the signal-to-noise ratio (SNR) loss is not severe in the activation region. In the most anterior frontal lobe regions (very inhomogeneous region), no net gain in BOLD CNR may be expected unless shimming is constrained to a local region to minimize intravoxel dephasing and compensate for SNR.

Acknowledgments

I would like to thank my supervisor, Dr. Alan Wilman for his great outlook on the project, in allowing me to independently develop my ideas and for giving me guidance whenever I dropped by his office unexpectedly. His generosity and constant encouragement when failure seemed inevitable is greatly appreciated. He is beyond doubt the best supervisor and mentor one can ask for.

My acknowledgements go to Maisie Goh and Karim Damji for immaculate maintenance of the BME/NMR centers; Changho Choi, Marc Lebel and Peter Seres for assistant with the magnets. Many thanks go to the BME graduate students who consistently volunteered for my fMRI studies especially Beau Sapach, Jacob Ellegood, Rob Stobbe, Luis Concha and David McAllindon. I would also like to recognize the great friends I made in these two years, namely Angela Leung, Beau Sapach, Behnaz Attaeian, Cheryl Porter, Dr. Kelvin Jones, Gaolang Gong, Gritchi Castro, Yi Mao and Yusuf Bhagat.

Above all, I would like to thank my parents for providing me with the opportunity to get the best education possible, for the numerous sacrifices they have made over the years and for giving me support throughout my life. I am indefinitely grateful for the endless love they have given me. My love also goes to my brothers for always lending me a listening ear and giving me encouragement. I am truly fortunate to be part of this caring family and I thank them from the bottom of my heart.

Table of Contents

1 INTRODUCTION **1**

1.1 SCOPE OF THESIS 2
REFERENCES 3

2 PHYSICS OF MAGNETIC RESONANCE IMAGING **4**

2.1 NUCLEAR MAGNETIC RESONANCE (NMR) 4
2.2 STAGES OF NMR 5
2.2.1 Preparation *5*
2.2.2 Excitation *8*
2.2.3 Acquisition *9*
2.3 RELAXATION 10
2.3.1 Longitudinal Relaxation (T1) *10*
2.3.2 Transverse Relaxation *11*
2.3.3 Contrast Mechanism *15*
2.4 ECHO FORMATION 16
2.4.1 Spin Echo (SE) *16*
2.4.2 Gradient-recalled Echo (GRE) *17*
2.5 IMAGING 18
2.5.1 Spatial Encoding *19*
2.5.2 Slice-select Encoding *20*
2.5.3 2D Fourier Imaging *22*
2.6 2D FOURIER TRANSFORM RECONSTRUCTION 23
2.7 K-SPACE 24
2.7.1 Sampling Requirements *25*
2.8 CONCLUSIONS 29
REFERENCES 30

3 FUNCTIONAL MAGNETIC RESONANCE IMAGING **32**

3.1 PHYSIOLOGICAL BASIS OF FMRI 32
3.1.1 Hemodynamic Response Function *33*
3.2 THE BOLD EFFECT 34
3.2.1 Historical Overview *34*
3.2.2 The Physical Basis of the BOLD Effect *35*
3.2.3 Functional Activation Maps *37*
3.3 THE BOLD EFFECT COMPONENTS 37
3.3.1 The Extravascular Effect *38*
3.3.2 Diffusion *38*
3.3.3 The Intravascular Effect *40*
3.4 FIELD STRENGTH AND THE BOLD EFFECT 40
3.5 CONCLUSIONS 42
REFERENCES 43

4 SINGLE-SHOT ECHO PLANAR IMAGING 46
4.1 CONVENTIONAL IMAGING 46
4.1.1 *Echo Planar Imaging (EPI)* *47*
4.2 EPI SEQUENCE VARIATIONS 48
4.2.1 *Gradient-echo EPI* *48*
4.2.2 *Spin-echo EPI* *48*
4.3 EPI ARTIFACTS 49
4.3.1 *Nyquist Ghosting* *49*
4.3.2 *Low-bandwidth Artifacts* *52*
4.3.3 *Constant Gradient Offset* *56*
4.3.4 *Chemical Shift* *58*
4.3.5 *T2* decay* *58*
4.4 EPI ACQUISITION PARAMETERS AT 4.7T 60
4.4.1 *Acquisition time* *60*
4.4.2 *B_o (in)homogeneity* *66*
4.4.3 *B_1 (In)homogeneity* *72*
Echo train adjustment using preparation reference scans *75*
4.5 EPI IMAGE RECONSTRUCTION WITH A REFERENCE SCAN 76
4.5.1 *Method 1: Linear Phase Correction* *76*
4.5.2 *Method 2: Nonlinear Phase Correction* *79*
4.5.3 *Comparison between the Linear and Nonlinear Phase Corrections* *80*
4.5.4 *Reconstruction Summary* *81*
4.6 CONCLUSIONS 82
REFERENCES 83

5 FMRI IMAGING AND ANALYSIS METHODS 85
5.1 IMAGING TECHNIQUE 85
5.2 PARAMETER OPTIMIZATION AT 4.7T 86
5.2.1 *Echo time (TE)* *86*
5.2.2 *Time of Repetition (TR)* *87*
5.2.3 *Voxel dimensions* *88*
5.3 PARADIGM DESIGN 88
5.4 DATA ANALYSIS 89
5.4.1 *SPM5 Statistical Software* *89*
5.4.2 *Summary* *96*
5.5 CONCLUSIONS 97
REFERENCES 98

6 EVALUATION OF FMRI AT 4.7T 99
6.1 METHOD 100
6.1.1 *Imaging Equipment* *100*
6.1.2 *Functional Imaging* *100*
6.2 RESULTS 106
6.2.1 *Flashing checkerboard* *106*

6.2.2 Verbal Fluency *112*
6.2.3 Face Perception *118*
6.3 DISCUSSION 124
6.3.1 Flashing checkerboard *124*
6.3.2 Verbal fluency task *125*
6.3.3 Face Perception *126*
6.4 CONCLUSIONS 127
REFERENCES 128

7 CONCLUSIONS AND FUTURE DIRECTIONS **131**

REFERENCES 134

APPENDIX A: EPI RECONSTRUCTION **136**

METHOD 1: NONLINEAR IMAGE RECONSTRUCTION 136
METHOD 2: LINEAR AND CONSTANT IMAGE RECONSTRUCTION 139

APPENDIX B: FILE CONVERSIONS **143**

APPENDIX C: FMRI PARADIGMS **145**

FLASHING CHECKERBOARD 145
FACE PERCEPTION 146

APPENDIX D: BOLD SIGNAL CHANGE CALCULATIONS **148**

LIST OF TABLES

TABLE 2.1.1: LIST OF USEFUL NMR NUCLEI. 5

TABLE 2.3.1: T_1 VALUES FOR DIFFERENT TISSUE TYPES AT 1.5T. 11

TABLE 2.3.2: T_2 VALUES FOR DIFFERENT TISSUE TYPES AT 1.5T. 13

TABLE 3.2.1: MAGNETIC SUSCEPTIBILITY VALUES FOR DIFFERENT MATERIAL. 36

TABLE 4.4.1: 4X4MM RESOLUTION. 61

TABLE 4.4.2: 2X4MM RESOLUTION. 61

TABLE 4.4.3: EPI ACQUISITION TIME PER DATA POINT WITH AND WITHOUT RAMP-SAMPLING. 61

TABLE 4.4.4: R.F. PULSE LENGTHS REQUIRED FOR THE LISTED SLICE THICKNESSES (CONSIDERING A MAXIMUM SLICE-SELECT GRADIENT OF 3.5G/CM). 70

TABLE 4.4.5: GHOST INTENSITY (%) FOR A/P AND L/R PHASE-ENCODES. 71

TABLE 4.4.6: RF WAVELENGTH AS A FUNCTION OF STATIC MAGNETIC FIELD FOR INVIVO BRAIN. 72

TABLE 6.2.1: AVERAGE BOLD SIGNAL CHANGE (%) IN AN 8MM (RADIUS) SPHERE IN THE V1. 106

TABLE 6.2.2: SNR CALCULATIONS FOR A ROI IN THE PRIMARY VISUAL CORTEX. 109

TABLE 6.2.3: ΔR_2^* (S^{-1}) CALCULATIONS IN THE PRIMARY VISUAL CORTEX. 110

TABLE 6.2.4: BOLD CNR CALCULATIONS IN THE PRIMARY VISUAL CORTEX. 111

TABLE 6.2.5: AVERAGE BOLD SIGNAL CHANGE (%) IN A 4MM (RADIUS) SPHERE IN THE LEFT IFG. ALSO INCLUDED ARE THE BUTTON RESPONSES, OUTLINED BELOW EACH SESSION CORRESPONDINGLY. 112

TABLE 6.2.6: SNR CALCULATIONS FOR A ROI IN THE INFERIOR FRONTAL LOBE (ACTIVATION REGION). 113

TABLE 6.2.7: SNR CALCULATIONS FOR A ROI IN THE MOST ANTERIOR-INFERIOR FRONTAL LOBE. 113

TABLE 6.2.8: SNR CALCULATIONS FOR A ROI IN THE POSTERIOR-INFERIOR REGIONS. 114

TABLE 6.2.9: ΔR_2^* (s^{-1}) CALCULATIONS IN THE FRONTAL LOBE. 117

TABLE 6.2.10: BOLD CNR CALCULATIONS IN THE FRONTAL LOBE. 117

TABLE 6.2.11: AVERAGE BOLD SIGNAL CHANGE (%) IN A 2MM (RADIUS) SPHERE IN THE RIGHT FFA. 118

TABLE 6.2.12: AVERAGE BOLD SIGNAL CHANGE (%) IN A 2MM (RADIUS) SPHERE IN THE LEFT FFA. 119

TABLE 6.2.13: SNR CALCULATIONS FOR A SLICE LOCATED IN THE RIGHT FFA. 122

TABLE 6.2.14: SNR CALCULATIONS FOR A SLICE LOCATED IN THE LEFT FFA. 122

TABLE 6.2.15: ΔR_2^* (s^{-1}) CALCULATIONS IN THE RIGHT FFA. 122

TABLE 6.2.16: ΔR_2^* (s^{-1}) CALCULATIONS IN THE LEFT FFA. 123

TABLE 6.2.17: BOLD CNR CALCULATIONS IN THE RIGHT FFA. 123

TABLE 6.2.18: BOLD CNR CALCULATIONS IN THE LEFT FFA. 123

List of Figures

FIGURE 2.2.1: SPINS IN THERMAL EQUILIBRIUM WITH NO NET MAGNETIZATION. 5

FIGURE 2.2.2: PREPARATION PHASE. 5

FIGURE 2.2.3: POPULATION DISTRIBUTION OF NUCLEAR SPINS AFTER APPLICATION OF B_O. 6

FIGURE 2.2.4: THE NET MAGNETIZATION VECTOR (M_Z) IN THE PRESENCE OF B_O. 7

FIGURE 2.2.5: NUCLEAR SPINS PRECESSION ABOUT B_O AT AN ANGLE. 7

FIGURE 2.2.6: B_1 TIPS M_Z INTO THE TRANSVERSE PLANE IN A SPIRAL TRAJECTORY.. 8

FIGURE 2.2.7: M_{XY} PRECESSION RESULTS IN AN OSCILLATING MAGNETIC FIELD WHICH INDUCES A SINUSOIDAL EMF IN A WIRE LOOP KNOWN AS AN R.F. COIL. 9

FIGURE 2.2.8: A SINUSOIDAL SIGNAL WITH FREQUENCY Ω_O IN THE TIME DOMAIN IS REPRESENTED AS AN IMPULSE FUNCTION CENTERED ON Ω_O. A DECAYING SINUSOIDAL SIGNAL (EMF) IS REPRESENTED AS A BROADENED IMPULSE FUNCTION. 9

FIGURE 2.3.1: T_1-RELAXATION PROCESS. 10

FIGURE 2.3.2: T_1 VALUES FOR DIFFERENT TISSUE TYPES PROVIDE A SOURCE OF IMAGE CONTRAST. 11

FIGURE 2.3.3: SPINS PRECESSION WITH DIFFERENT FREQUENCIES. 12

FIGURE 2.3.4: T_2-RELAXATION PROCESS. 13

FIGURE 2.3.5: T_2 VALUES FOR DIFFERENT TISSUE TYPES PROVIDE A SOURCE OF IMAGE CONTRAST. 14

FIGURE 2.3.6: COMPARISON BETWEEN T_2 AND T_2* DECAY RATES. 15

FIGURE 2.3.7: LEFT: T_1-WEIGHTED, RIGHT: T_2-WEIGHTED. 15

FIGURE 2.4.1: APPLICATION OF A 180° R.F. PULSE REFOCUSES STATIC DEPHASING..... 16

FIGURE 2.4.2: SPIN-ECHO FORMATION. 17

FIGURE 2.4.3: APPLICATION OF 180° R.F. PULSES REFOCUSES THE STATIC FIELD INHOMOGENEITIES. 17

FIGURE 2.4.4: GRADIENT-RECALLED ECHO FORMATION. 18

FIGURE 2.5.1: A GRADIENT FIELD APPLIED IN THE B_0 DIRECTION BUT VARYING IN THE X DIRECTION. 19

FIGURE 2.5.2: A GRADIENT FIELD CHANGES THE INSTANTANEOUS FREQUENCY OF THE SIGNAL. 19

FIGURE 2.5.3: SLICE SELECTION. 20

FIGURE 2.5.4: THE FREQUENCY BANDWIDTH OF THE R.F. PULSE IS LINEARLY PROPORTIONAL TO THE SLICE THICKNESS. 21

FIGURE 2.5.5: MODULATING THE R.F. PULSE TIME-VARYING ENVELOPE RESULTS IN THE DESIRED FREQUENCY PROFILE. 22

FIGURE 2.7.1: A TRANSVERSE SLICE OF THE HUMAN BRAIN AND THE CORRESPONDING RAW K-SPACE DATA.. 25

FIGURE 2.7.2: THE RANGE OF FREQUENCIES IN THE FREQUENCY AND PHASE-ENCODE DIRECTIONS IS DEFINED BY THE FIELD OF VIEW. 25

FIGURE 2.7.3: CONVENTIONAL GRADIENT-ECHO K-SPACE TRAJECTORY. 27

FIGURE 2.7.4: CONVENTIONAL GRADIENT-ECHO IMAGING SEQUENCE. 27

FIGURE 2.7.5: ECHO PLANAR IMAGING K-SPACE TRAJECTORY. 28

FIGURE 2.7.6: ECHO PLANAR IMAGING SEQUENCE. 28

FIGURE 3.1.1: SUMMARY CHART OF PHYSIOLOGICAL/METABOLIC CHANGES THAT FOLLOW NEURAL ACTIVITY.. 33

FIGURE 3.1.2: HEMODYNAMIC RESPONSE FUNCTION FOLLOWING NEURAL ACTIVITY.. 33

FIGURE 3.1.3: HRF IN THE PRIMARY VISUAL CORTEX (V1), SUPPLEMENTARY MOTOR AREA (SMA) AND MOTOR CORTEX (M1). 34

FIGURE 3.2.1: PARAMAGNETISM AND DIAMAGNETISM. 36

FIGURE 3.2.2: HB IN A BLOOD VESSEL CREATES A DIPOLE-LIKE MAGNETIC FIELD IN THE TISSUE SPACE AROUND IT DUE TO DIFFERENCES IN MAGNETIC SUSCEPTIBILITY IN THESE TWO REGIONS. 36

FIGURE 3.3.1: FIELD DISTORTIONS AROUND A MAGNETIZED BLOOD VESSEL. A SINGLE MAGNETIZED CYLINDER ORIENTED PERPENDICULARLY TO THE MAGNETIC FIELD B_0 CREATES FIELD OFFSETS (ΔB) IN THE SURROUNDING SPACE, WITH THE FIELD INCREASED ALONG THE MAIN FIELD AXIS AND DECREASED ALONG A PERPENDICULAR AXIS. 38

FIGURE 3.3.2: DIFFUSION PRODUCES AN AVERAGING OVER FIELD OFFSETS THAT IS MORE EFFECTIVE FOR THE SMALLEST VESSELS.. 39

FIGURE 3.3.3: SPIN-ECHO AND GRADIENT-ECHO T_2 AND T_2^* SENSITIVITIES TO VESSELS OF DIFFERENT DIAMETERS. 39

FIGURE 4.1.1: FLOW CHART FOR THE CONVENTIONAL GRADIENT-ENCODE SCHEME. .. 47

FIGURE 4.1.2: FLOW CHART FOR ECHO PLANAR IMAGING SEQUENCE.. 47

FIGURE 4.2.1: GRE-EPI SEQUENCE. 48

FIGURE 4.2.2: SE-EPI SEQUENCE. 49

FIGURE 4.3.1: EVERY OTHER LINE IN K-SPACE IS ACQUIRED WITH A NEGATIVE POLARITY GRADIENT. 50

FIGURE 4.3.2: EDDY CURRENTS CAUSE A CONSTANT PERIODIC TIME-DELAY FOR EVERY SECOND LINE IN K-SPACE WHICH LEADS TO A PERIODIC CRISSCROSS PATTERN AFTER TIME-REVERSAL. 50

FIGURE 4.3.3: A COMPENSATION FIELD REDUCES THE EFFECT OF EDDY CURRENTS ON READOUT FIELD GRADIENTS. 51

FIGURE 4.3.4: THIS ORIGINAL PHANTOM IMAGE SHOWS LARGE SHIFTS BETWEEN ODD AND EVEN LINES, MANIFESTED AS DARK BANDS IN THE IMAGE. 51

FIGURE 4.3.5: ACQUISITION OF A REFERENCE SCAN PRIOR TO THE ACTUAL IMAGE SCAN.. 52

FIGURE 4.3.6: A CORONAL SLICE OF A HUMAN HEAD AND ITS CORRESPONDING PHASE MAP.. 53

FIGURE 4.3.7: CONVENTIONAL GRE IMAGES TAKEN WITH TR: 50MS, 1X1X2MM RESOLUTION, A) TE: 10, B) 20, C) 30 AND D) 40MS. 54

FIGURE 4.3.8: THE PRESENCE OF A NEGATIVE (TOP) OR POSITIVE (BOTTOM) GRADIENT OFFSET DURING READOUT CAUSES SIGNAL LOSS. 55

Figure 4.3.9: Use of oblique slices to avoid brain regions with large magnetic susceptibility differences. 56

Figure 4.3.10: Echo drift in the presence of a 0.015mT/m gradient offset.... 56

Figure 4.3.11: A constant gradient offset causes an increasing echo shift. However, this is not a source of ghosting since the echo shifts are not periodic from line to line. 57

Figure 4.3.12: An uncorrected phantom image (left) and the post-processed image (right). Also shown are Varian Inova 4.7T and Matlab windows of echo drift in the reference scan. 57

Figure 4.3.13: Fat and water Larmor frequencies differ by 3.5ppm in a homogenous field. 58

Figure 4.3.14: The effect of increasing B_0 field inhomogeneity (T_2') on point spread function (*PSF*). 59

Figure 4.3.15: Difference in PSF for GRE (FID) and SE EPI sequences. 59

Figure 4.4.1: Non-uniform time-sampling.. 63

Figure 4.4.3: Zero-filling partial Fourier reconstruction acts as a low-pass filter, causing blurring in the images. 64

Figure 4.4.4: Homodyne Partial-Fourier Reconstruction. 64

Figure 4.4.5: Ramp function. 65

Figure 4.4.6: GRE-EPI images taken with TR/TE = 2000/25ms, 2x4x1.5mm resolution, 75% acquired lines and reconstructed with a) zero-filling and b) homodyne techniques. 65

Figure 4.4.7: A demonstration of poor and acceptable shimming. 66

Figure 4.4.8: Higher order Shims. 66

Figure 4.4.9: Window of manual shimming on Varian Inova 4.7T system. Left: FID signal, Right: power spectrum. 67

Figure 4.4.10: Common defects in line shape caused by mis-adjustment of shim currents. 68

Figure 4.4.11: Adjusting first-order 'z' shim to eliminate beats and nulls in the FID signal. 68

Figure 4.4.12: Adjusting second-order 'z' shim due to the asymmetrical skew of the line in addition to its existence close to the base of the line. The FID in this case decays faster in the first part of the envelope than the later parts. 68

Figure 4.4.13: Adjusting third-order 'z' shim due to symmetric broadening at the base of the line shape. The FID envelope in this case is misleading as its faster initial decay can be categorized as a 'z2' or 'z4' shim. 69

Figure 4.4.14: An example of a proper shim where the FID signal decays slowly, the line shape is symmetric and the bandwidth is below 20Hz. 69

Figure 4.4.15: Conventional GRE images taken with two slice thicknesses at 4.7T with TR/TE: 50/25ms, a: 20°, a) 1x1x8mm b)1x1x2mm with 4 averages. 70

Figure 4.4.16: EPI images taken with 2x4x2mm resolution, a) A/P phase-encode and b) L/R phase-encode 70

Figure 4.4.17: Fitted B_1 field distribution for a transverse slice,. 73

Figure 4.4.18: Fitted flip angle distribution for a transverse slice, calculated from B_1 field map in Figure 4.4.17 73

Figure 4.4.19: Normalized signal intensity profile for a transverse slices, calculated from flip angle distribution in Figure 4.4.18 and Eqn. 56.. 74

Figure 4.4.20: A balanced echo train. 75

Figure 4.4.21: An echo train drift to the right due to a negative background gradient offset. An additional positive gradient field may be applied to the readout refocusing gradient to null the gradient offset. 76

Figure 4.4.22: Large echo shifts between even and odd lines. A delay (ms) may be added initially to ensure echoes are refocused at the center of k-space. 76

Figure 4.5.1: Echo position per k-space line acquired from a subject's reference scan (128x64 resolution) 77

Figure 4.5.2: Constant phase per k-space line acquired from a subject's reference scan.. 78

Figure 4.5.3: An axial slice showing the presence of dark bands and iso-intense ghosts when no phase-corrections are done. 78

FIGURE 4.5.4: NONLINEAR (LEFT) AND LINEAR PHASE CORRECTIONS (RIGHT). 80

FIGURE 4.5.5: NONLINEAR (LEFT) AND LINEAR (RIGHT) PHASE-CORRECTED EPI IMAGES. 80

FIGURE 4.5.6: EPI RECONSTRUCTION METHOD FOR UNIFORM K-SPACE DATA SAMPLING. 81

FIGURE 5.1.1: SUBJECT MOVEMENT BEHAVIOR AS THE FUNCTION OF SCAN TIME, CHARACTERIZED IN 3-D BY TRANSLATION (X,Y,Z) AND ROTATION (PITCH, ROLL, YAW). 86

FIGURE 5.2.1: BOLD CONTRAST AS A FUNCTION OF ECHO TIME WITHIN VESSEL AND TISSUE FOR B) 1.5T AND C) 4T TO ILLUSTRATE THAT MAXIMUM CONTRAST OCCURS AT TE=T_2* IN VESSEL AND TISSUE REGIONS. 87

FIGURE 5.3.1: BLOCK PARADIGM DESIGN. SHOWN IS FIVE CYCLES OF "ON" AND "OFF" PERIOD. 88

FIGURE 5.4.1: SPM5 SNAPSHOT OF REALIGNMENT PROCEDURE.. 90

FIGURE 5.4.2: SMOOTHING PROCESS. 91

FIGURE 5.4.3: GAUSSIAN SMOOTHING KERNEL. 91

FIGURE 5.4.4: SPM5 SNAPSHOT OF THE SMOOTHING PROCEDURE. AN 8MM ISOTROPIC GAUSSIAN KERNEL IS USED FOR TYPICAL EPI VOXEL DIMENSIONS AT 4.7T. 92

FIGURE 5.4.5: SPECIFYING THE ONSET TIMES FOR TASK BLOCKS.. 92

FIGURE 5.4.6: SPECIFYING THE WIDTH OF THE HIGH-PASS FILTER KERNEL IN SECONDS. 93

FIGURE 5.4.7: SPECIFYING THE LOW-PASS FILTER. 93

FIGURE 5.4.8: GENERAL LINEAR MODEL. 94

FIGURE 5.4.9: DESIGN MATRIX IN SPM5 95

FIGURE 5.4.10: SUMMARY OF FMRI DATA PROCESSING AND ANALYSIS. 96

FIGURE 6.1.1: OUTLINES WITH FUNCTIONAL ATTRIBUTION. 101

FIGURE 6.1.2: DIFFERENT BRAIN CORTICES. 101

FIGURE 6.1.3: DIAGRAM OF THE FFA WITH TRANSVERSE AND CORONAL CUTS REVEALING THE SITE OF THIS REGION. 104

FIGURE 6.2.1: SCATTER PLOT SHOWING THE BOLD SIGNAL CHANGE IN THE PRIMARY VISUAL CORTEX ACROSS THE 1.5T AND 4.7T FIELD STRENGTHS FOR SIX SUBJECTS.. 106

FIGURE 6.2.2: FMRI TIME-COURSE FOR THE MOST STATISTICALLY SIGNIFICANT VOXEL IN THE PRIMARY VISUAL CORTEX. SHOWN IS THE BOLD SIGNAL CHANGE AS THE FUNCTION OF SCAN TIME. 108

FIGURE 6.2.3: ACTIVATION MAP (T-STATISTICS) OVERLAID ON EPI IMAGES. THE ACTIVATION MAP IS FROM THE SAME SUBJECT WITH SIMILAR SLICES ACROSS THE THREE IMAGING PROTOCOLS. 109

FIGURE 6.2.4: SCATTER PLOT SHOWING ΔR_2^* IN THE PRIMARY VISUAL CORTEX ACROSS THE 1.5T AND 4.7T FIELD STRENGTHS FOR SIX SUBJECTS. 110

FIGURE 6.2.5: SCATTER PLOT SHOWING BOLD CNR IN THE PRIMARY VISUAL CORTEX ACROSS THE 1.5T AND 4.7T FIELD STRENGTHS. 111

FIGURE 6.2.6: SCATTER PLOT SHOWING THE BOLD SIGNAL CHANGE IN THE LEFT IFG ACROSS THE 1.5T AND 4.7T FIELD STRENGTHS FOR SIX SUBJECTS.. 112

FIGURE 6.2.7: FMRI TIME-COURSE FOR THE MOST STATISTICALLY SIGNIFICANT VOXEL IN THE LEFT IFG. SHOWN IS THE BOLD SIGNAL CHANGE AS THE FUNCTION OF SCAN TIME. 115

FIGURE 6.2.8: ACTIVATION MAP (T-STATISTICS) OVERLAID ON EPI IMAGES. THE ACTIVATION MAP IS FROM THE SAME SUBJECT WITH SIMILAR SLICES ACROSS THE THREE IMAGING PROTOCOLS. THE RED ARROW INDICATES THE ACTIVATION REGION IN THE LEFT IFG. 116

FIGURE 6.2.9: SCATTER PLOT SHOWING ΔR_2^* IN THE LEFT IFG ACROSS THE 1.5T AND 4.7T FIELD STRENGTHS FOR SIX SUBJECTS. 117

FIGURE 6.2.10: SCATTER PLOT SHOWING BOLD CNR IN THE LEFT IFG ACROSS THE 1.5T AND 4.7T FIELD STRENGTHS. 118

FIGURE 6.2.11: : SCATTER PLOT SHOWING THE BOLD SIGNAL CHANGE IN THE RIGHT AND LEFT FFA ACROSS THE 1.5T AND 4.7T FIELD STRENGTHS FOR SIX SUBJECTS. 119

FIGURE 6.2.12: ACTIVATION MAP (T-STATISTICS) OVERLAID ON ACTUAL EPI IMAGES. THE ACTIVATION MAP IS FROM THE SAME SUBJECT WITH SIMILAR SLICES ACROSS THE THREE IMAGING PROTOCOLS. NOTE THAT THE RED ARROW IN THE CORONAL

SLICE INDICATES THE ACTIVATION REGION IN THE RIGHT FUSIFORM GYRUS AREA.. 120

FIGURE 6.2.13: GRE-EPI IMAGES AT 4.7T AND 1.5T. 121

FIGURE 6.2.14: FMRI TIME-COURSE FOR THE MOST STATISTICALLY SIGNIFICANT VOXEL IN THE RIGHT FFA. SHOWN IS THE BOLD SIGNAL CHANGE AS THE FUNCTION OF SCAN TIME. 121

FIGURE 6.2.15: SCATTER PLOT SHOWING ΔR_2^* IN THE RIGHT/LEFT FFA ACROSS THE 1.5T AND 4.7T FIELD STRENGTHS FOR SIX SUBJECTS. 123

FIGURE 6.2.16: SCATTER PLOT SHOWING BOLD CNR IN THE RIGHT/LEFT FFA ACROSS THE 1.5T AND 4.7T FIELD STRENGTHS. 124

List of Symbols

$\mathbf{B_o}$	static magnetic field
$\mathbf{B_1}$	radio frequency field
$\mathbf{B_{eff}}$	effective magnetic field
$\mathbf{b}$	bandwidth per pixel
$\mathbf{b(x,y,z,t)}$	irreversible (time-varying) field inhomogeneities
$\boldsymbol{\beta}\mathbf{(x,y,z)}$	reversible(static) field inhomogeneities
$\mathbf{d}$	pixel displacement
$\mathbf{E_z}$	Zeeman energy
$\mathbf{f}$	frequency (Hz)
$\mathbf{G}$	gradient field
$\mathbf{M}$	net magnetization vector
$\mathbf{M_o}$	initial magnetization
$\mathbf{M_{xy}}$	transverse magnetization
$\mathbf{M_z}$	longitudinal magnetization
$\mathbf{n}\uparrow, \mathbf{n}\downarrow$	number of spins pointing parallel/anti-parallel to B_o
$\mathbf{N_{avg}}$	number of averages
$\mathbf{N_x, N_y}$	number of points
$\mathbf{N_{shots}}$	number of shots
$\mathbf{R_2}$	irreversible transverse relaxation rate
$\mathbf{R_2'}$	reversible transverse relaxation rate
$\mathbf{R_2^*}$	apparent transverse relaxation rate
$\mathbf{T}$	temperature
$\mathbf{T_1}$	longitudinal magnetization
$\mathbf{T_2}$	irreversible transverse decay time
$\mathbf{T_2'}$	reversible transverse decay time
$\mathbf{T_2^*}$	apparent transverse decay time
$\mathbf{T_{acq}}$	time of acquisition
$\mathbf{\Delta x, \Delta y, \Delta z}$	voxel dimensions
$\mathbf{\Delta B_o}$	static magnetic field inhomogeneities

Δf	bandwidth
ΔR_2^*	change in apparent transverse relaxation rate
$\Delta S/N$	BOLD contrast to noise ratio
$\Delta S/S$	BOLD signal change
Δ	change
$\partial t/t$	time derivative
$\int$	integration
Θ	flip angle
θ	phase
β	estimated parameters
ε	error
κ	Boltzmann constant
h	Planck's constant
$\hbar$	Planck's constant divided by 2π
I	angular momentum
τ	time delay, torque
γ	gyromagnetic ratio
μ	magnetic moment
ν	frequency
ω	angular frequency
ω_o	Larmor frequency
ω_{eff}	effective precession frequency
χ	magnetic susceptibility

Abbreviations

A/D	analog to digital converter
ASE	asymmetric spin echo
BOLD	blood oxygenation level dependent
BW	bandwidth
CBF	cerebral blood flow
CBV	cerebral blood volume
$CMRO_2$	cerebral metabolic rate of oxygen consumption
CNR	contrast to noise ratio
EMF	electromotive force
EPI	echo planar imaging
EV	extravascular
FFA	face fusiform area
FID	free induction decay
fMRI	functional magnetic resonance imaging
FOV	field of view
FT	Fourier transform
FWHM	full width at half maximum
GLM	general linear model
GRAPPA	generalized auto-calibrating partially parallel acquisitions
GRE	gradient-recalled echo
Hb	deoxyhemoglobin
HbO_2	oxyhemoglobin
HRF	hemodynamic response function
IV	intravascular
MNI	Montreal Neurological Institute
MRI	magnetic resonance imaging
NMR	nuclear magnetic resonance
PET	positron emission tomography
PRESS	point resolved spectroscopy

PSF	point spread function
RF	radio frequency field
ROI	region of interest
SAR	specific absorption rate
SD	standard deviation
SE	spin echo
SENSE	sensitivity encoding
SNR	signal to noise ratio
SPM	statistical parametric map
TE	time of echo
TR	time of repetition
T/R	transmit/receive

1 Introduction

As early as 1970's, radioactive tracing methods such as PET (positron emission tomography) were used to study brain activation. The methods were based on quantifying blood flow in brain. In the late 1980's, Thulborn [1] and Ogawa [3] made groundbreaking discoveries that changes in blood oxygenation cause changes in the gradient-echo (GRE) MRI signal. Several groups followed by quantifying this change in the motor and visual cortices.

Magnetic resonance imaging (MRI) quickly became popular for studying brain activation due to several key advantages it offers. Unlike PET, MRI is not based on ionizing radiation and thus provides no major health risks to humans. It is also a noninvasive technique which allows for group and longitudinal studies.

Functional MRI (fMRI) in general refers to any technique which measures some aspect of the local physiological changes following neural activity. However, the most popular method to date has been based on the close but incongruous coupling of blood flow and oxygen metabolism following neural activity. In the early 1990's, Ogawa coined this method the blood oxygenation level dependent (BOLD) effect.

Conventional imaging methods were first employed for collecting functional MRI data. However, these methods were slow, time-consuming and could not capture the BOLD signal continuously. Steadily, developments in gradient and shim systems made echo planar imaging (EPI), conceived by Sir Mansfield [2], the preferred imaging protocol. EPI offers reasonable image quality in addition to high temporal resolution which is absolutely necessary for fMRI studies.

In recent years, the general interest has shifted to high magnetic fields (>4T). It has been observed that high field fMRI benefits from a higher signal-to-ratio, higher BOLD effect and accuracy. Due to larger magnetic susceptibility gradients, however, EPI image quality severely degrades at high fields, which in many cases limits brain coverage and subsequently the scope of the fMRI study. Nonetheless, high field functional MRI stands to benefit as more advanced hardware and post-processing solutions are developed in the coming years.

1.1 Scope of thesis

This thesis begins by introducing the basic principles of a magnetic resonance experiment. Chapter 2 also discusses how an image is formed and the sources of image contrast in MRI.

Chapter 3 is a general introduction to functional magnetic resonance imaging with discussions on the biophysical basis of the BOLD effect, the extravascular and intravascular components of the BOLD signal in addition to key literature reviews on the effect of field strength on the BOLD effect.

Since one focus of this thesis is the optimization of EPI protocol for fMRI studies at 4.7T, chapter 4 is dedicated entirely to echo planar imaging sequence. There is an in depth discussion of EPI artifacts, acquisition parameter optimization at 4.7T and reconstruction techniques using a signal reference scan. Appendix A provides Matlab code for reconstructing EPI images.

Chapter 5 briefly focuses on the statistical analysis of the fMRI data in addition to stimulation paradigm design. The discussion is mainly focused on SPM5 software due to its widespread use in fMRI literature. Several key toolboxes are also touched on for further data quantification.

In chapter 6, several fMRI studies were designed to explore the visual and language functions of the brain at 4.7T. The experiments were replicated on the 1.5T scanner. The BOLD signal change and BOLD contrast to noise ratio (CNR) were quantified and compared across the two fields to show the advantages and disadvantages of high field fMRI. Chapter 7 touches on the major conclusions derived in this thesis in addition to outlining possible future research and theoretical work in this area.

References

1. K. R. Thulborn, J. C. Waterton, P. M. Matthews, G. K. Radda, Oxygenation dependence of transverse relaxation time of water protons in whole blood at high field. *Biochem. Biophys. Acta.* **714**, 265-270 (1982).

2. P. Mansfield, Multi-planar image formations using NMR spin echoes. *J. Phys. C.* **10**, L55-58 (1977).

3. S. Ogawa, T. M. Lee, A. S. Nayak, P. Glynn, Oxygenation-sensitive contrast in magnetic resonance image of rodent brain at high magnetic fields. *Magn. Reson. Med.* **14**, 68-78 (1990).

2 Physics of Magnetic Resonance Imaging

This chapter introduces the principles of magnetic resonance imaging to the reader by first outlining the three main stages of a nuclear magnetic resonance experiment. This is followed by the concept of nuclear relaxation and its role in image contrast. The reader is then introduced to the method of imaging in MRI, namely spatial encoding. The chapter concludes by introducing the concept of k-space which is essential for understanding different imaging techniques in MRI.

2.1 Nuclear Magnetic Resonance (NMR)

Nuclear magnetic resonance "is a phenomenon which occurs when the nuclei of certain atoms are immersed in a static magnetic field and exposed to a second oscillating magnetic field" [4].

As such, a nucleus has to possess a net spin – i.e. a net magnetic moment (μ) – in order to interact with a magnetic field:

$$\bar{\mu} = \gamma \bar{I} \hbar , \tag{1}$$

where γ is the gyromagnetic ratio, $\bar{I}$ is the spin angular momentum and $\hbar$ is Planck's constant divided by 2π ($\hbar = 1.054 \times 10^{-34}\ J.s$).

Just like electrons, protons and neutrons – known together as nucleons - have spins and fill energy orbital. If there is an even number of nucleons, the energy orbital fills, spins pair together and cancel out, resulting in zero net magnetic moment. As an example, consider ^{12}Carbon which has 6 protons and 6 neutrons. Since the nucleon is even, it has no net spin ($\mu = 0$). Thus, it is NMR insensitive. ^{13}Carbon on the other hand has an odd nucleon and is used extensively in magnetic resonance spectroscopy. The following table lists some useful nuclei in NMR.

Table 2.1.1: List of useful NMR nuclei [11].

Nucleus	Unpaired protons	Unpaired Neutrons	γ (MHz/T)
^{1}H	1	0	42.58
^{31}P	1	0	17.25
^{23}Na	1	2	11.27
^{14}N	1	1	3.08
^{13}C	0	1	10.71

2.2 *Stages of NMR*

Magnetic resonance imaging experiment consists of three main preparation stages prior to actual imaging which are discussed in the following sections.

2.2.1 Preparation

The living body is made up mainly of hydrogen atoms. In the absence of a magnetic field, the spins of these hydrogen nuclei are oriented in random directions. This results in no net magnetization at thermal equilibrium.

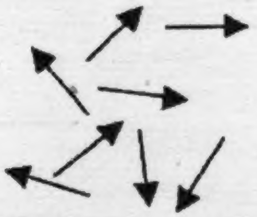

Figure 2.2.1: Spins in thermal equilibrium with no net magnetization.

To conduct an NMR experiment, a uniform, static magnetic field B_o is applied. The magnetic spins align themselves to the magnetic field in either a parallel or anti-parallel orientation, as a consequence of their quantum behavior, namely the atomic nuclear spin angular momentum (I). For hydrogen atoms, I = ½ which means there are two energy states and therefore two orientations.

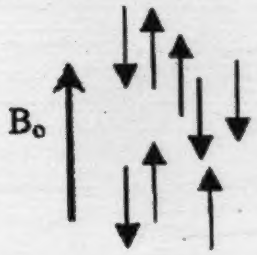

Figure 2.2.2: Preparation phase.

Since the parallel orientation has the lower energy of the two states, it is more stable and therefore more spins remain in this state. The ratio of the population of the protons within the two energy states is given by the classical Maxwell-Boltzmann statistics equation:

$$n\downarrow / n\uparrow = e^{-E_z / \kappa T}, \qquad (2)$$

where ↑ points along the B_o field, κ is Boltzmann constant ($1.38x10^{-23}\ J/k$), T is the temperature (Kelvin) and E_z is referred to as Zeeman energy.

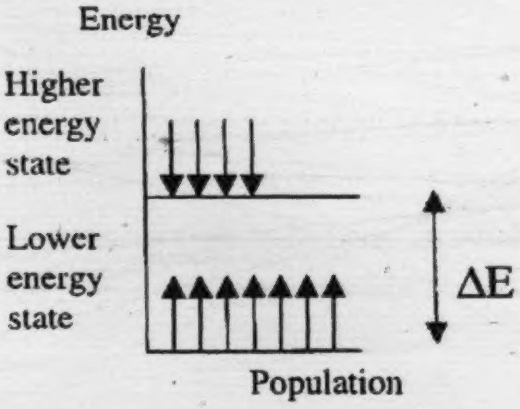

Figure 2.2.3: Population distribution of nuclear spins after application of B_o.

The energy difference E_z between the two energy states is proportional to the strength of B_o and to the size of the magnetic moment of the nucleus $h\gamma$:

$$E_z = h\gamma B_o. \qquad (3)$$

When the magnetic moment of the parallel spins is subtracted from the magnetic moment of the anti-parallel spins, the resultant net magnetization can be expressed as a vector pointing along the B_o field:

$$M = \sum \mu \uparrow - \sum \mu \downarrow. \qquad (4)$$

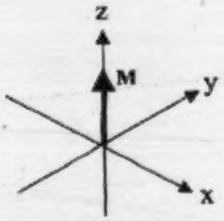

Figure 2.2.4: The net magnetization vector (M_z) in the presence of B_o.

The above discussion assumes that the spins line up exactly parallel or anti-parallel to the magnetic field. In reality, however, the spins precess about B_o at an angle.

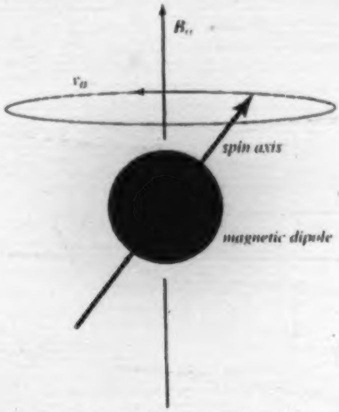

Figure 2.2.5: Nuclear spins precession about B_0 at an angle.

This precession is due to the torque applied by B_o to the spins:

$$\tau = \mathrm{B}_{\mathrm{o}} \times \vec{\mu}. \tag{5}$$

The angular frequency ω_o of nuclear precession around B_o is found by noting that frequency ν is related to energy E as,

$$\begin{aligned} \nu &= E / h. \\ E &= \gamma\hbar B_o \\ \nu &= \gamma\hbar B_o / h = \gamma B_o / 2\pi \\ \omega_o &= \gamma B_o \end{aligned} \tag{6}$$

ω_o is referred to as the Larmor frequency and is unique for each nucleus. Hydrogen for instance has a Larmor frequency of 42.58MHz/T (refer to Table 2.1.1).

In summary, the preparation stage allows magnetic spins to act in unison by the application of a uniform, static magnetic field of considerable strength (in Tesla units).

2.2.2 Excitation

The net longitudinal magnetization is not measurable in the presence of the overwhelmingly strong B_o field. During the application of a uniform static magnetic field, a second magnetic field B_1 is applied to the system. The B_1 field, referred to as the radio frequency field (r.f. field), is a time-varying magnetic field which rotates at the same angular frequency ω_o as the nuclei under study (on-resonance) and in a negative sense.

The B_1 field is perpendicular to the B_o field and as such applies a torque to the net magnetization M_z causing its angle to deviate from the B_o field direction. Even though the B_1 field is much weaker than the B_o field, its time-varying nature makes it possible to tip the magnetization down to the transverse plane.

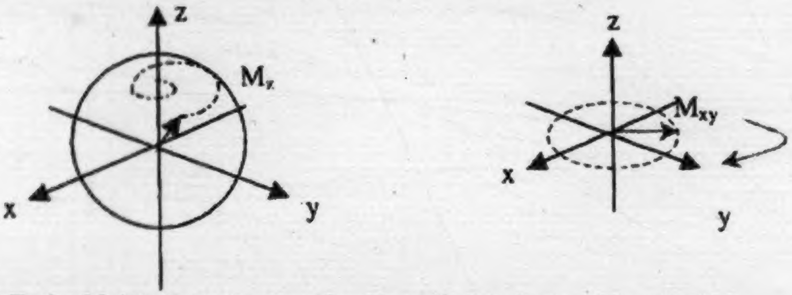

Figure 2.2.6: B_1 tips M_z into the transverse plane in a spiral trajectory. The resulting magnetization M_{xy} rotates in the transverse plane at the same frequency and direction as the applied B_1 field.

The angular displacement of M_z from the B_o field is described by the flip angle Θ :

$$\Theta = \int B_1 dt . \qquad \textbf{(7)}$$

The flip angle is specified by varying the amplitude and duration of the r.f. field. A 90° flip angle flips M_z into the transverse plane, resulting in maximum signal. After excitation, the B_1 field is switched off. The transverse magnetization M_{xy}, now perpendicular to the B_o field, experiences a torque from B_o:

$$\begin{aligned} \tau &= \partial(\bar{I}\hbar)/\partial t \\ &= \partial(\bar{M}_{xy})/\partial t \qquad \textbf{(8)} \\ &= \bar{M}_{xy} \times B_o \ . \end{aligned}$$

This torque causes M_{xy} to precess in the transverse plane at the same frequency as B_1. For more detailed mathematical description of excitation, refer to [10].

2.2.3 Acquisition

When the r.f. field is switched off, the magnetization vector M_{xy} precesses in the transverse plane. This precession results in an oscillating magnetic field which induces a sinusoidal electromotive force (*EMF*) in a wire loop known as an r.f. coil. R.F. coils act as antennas, tuned to the Larmor frequency of the nucleus under study.

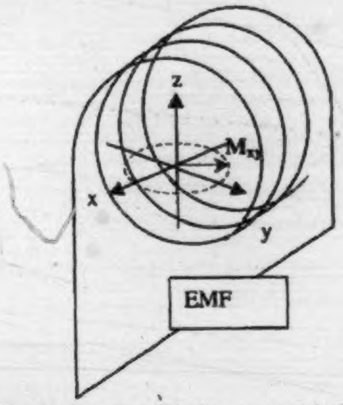

Figure 2.2.7: M_{xy} precession results in an oscillating magnetic field which induces a sinusoidal EMF in a wire loop known as an r.f. coil.

Under ideal conditions, the EMF oscillates forever. However, as shown in Figure 2.2.8, the EMF decays exponentially over time. This is due to interaction of the spins with their surroundings which is discussed in section 2.3. The decaying EMF signal is referred to as the fast-induction decay (FID). The FID is Fourier-transformed to give its power spectrum at the Larmor frequency ω_o which is unique for each nucleus.

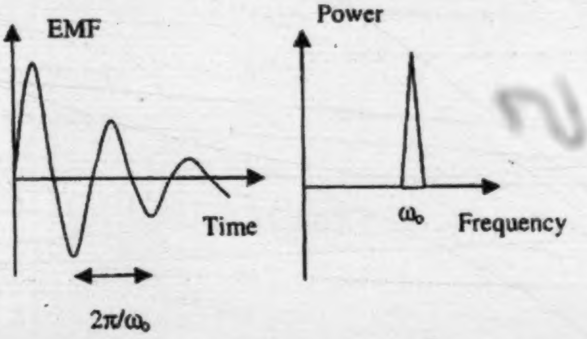

Figure 2.2.8: A sinusoidal signal with frequency ω_o in the time domain is represented as an impulse function centered on ω_o. A decaying sinusoidal signal (EMF) is represented as a broadened impulse function.

2.3 *Relaxation*

In the presence of the B_o field, the net magnetization M_z rotates around the z axis. There is no transverse magnetization M_{xy} in this stage. When a B_1 field is applied, the longitudinal magnetization M_z is pulled to the transverse plane. Therefore, M_z goes to zero and the net magnetization is now M_{xy}.

Once the r.f. field is switched off, the magnetic spins tend to go back to equilibrium state over time. This happens in such a way that the longitudinal magnetization M_z and the transverse magnetization M_{xy} go through two very distinct but related processes.

2.3.1 Longitudinal Relaxation (T_1)

Also referred to as the spin-lattice relaxation, T_1-relaxation is the consequence of the interaction of the spins with their surrounding environment. T_1-relaxation following a 90° r.f. pulse is characterized by the following equation:

$$\begin{aligned} M_z(t) &= M_o(1-e^{-t/T_1}) \\ &= M_o(1-e^{-tR_1}), \end{aligned} \quad (9)$$

where $T_1 = 1/R_1$ is the longitudinal relaxation rate.

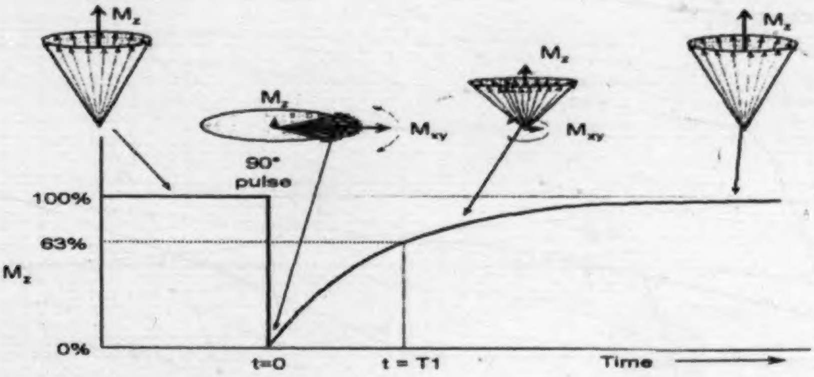

Figure 2.3.1: **T_1-relaxation process.**

Note from Figure 2.3.1 that time T_1 is defined as the time when the longitudinal relaxation recovers to 63% of its equilibrium value. T_1 is used in MRI to describe the time of M_z recovery.

T_1-relaxation is one of the main sources of contrast in MRI. After the same time delay, different tissues with equal amount of nuclei will have different signal strengths.

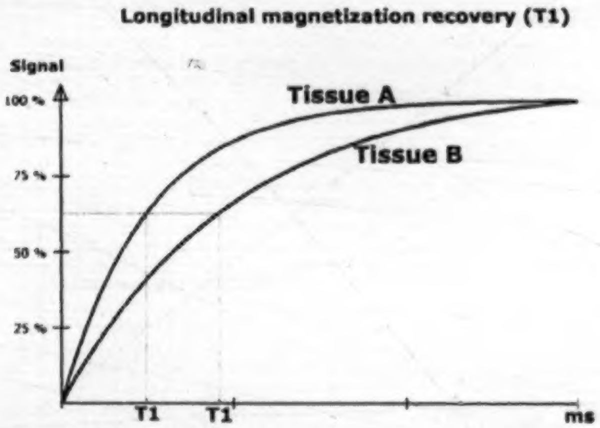

Figure 2.3.2: T_1 values for different tissue types provide a source of image contrast.

The following table lists T_1 values for different tissue types at 1.5T:

Table 2.3.1: T_1 values for different tissue types at 1.5T [5].

Tissue	T_1 (ms)
Skeletal Muscle	870
Liver	490
Spleen	780
Fat	260
Grey Matter	920
White Matter	790
CSF	>4000

2.3.2 Transverse Relaxation

Also referred to as the spin-spin relaxation, transverse relaxation arises from the interaction of the spins with each other. The spin interaction causes local magnetic field perturbations which can be classified as either static (reversible) or time-varying (irreversible).

Intrinsic T_2 relaxation

After the B_1 field is switched off, the transverse magnetization M_{xy} precesses in the transverse plane at the Larmor frequency. In an ideal homogenous magnetic field, M_{xy} would precess about B_o indefinitely; however, realistically, the magnetic spins experience local field perturbations from other spins such that the effective field experienced by each spin is now,

$$B_{eff} = B_o + \gamma b(x,y,z,t), \tag{10}$$

where *b(x,y,z,t)* term contains temporal and spatial field inhomogeneities.

In this new magnetic field, the spins no longer precess at the Larmor frequency:

$$\omega_{eff} = \omega_o + \gamma b(x,y,z,t). \tag{11}$$

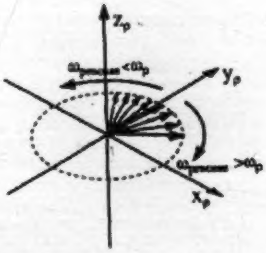

Figure 2.3.3: Spins precession with different frequencies.

Each magnetic spin precesses with a different frequency and as a result accrues phase ($\theta = \omega t$) over time. The phase incoherence between spins causes the net magnetization M_{xy} to decrease to its equilibrium value of zero through T_2-relaxation characterized by the following equation:

$$M_{xy} = M_{xy}(0)e^{-t/T_2}, \tag{12}$$

where $M_{xy}(0)$ is the transverse magnetization immediately following an r.f. pulse.

The T_2-relaxation mechanism is summarized in Figure 2.3.4:

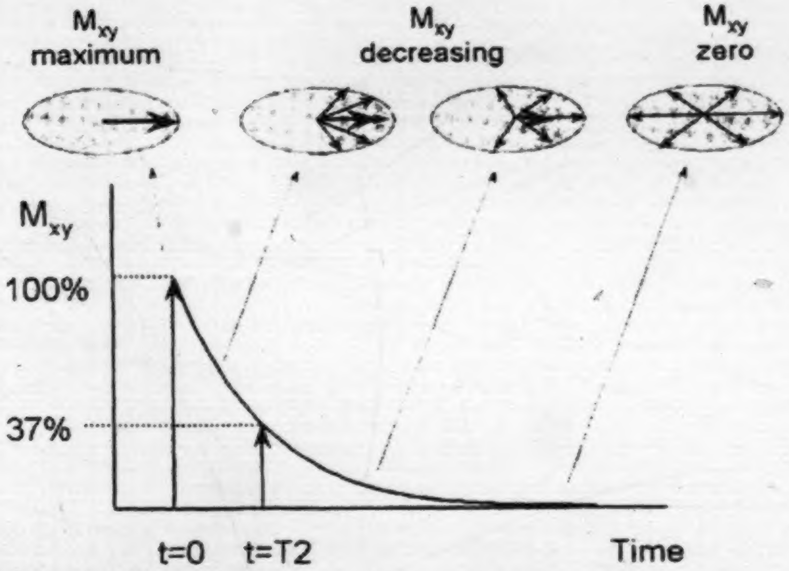
M_{xy} maximum
M_{xy} decreasing
M_{xy} zero
M_{xy}
100%
37%
t=0
t=T2
Time

Figure 2.3.4: T_2-relaxation process.

Note that at time T_2, the transverse magnetization decays to 37% of its initial magnetization. Just like T_1-relaxation, T_2 decay is another source of image contrast. Table 2.3.2 lists T_2 values for different tissue types at 1.5T:

Table 2.3.2: T_2 values for different tissue types at 1.5T [5].

Tissue	T_2 (ms)
Skeletal Muscle	47
Liver	43
Spleen	62
Fat	84
Grey Matter	101
White Matter	92
CSF	>2000

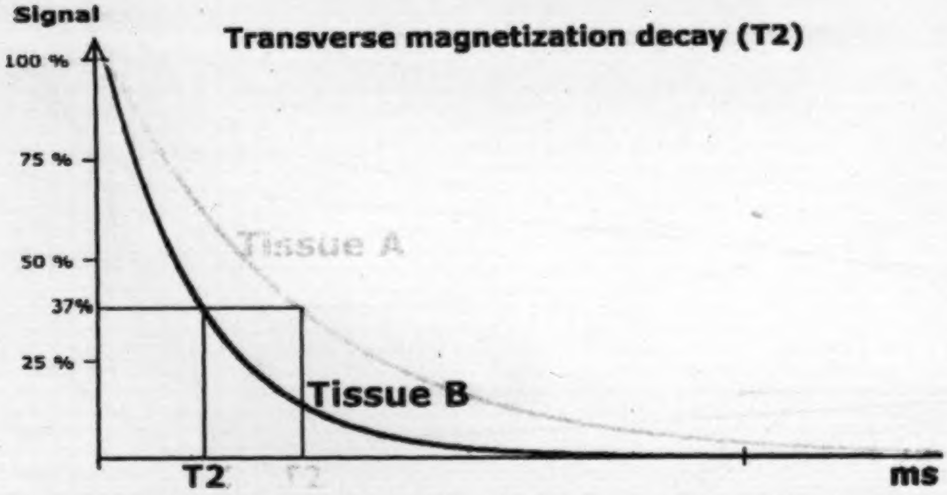

Figure 2.3.5: T_2 values for different tissue types provide a source of image contrast.

T_2*-relaxation

In practice, there are additional sources of field inhomogeneity: imperfections in the magnet design and differences in magnetic susceptibility at different tissue interfaces (e.g. nasal cavity). The magnetic field experienced by the spins is now,

$$B_{eff} = B_o + b(x,y,z,t) + \beta(x,y,z), \qquad (13)$$

where *$\beta(x,y,z)$* term represents the static field inhomogeneities. Because of the additional field inhomogeneities, the FID signal decays faster with an R_2* rate:

$$R_2^* = R_2 + R_2', \qquad (14)$$

where R_2 term ($1/T_2$) is the intrinsic irreversible relaxation rate, and R_2' is the reversible relaxation rate ($1/T_2'$). Eqn. 14 may be rewritten in terms of T_2* decay:

$$1/T_2^* = \gamma\Delta B_o + 1/T_2, \qquad (15)$$

where ΔBo takes account of the static magnetic field inhomogeneities.

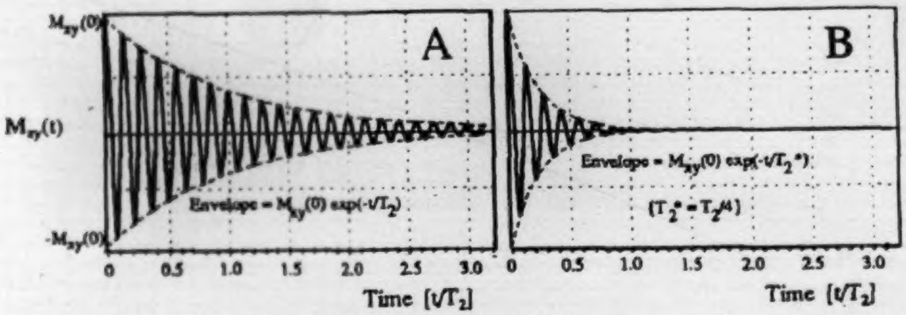

Figure 2.3.6: Comparison between T_2 and T_2* decay rates.

Since the T_2'- relaxation component is static, it is reversible by the application of a 180° r.f. pulse along either of the transverse planes. The time at which the spins refocus is called the time of echo (*TE*).

2.3.3 Contrast Mechanism

After the magnetization is flipped to the transverse axis, it begins both longitudinal recovery and transverse decay. The experiment might be T_1-weighted, T_2-weighted or T_2*-weighted. Each of these experiments makes use of the differences in T_1 and T_2 values between different tissue types to bring out image contrast.

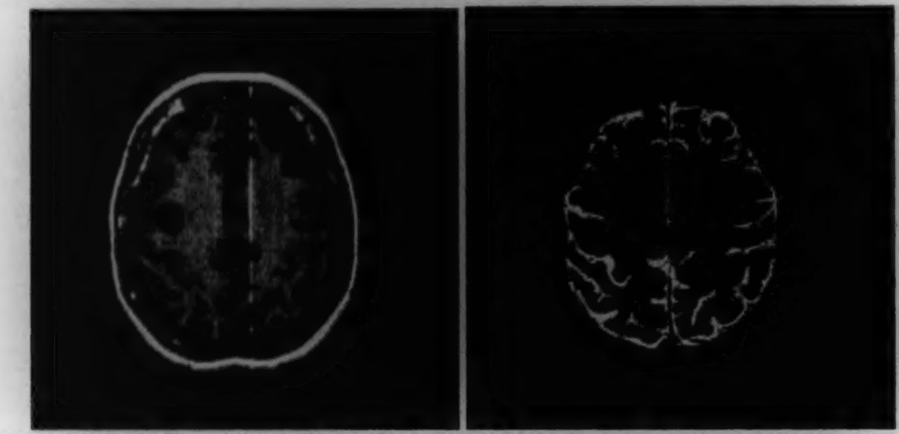

Figure 2.3.7: Left: T_1-weighted, Right: T_2-weighted. Note the contrast changes in gray and white matter in the two clinical images. Note that CSF is dark in T_1-weighted images whereas it is bright in T_2-weighted images.

To the reader, it might seem that the T_2*-weighted contrast is not of much use since the FID decays so rapidly. However, T_2* is the main source of contrast in functional MRI where neural activity is detected endogenously by measuring the differences in blood oxygenation states. A T_2-weighted experiment in this case would have a lower sensitivity. For general information on functional MRI, refer to chapter 3.

2.4 Echo formation

As mentioned before, spins lose their phase coherence due to static and time-varying sources of field inhomogeneity. Static dephasing component (T_2') can be reversed by two methods. In any case, an echo is formed when the phases of the spins combine constructively along either the x/y plane.

2.4.1 Spin Echo (SE)

Following excitation, the spins lose phase coherence. They fan out after a period τ, with some spin precessing faster and some slower than the Larmor frequency (Figure 2.3.3). By applying a refocusing pulse along the x or y axis, the spins converge to either the –y or y plane at time 2τ (TE):

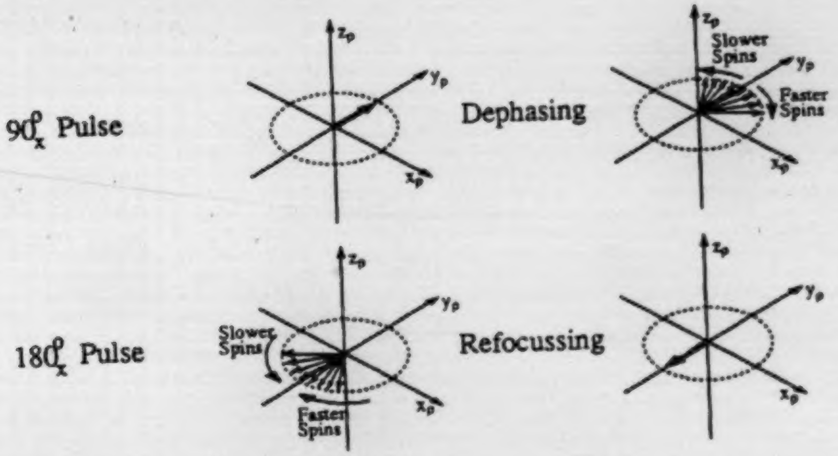

Figure 2.4.1: Application of a 180° r.f. pulse refocuses static dephasing.

The phase of the spins sums coherently and constructively causing the formation of the spin echo. The whole process is summarized in the following figure:

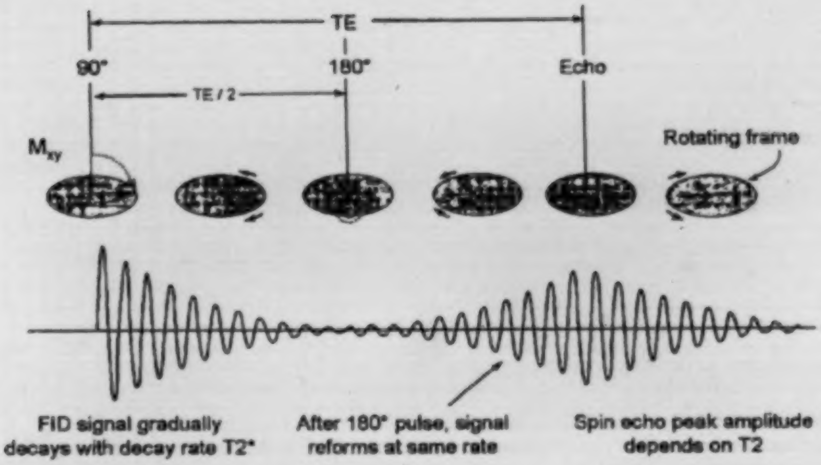
TE
90°
180°
Echo
TE / 2
M$_{xy}$
Rotating frame
FID signal gradually decays with decay rate T2*
After 180° pulse, signal reforms at same rate
Spin echo peak amplitude depends on T2

Figure 2.4.2: Spin-echo Formation.

Due to irreversible T_2 decay, the precession frequency of some of the spins changes during the dephasing and refocusing times. These spins do not refocus at time TE and their intensity will be lost. The subsequent application of 180° r.f. pulses therefore results in decreased echo intensities over time.

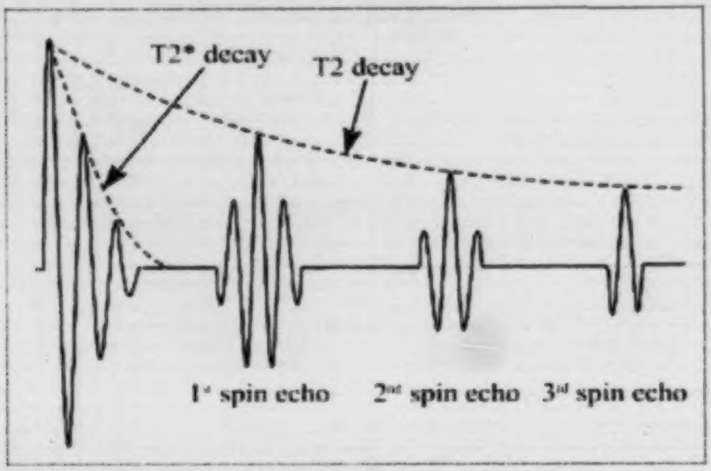
T2* decay
T2 decay
1st spin echo
2nd spin echo
3rd spin echo

Figure 2.4.3: Application of 180° r.f. pulses refocuses the static field inhomogeneities.

2.4.2 Gradient-recalled Echo (GRE)

The gradient recalled method makes use of imaging gradients to refocus the spins. As will be shown in section 2.5, gradient fields cause the precession frequencies of the spins to change based on their spatial position:

$$\omega = \gamma(B_o + G_r\vec{r}), \qquad (16)$$

where *r* represents spatial position *(x,y,z)* of the spins and *G* is the gradient amplitude. The range of precession frequencies produced by a gradient field leads to dephasing between spins as each spin accumulates a unique phase θ based on its spatial position:

$$\theta = \omega t\,. \tag{17}$$

The direction of the precession frequencies can be reversed by applying a reverse polarity gradient:

$$\begin{aligned} \omega &= \gamma(B_o - G_r r) \\ \theta &= -\omega t. \end{aligned} \tag{18}$$

The phase of the spins sum coherently and the spins refocus at time TE,

$$\begin{aligned} \omega &= \gamma B_o \\ \theta &= 0. \end{aligned} \tag{19}$$

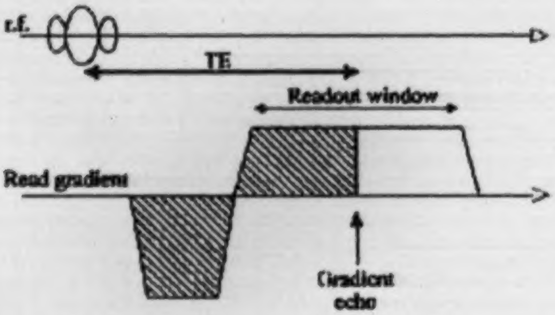

Figure 2.4.4: Gradient-recalled echo formation.

The above two methods are the foundations of spin-echo and gradient-echo imaging sequences. The spin-echo sequence uses 180° r.f. pulses to refocus spin dephasing. The gradient echo sequences use gradients but only for imaging purposes.

2.5 Imaging

Once the B_1 field has tipped the magnetization into the transverse plane, the spins precess at the Larmor frequency ω_0. However, the NMR experiment can not yet produce an image. As was seen in Figure 2.2.8, without some sort of encoding, the power of the signal is solely concentrated at the Larmor frequency which does not indicate much about the object being imaged. In order to create an image, M_{xy} must carry information about frequencies present in the image.

2.5.1 Spatial Encoding

"Spatial encoding is considered as the determination of the [transverse magnetization] M_{xy} as a function of the spatial variables (x,y,z)"[16]. The NMR experiment encodes spatial information into the precession frequency through the application of additional magnetic fields. These magnetic fields or "gradients" are applied in the direction of the main magnetic field B_o but linearly varying in any arbitrary direction. For instance, a gradient applied along the *x* direction is $G_x = dB_o/dx$. Refer to Figure 2.5.1.

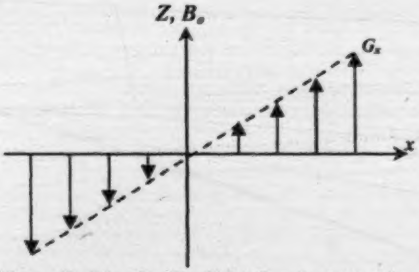

Figure 2.5.1: A gradient field applied in the B₀ direction but varying in the *x* direction.

In the above figure, the gradient field causes the spins to experience different magnetic fields depending on their spatial position along *x*: $B_{eff} = B_o + G_x x$. The new precession frequency for each spin, based on its spatial position is $\omega_{eff} = \omega_o + \gamma G_x x$. In summary, spatial information is encoded into the MR signal by changing the instantaneous precession frequency of the spins based on their position.

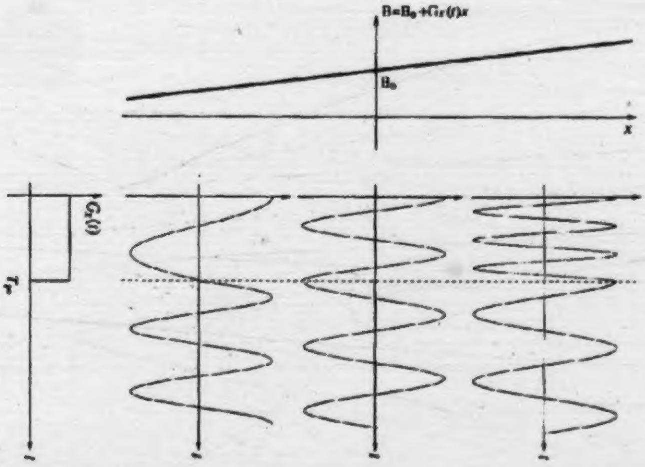

Figure 2.5.2: A gradient field changes the instantaneous frequency of the signal.

Generally, the MR signal is encoded in three dimensions. One dimension of localization is performed using slice-selective excitation. The other two dimensions of localization are typically performed with frequency and phase gradients.

2.5.2 Slice-select Encoding

The goal of slice-select encoding is to restrict the area of imaging and create transverse magnetization only in that region. In this way, the receiver coil is only sensitive to the desired slice. The application of the r.f. field causes all points within the object to precess with the Larmor frequency. This pulse is "nonselective". In order to image a specific region, a gradient field is applied to create a spectrum of resonant frequencies Δf within the object. An r.f. pulse is applied simultaneously with the gradient whose bandwidth matches the frequency spread Δf. The combination of the "selective" r.f. pulse and the gradient is called slice selection.

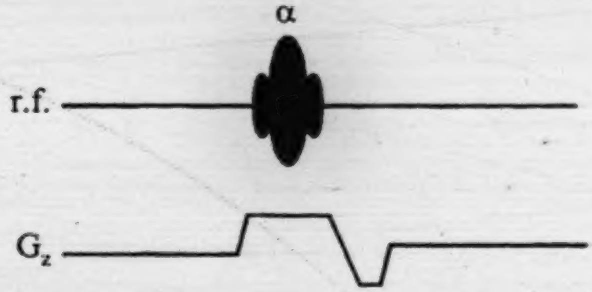

Figure 2.5.3: Slice Selection.

As an example, consider imaging on Varian 4.7T system with $G_{max} = 3.5G/cm$ and an r.f. pulse of *4.0ms* duration. Let's consider an axial slice. Note that in order to excite a slice in the *z*-plane, a z gradient must be applied. The minimum slice thickness achievable is calculated by noting that,

$$\begin{aligned}\Delta f &= f(z_{max} - z_{min}) \\ &= (\gamma/2\pi)\{(B_o - G_z z_{max}) - (B_o + G_z z_{max}) \\ &= (\gamma/2\pi)G_z\Delta z,\end{aligned} \qquad \textbf{(20)}$$

where Δf is the bandwidth of the r.f. pulse and Δz is the slice thickness. Considering a Sinc r.f. pulse with 5 lobes, the r.f. bandwidth is calculated as, $\Delta f = 5x10^6$ / pulse width (us) = $5x10^6/4000$ = 1250 Hz. The minimum achievable slice thickness is then calculated by rearranging Eqn.20: Δz = (2*1250Hz)/(3.5G/cm*4258Hz/G)= 0.17 cm.

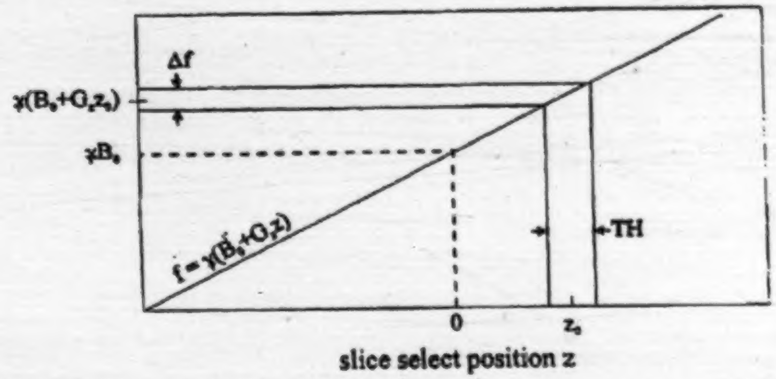

Figure 2.5.4: The frequency bandwidth of the r.f. pulse is linearly proportional to the slice thickness.

The absolute frequency of the r.f. pulse can be changed to excite a slice centered at a position other than the iso-center, i.e. *(x,y,z) = (0,0,0)*. In that case, the offset frequency is,

$$f_{off} = (\gamma/2\pi)G_z\Delta z_{off}, \qquad (21)$$

and the slice midpoint corresponds to an r.f. frequency of

$$f_{abs} = f_o + f_{off}. \qquad (22)$$

Continuing with the previous example, let's excite a slice *1.5cm* away from the magnet's iso-center. The frequency of the excitation pulse is,

f = (42.58 MHz/T){4.7T + 3.5G/cm*1T/10000G*1.5cm} = 200.148MHz.

It is clear now that the r.f. pulse absolute carrier frequency corresponds to slice position, and the r.f. pulse bandwidth (or duration) determines the slice thickness. In addition, modulating the r.f. pulse time-varying envelope results in the desired frequency profile.

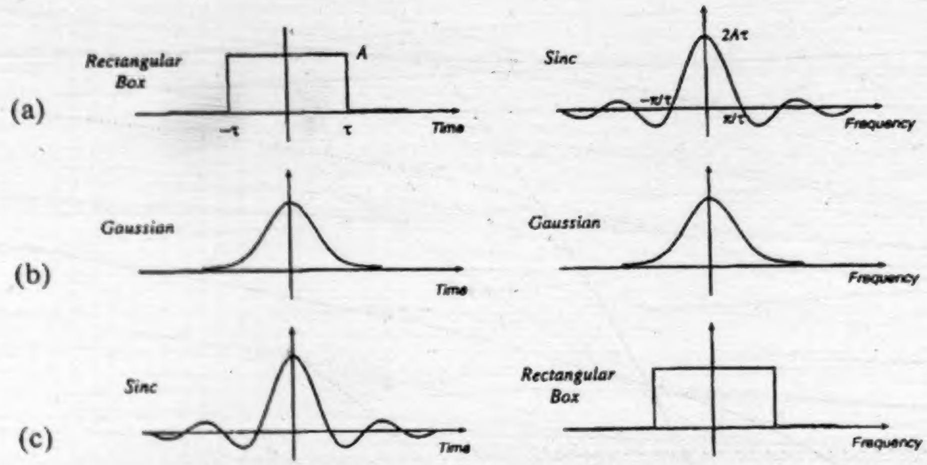

Figure 2.5.5: Modulating the r.f. pulse time-varying envelope results in the desired frequency profile. The rectangular pulse in a) results in nonselective frequency profile. The Gaussian and Sinc pulses in b) and c) result in selective frequency profiles.

2.5.3 2D Fourier Imaging

After selecting a slice, the next step is to spatially-encode the transverse magnetization in two other orthogonal directions, namely the frequency (or readout) and phase-encode directions.

Frequency Encoding

Frequency encoding is similar to slice-selective encoding in that a gradient is applied along the direction of interest. However; no r.f. pulse is required as the signal is assumed to be contained within a frequency range defined by the field of view (*FOV*):

$$\begin{aligned}\Delta f &= f(r_{\max} - r_{\min}) \\ &= (\gamma/2\pi)\{(B_o + G_r r_{\max}) - (B_o + G_r r_{\min})\} \\ &= (\gamma/2\pi) G_r FOV_r\,, \end{aligned} \qquad \textbf{(23)}$$

where *r* could be in any arbitrary direction *(x,y,z)*.

In MRI, the sampling bandwidth Δf is usually set to a fixed value, say 300 KHz. The operator specifies the FOV (in cm) and the appropriate gradient strengths are calculated. FOV is specified such that it covers the region of interest. The human brain can be contained in a FOV of 18-24 cm. For a bandwidth of 300 KHz and FOV of 24cm, the gradient strength is calculated as G = 300 KHz / (4528Hz/G * 24cm) = 2.9G/cm.

Let's assume that the frequency-encode gradient is applied in the *x* direction. The time-domain signal detected with an r.f. coil is,

$$S(t) = \int M_{xy}(x) e^{-i\gamma t G_x x} dx . \qquad \textbf{(24)}$$

In reality, the magnetization has dependence along the *y* direction as well. But in the absence of any *y* gradient, the detected signal is,

$$S(t) = \int\int M_{xy}(x) e^{-i\gamma t G_x x} dxdy . \qquad \textbf{(25)}$$

Phase Encoding

One might assume that applying two gradients at the same time would result in 2D spatial encoding. However, since the gradients sum up, this would actually result in 1D spatial encoding. This is the basis of the projection reconstruction method. In order to achieve rectilinear sampling (simpler reconstruction), a gradient must be applied in an orthogonal direction to the frequency-encode gradient.

Let's apply a gradient in the *y* direction for a finite time *τ*. The application of the gradient causes the spins to process with different frequencies. The gradient is then shut off. In the presence of only the B_0 field, the spins revert to precess with the Larmor frequency but now they possess a unique phase. This phase was acquired during the application of the *y* gradient for the duration *τ*:

$$\theta = \omega(t)\tau = \gamma G_r r \tau . \qquad \textbf{(26)}$$

Eqn. 26 shows that the phase of the spins provides an additional mean of spatially-encoding the MR signal. The time-domain signal detected now has both an x and y dependence:

$$S(t) = \int\int M_{xy}(x.y) e^{-i\gamma t (G_x x + G_y y)} dxdy . \qquad \textbf{(27)}$$

Eqn. 27 implies that the combination of non-zero phase-encode gradients and a frequency-encode gradient results in a rectilinear sampling grid. The transverse magnetization M_{xy} can be recovered by 2D Fourier transform.

2.6 2D Fourier Transform Reconstruction

After spatial-encoding the time-domain signal, Fourier transform can be applied separately in the frequency and phase-encode directions to find the signal strength as a function of frequency. Remember that Fourier transform is defined as,

$$F(\omega) = \int f(t)e^{-i\omega t}dt\,. \qquad \textbf{(28)}$$

Eqn. 28 can be extended to an NMR experiment by substituting ω by $\gamma . G_x . x$ and integrating over two orthogonal directions:

$$\begin{aligned} S(t) &= \int\int M_{xy}(x.y)e^{-i\gamma t(G_x x+G_y y)}dxdy \\ &= FT(M_{xy}(x.y)). \end{aligned} \qquad \textbf{(29)}$$

S(t) is the encoded signal in the time domain. The goal is to recover M_{xy}, the transverse magnetization spatial density. Using inverse Fourier transform,

$$\begin{aligned} M_{xy}(x,y) &= \gamma^2 G_x G_y \int\int S(t)e^{i\gamma t(G_x x+G_y y)}dt \\ &= IFT(S(t)). \end{aligned} \qquad \textbf{(30)}$$

Note that since Fourier transform operator is complex, it yields both an imaginary and real signal (phase and magnitude).

2.7 K-space

The raw data space in MRI is called 'k-space' and is defined as the gradient-time integral:

$$k_x = \gamma \int G_x dt\,, \qquad \textbf{(31)}$$

$$k_y = \gamma \int G_y dt\,. \qquad \textbf{(32)}$$

Using k-space definition, Eqn. 29 and 30 can be re-written as,

$$\begin{aligned} S(k_x,k_y) &= \int\int M_{xy}(x.y)e^{-i\gamma(k_x x+k_y y)}dxdy \\ &= FT(M_{xy}(x.y)). \end{aligned} \qquad \textbf{(33)}$$

$$\begin{aligned} M_{xy}(x,y) &= \int\int S(t)e^{i\gamma(k_x x+k_y y)}dk_x dk_y \\ &= IFT(S(t)). \end{aligned} \qquad \textbf{(34)}$$

As seen from Eqn. 33-34, If FID is sampled at sufficiently large number of points in k-space, the resulting data set can be inverse-Fourier transformed to provide an image of the object.

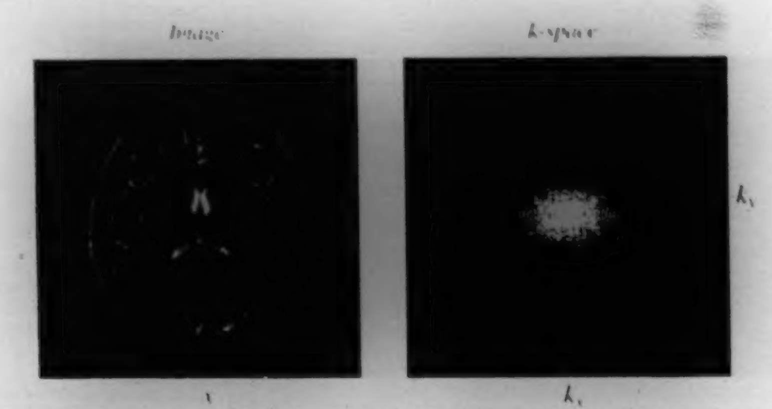

Figure 2.7.1: A transverse slice of the human brain and the corresponding raw k-space data. Note that most of the signal energy (image contrast) lies in the center of k-space. The outer k-space defines smaller details in the image.

2.7.1 Sampling Requirements

The continuous FID has to be correctly digitized in time. The Shannon sampling theorem states that a continuous-time signal can be recovered from its samples if the signal is contained within a specified frequency range (band-limited) and if the sampling frequency is greater than twice the signal bandwidth. In MRI, the range of frequencies within the imaging region is known beforehand by the field of view.

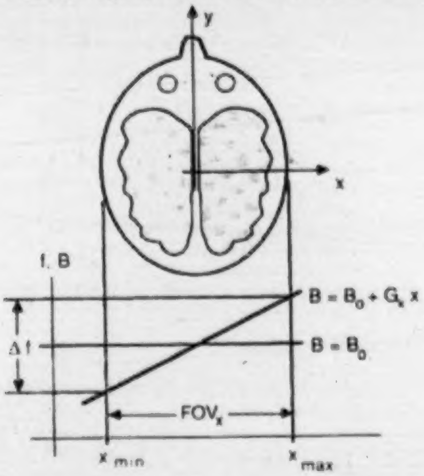

Figure 2.7.2: The range of frequencies in the frequency and phase-encode directions is defined by the field of view.

From Shannon's theorem, sufficient sampling frequency for correct image reconstruction is,

$$f_{\max} = \gamma G\,FOV/2 \tag{35}$$

$$BW_{samp} = \Delta f = \gamma GFOV\,. \tag{36}$$

The correct combination of BW and G ensures that the signal is sampled sufficiently for correct Fourier image reconstruction. In MRI, FOV is specified to cover the region of interest and the sampling bandwidth is set to a fixed value (for discussion of how the sampling bandwidth is specified, refer to section 4.4.1). The frequency and phase gradients are then adjusted by the imaging system for correct digitization of the FID signal. Therefore,

$$G_x = BW/\gamma FOV_x\,, \quad \text{in the readout direction,} \tag{37}$$

$$\Delta G_y = 1/\gamma FOV_y\tau\,, \quad \text{in the phase-encode direction.} \tag{38}$$

For a 2D image, the number of time points sampled is,

$$\Delta k_x = \gamma G_x \Delta t = 1/FOV_x \tag{39}$$
$$\Delta k_y = \gamma \Delta G_y \tau = 1/FOV_y\,. \tag{40}$$

Eqn. 39-40 show clearly the relationship between spatial frequency k and temporal frequency FOV. Also note that larger FOV produces higher frequencies in the signal, requiring faster digitization of FID ($f_s>f_{max}$). The final image resolution may be defined as well:

$$\Delta x = FOV_x/N_x = 1/k_x\,. \tag{41}$$
$$\Delta y = FOV_y/N_y = 1/k_y\,. \tag{42}$$

As seen from Eqn. 41-42, the extent of k-space (and not the k-space sampling interval) determines the pixel resolution in the final image. Since imaging in MRI is done with gradients and k-space is defined as the gradient-time integral, k-space provides an alternative method of looking at MRI sequences. All magnetic resonance imaging methods sample k-space by devising strategies for varying the gradients amplitude and duration. Conventional MRI methods obtain only a small portion of k-space after an r.f. excitation. This can be seen in the following figure.

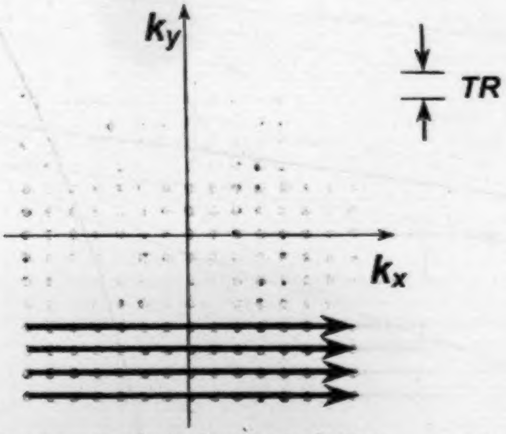

Figure 2.7.3: Conventional gradient-echo k-space trajectory.

After slice selection, negative phase and frequency encode gradients[1] are applied to move the k-space trajectory to the bottom left hand corner. A frequency-encode gradient is then applied to traverse k-space in the k_x direction. Next, a less negative phase-encode gradient is applied following an r.f. pulse to move the k-space trajectory one step along the k_y direction. Again, the frequency-encode gradient is applied. This process is repeated as many times as necessary to fill all of k-space.

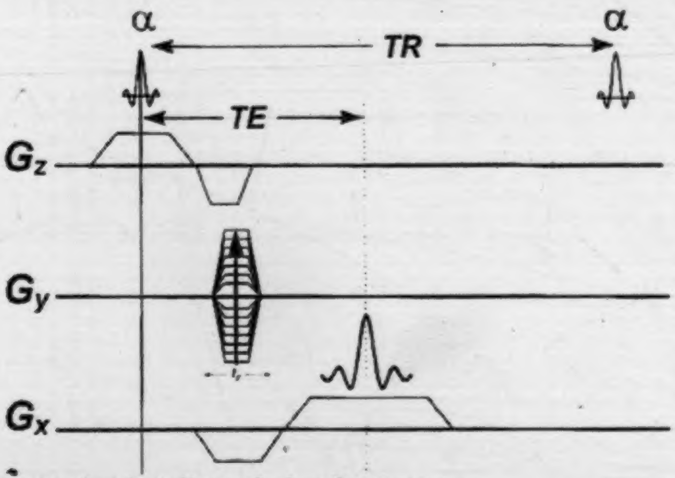

Figure 2.7.4: Conventional gradient-echo imaging sequence.

In a fast imaging technique such as Echo Planar Imaging, all of k-space is sampled after one excitation with very large and fast-switching gradient fields. Figure 2.7.5 shows the raster-like k-space trajectory which is achieved by both positive and negative polarity readout gradients (Figure 2.7.6).

---

[1] Known as dephasers.

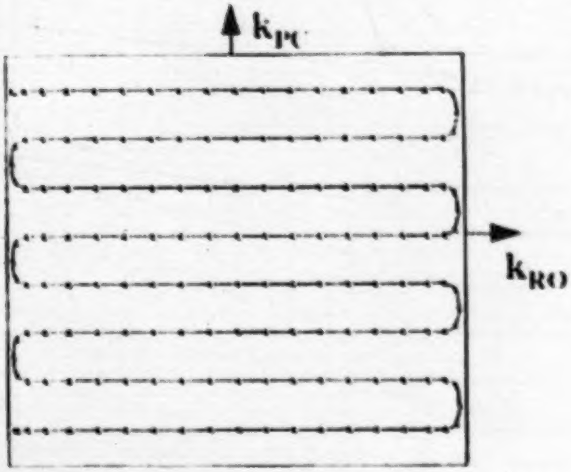

Figure 2.7.5: Echo planar imaging k-space trajectory.

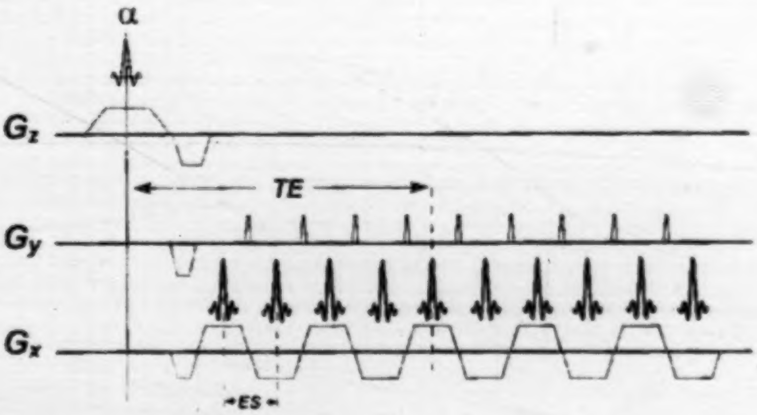
α
G_z
TE
G_y
G_x
ES

Figure 2.7.6: Echo planar imaging sequence.

2.8 Conclusions

In this chapter, the steps to producing an image in MRI – including preparation, excitation, acquisition and spatial-encoding – were introduced to the reader. The next few chapters build on this knowledge to discuss Echo Planar Imaging in detail, a fast imaging sequence with very unique characteristics. Echo planar imaging is especially utilized in functional MRI when the need for speed is of paramount importance.

References

1. E. M. Parcell, H. C. Torrey, R. V. Pound, Resonance absorption by nuclear magnetic moments in a solid. *Phys. Rev.* **69**, 37 (1946).

2. F. Bloch, W. Hansen, M. Packard, Nuclear induction. *Phys. Rev.* **69**, 127 (1946).

3. F. Schmitt, M. K Stehling, R. Turner, Echo Planar Imaging: Theory, Technique and Application, Springer-Verlag Berlin, Heidelberg (1998).

4. J. P. Hornak, The Basics of NMR (software package), Copyright © 1997-99.

5. M. J. Bronskill, S. J. Graham, NMR Characteristics of Tissue. The Physics of MRI 1992 AAPM Summer School Proceedings, American Institute of Physics Inc. Woodbury, NY (1993).

6. P. C. Lauterbur, Image formation by induced local interactions: examples employing nuclear magnetic resonance. *Nature* **242**, 190 (1973).

7. P. Mansfield, Multi-planar image formations using NMR spin echoes. *J. Phys. C.* **10**, L55-58 (1977).

8. P. Mansfield, I. L. Pykett, Biological and medical imaging by NMR. *J. Magn. Reson.* **29**, 355-372 (1978).

9. P. Mansfield, P. K. Grannell, NMR 'diffraction' in solids? *J. Phys. C.* **6**, L422-426 (1973).

10. P. S. Allen, Some fundamental principles of nuclear magnetic resonance. The Physics of MRI 1992 AAPM Summer School Proceedings, American Institute of Physics Inc. Woodbury, NY (1993).

11. R. C. Weast, Handbook of Chemistry and Physics, 53, Chemical Rubber Company. Cleveland, Ohio (1972).

12. R. Gabillard, A steady state transient technique in nuclear magnetic resonance. *Physiol. Rev.* **85**, 694-705 (1952).

13. R. J. Ordidge, R. Coxon, A. Howseman, B. Chapman, R. Turner, M. Stehling, P. Mansfield, Snapshot head imaging at 0.5T using the echo planar technique. *Magn. Reson. Med.* **8**, 110-115 (1988).

14. R. R. Rzedzian, I. L. Pykett, Instant images of the human heart using a new, whole-body MR imaging system. *Am. J. Roentgenol.* **149**, 245-250 (1987).

15. S. Ljunggren, A simple graphical representation of Fourier based imaging methods. *J. Magn. Reson.* **54**, 338-343 (1983).

16. S. J. Riederer, Spatial encoding and image reconstruction. The Physics of MRI 1992 AAPM Summer School Proceedings, American Institute of Physics Inc. Woodbury, NY (1993).

17. W. A. Edelstein, J. M. S. Hutchison, G. Johnson, T. Redpath, Spin warp NMR imaging and applications to human whole body imaging. *Phys. Med. Biol.* **25**, 751-756 (1980).

3 Functional Magnetic Resonance Imaging

In the 17th century, many scientists believed that all areas of the brain work together for every task since the apparent surface of the brain looks uniform. The famous physician Thomas Gall however argued that specific brain regions were associated with specific brain functions. His work led to the notion of "cortical functional localization".

Neural activity associated with a mental process is hard to localize without directly placing electrodes in the brain. Before the advent of functional imaging, studies of patients with focal brain damage led to the observation that a brain region is necessary rather than just involved in a mental process. Nonetheless, lesion studies are limited since the brain organizes itself after damage. Functional localization is also more difficult as brain damage affects large regions and disrupts neural pathways carrying information to other cortical regions involved in the mental process.

Magnetic resonance imaging has become the tool of choice in the past two decades for studying brain activation. Its major attraction is its non-invasive nature and the ease in replicating results which allows for longitudinal and group subject studies.

In this chapter, Functional MRI (*fMRI*) is introduced to the reader. This is followed by introducing the BOLD effect and an overview of it bio-physical source, namely magnetic susceptibility and the extravascular and intravascular effects. The chapter concludes by presenting key literature review on the effect of field strength on the BOLD effect.

3.1 Physiological Basis of fMRI

In 1986, Fox and Raichle [15] showed with PET that neural activity is followed by local physiological changes in brain. The following chart summarizes these changes:

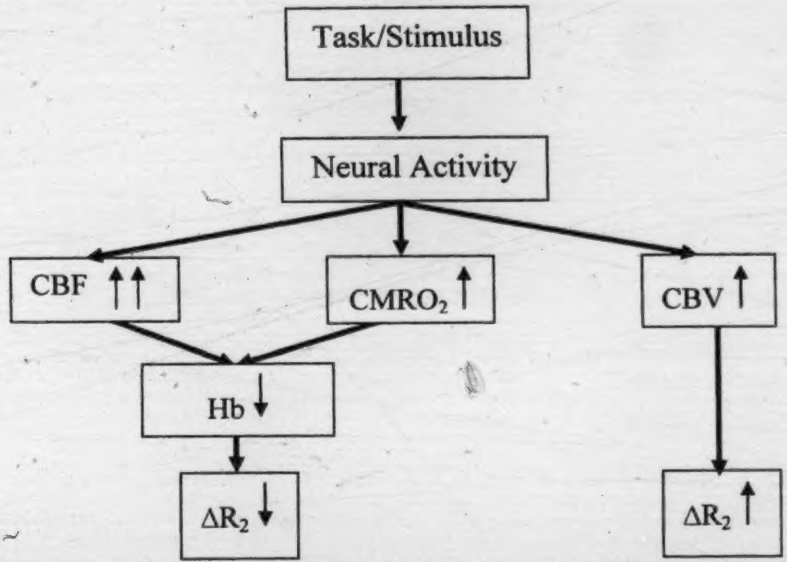

Figure 3.1.1: Summary chart of physiological/metabolic changes that follow neural activity. Note that the double arrow (inside boxes) indicates a greater relative change than a single arrow.

The physiological processes following brain activation are not definitely understood. What is certain is that following neural activity, blood flow (*CBF*) increases substantially, blood volume (*CBV*) increases moderately and oxygen metabolic rate (*CMRO$_2$*) increases slightly – a 40% increase in CBF is usually associated with a 5% increase in CMRO$_2$.

3.1.1 Hemodynamic Response Function

The physiological responses - known collectively as the hemodynamic response function (*HRF*) - do not follow neural activity instantly.

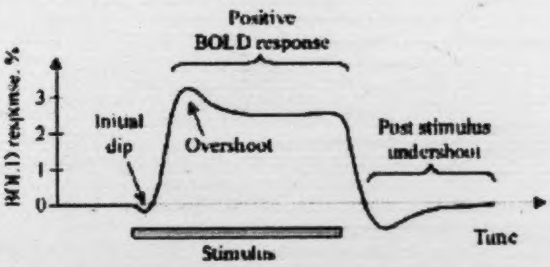

Figure 3.1.2: Hemodynamic Response Function following neural activity. Some characteristics of HRF are an initial dip, an overshoot and a post-stimulus undershoot.

Indeed, there is a delay of approximately 8 seconds between the onset of the stimulus and the peak of HRF[2]. Because of this time latency, there has been a hot debate over fMRI accuracy in measuring the magnitude and site of neural activity. This situation is also worsened by the fact that HRF shape and amplitude varies with the stimulus type, between different subjects and brain regions.

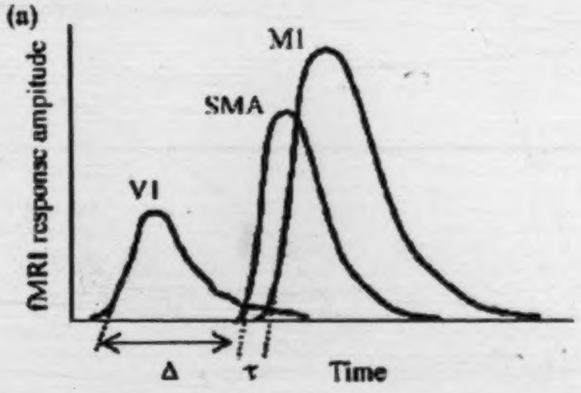

Figure 3.1.3: HRF in the primary visual cortex (V1), supplementary motor area (SMA) and motor cortex (M1).

For the stimulus types presented in chapter 6, it can be safely assumed that HRF has a latency of 8 seconds and is sustained for approximately 30 seconds.

3.2 The BOLD Effect

There are two techniques in magnetic resonance imaging for studying brain activation: 1) perfusion and 2) blood-oxygenation level dependent (*BOLD*) effect. Perfusion is based on quantifying T_1 contrast of CBF. The BOLD effect is based on T_2^* contrast which is dependent on the close but incongruous coupling between CBF and $CMRO_2$. This thesis explores the latter method.

3.2.1 Historical Overview

Functional MRI based on the BOLD effect has only been around for two decades. In 1982, Thulborn [7] showed that blood T_2 is dependent on changes in blood oxygenation. Ogawa [23] in 1990 used rodent models at 7T to measure the change in MR signal in response to changes in blood oxygenation. Meanwhile, Turner in 1991 [19] showed that a reduction in blood oxygenation leads to a decrease in T_2^* and a corresponding drop in MRI signal. A year later, Belliveau [5], Frahm [3], Kwong [6] and Ogawa [21] showed that brain stimulation in humans produces a local increase in T_2^* in the primary visual and motor cortices- i.e. a signal increase which is more observable in gradient-echo images. Ogawa coined this technique "blood oxygenation level dependent contrast" or BOLD. Nature has conveniently provided deoxyhemoglobin as an endogenous contrast agent for studying brain activation.

---

[2] There is a two second delay after the stimulus onset, followed by a rise time of six seconds before the signal's peak plateau.

3.2.2 The Physical Basis of the BOLD Effect

The degree of magnetization –i.e. magnetic susceptibility - of a material in the presence of a magnetic field depends on its magnetic properties. There are several contributors to a material's magnetic properties: the dipole moment of proton spins and unpaired electrons, and the orbital motion of electrons. The dipole moment of proton spins that gives rise to NMR signal is three orders of magnitude smaller than the dipole moment of electrons. Thus, the electron magnetic moment leads to a greater magnetic effect.

Material can be classified into ferromagnetic, diamagnetic and paramagnetic in terms of their magnetic properties. When these materials are placed in a magnetic field, the magnetic dipole moments interact with the main magnetic field and distort the local magnetic field:

$$\begin{aligned} B_{local} &= (1+\chi)B_o \\ &= B_o + \chi B_o \\ &= B_o + M, \end{aligned} \tag{43}$$

where χ is the magnetic susceptibility factor and M is the local magnetization.

A material is paramagnetic if the magnetic dipole moments line up with the applied magnetic field and diamagnetic if they line up opposite to the magnetic field. For a paramagnetic material, unpaired electrons dominate the magnetic properties whereas for a diamagnetic material, it is the orbital motion of electrons.

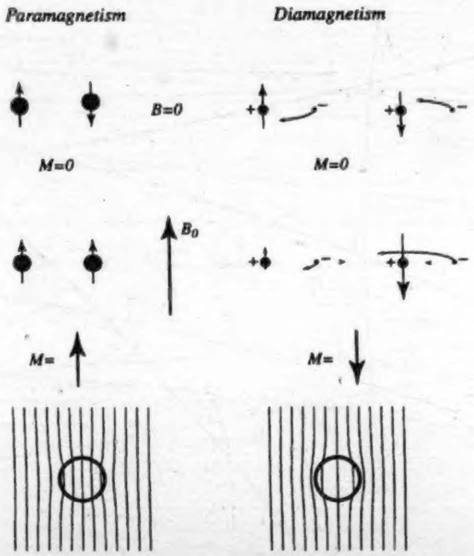

Figure 3.2.1: Paramagnetism and diamagnetism. Magnetic dipole moments (unpaired electrons and nuclei) align with the magnetic field to produce a magnetization aligned with B_0 (paramagnetism, left). The magnetic dipole moments due to the orbital motions of electrons are altered to produce a net magnetization aligned opposite to the field (diamagnetism, right). The bottom row shows distortions of uniform magnetic field lines by a magnetized sphere [16].

Tissue and OxyHemoglobin (*HbO_2*) are diamagnetic whereas deOxyHemoglobin (*Hb*) is paramagnetic. The following table lists the magnetic susceptibility values for some relevant material:

Table 3.2.1: Magnetic susceptibility values for different material [11].

Material	*X (ppm)*
Water	-8.8
Hb	0.3
Air	3.6
Iron	>>1000

Note from Table 3.2.1 that χ is positive for paramagnetic materials (adds to the local magnetic field) and negative for diamagnetic materials (subtracts from the local magnetic field).

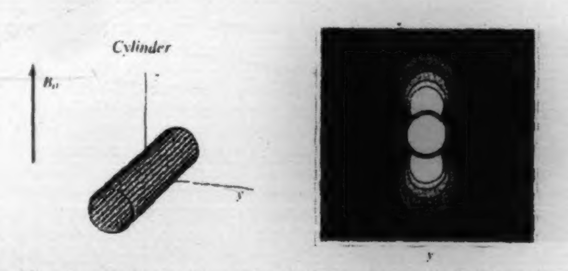

Figure 3.2.2: Hb in a blood vessel creates a dipole-like magnetic field in the tissue space around it due to differences in magnetic susceptibility in these two regions.

When two different materials exist in close proximity, a field gradient is produced due to the different local magnetic fields. Thus, the field homogeneity is degraded at their boundary. In deoxygenated blood, large field gradients are produced in and around blood cells. Thus, proton spins in the tissue space surrounding blood vessels feel dipolar field gradients (Figure 3.2.2) and as a result precess with different frequencies. Over time, the spins accumulate different phases at time TE, T_2* decays faster and the measured signal is reduced. Unlike Hb, HbO_2 is diamagnetic as is the tissue space around it. There are no gradient fields and no effect on the measured signal at time TE. As is apparent from this discussion, the measured signal varies as the blood oxygenation level changes. The following section lists the steps to obtaining functional brain maps.

3.2.3 Functional Activation Maps

Brain activation maps are obtained as follows:

1) The subject is stimulated such that neural response is restricted as best as possible to a local region(s). For instance, a subject is presented with a red and blue flashing checkerboard. The neural response is then restricted to the primary visual cortex (V1).

2) The neural response in the local region leads to an initial increase in the local consumption of oxygen i.e. an increase in Hb concentration in blood. The demand for more oxygen is immediately met by a large increase in CBF. Due to the fresh supply of blood, there is a higher ratio of HbO_2 to Hb. This leads to a higher MR signal.

3) The task state is alternated with a control (rest) state where the concentration of Hb returns to baseline levels. For the flashing checkerboard example, the subject may be asked to look at a black screen to produce this effect.

4) The difference in MR signal intensity between the "task" and "rest" states leads to bright spots on functional images which are interpreted as brain activation.

The changes in MR signal intensity during the task and rest states – i.e. changes in the blood oxygenation – is referred to as the BOLD effect.

3.3 The BOLD Effect Components

An imaging region contains tissue and blood vessels of all sizes. Ogawa [22, 23] and Gati [4] have shown that changes in MR signal come from both blood vessels and the tissue space surrounding them. Ogawa categorized the BOLD effect as extravascular (*EV*) and intravascular (*IV*). Brain activation is best described by the tissue space, i.e. EV effect – since large blood vessels may be distal to the site of neural activity.

3.3.1 The Extravascular Effect

The extravascular effect is dominated by large veins. This can be explained by considering two factors separately in large and small vessels: 1) the degree of change in blood oxygenation levels during neural activity and 2) the magnetic susceptibility effect.

At rest, venous blood contains approximately 60% HbO_2. During brain activation, HbO_2 concentration increases to more than 70%. For capillaries, this change is from 80-85% which is less dramatic than changes in veins. To consider the second factor, it is important to include diffusion in the discussion. Diffusion implies that water protons do not stay in one place but move around in the tissue space surrounding the blood vessels.

3.3.2 Diffusion

Imagine a blood vessel perpendicular to the B_o field. The presence of Hb in the blood vessel causes a gradient field in the tissue space around it (refer to section 3.2.2). Note in Figure 3.3.1 that the radius, and not the length of the blood vessel, affects the extent of the gradient fields in the extravascular space. For this reason, only the cross-sectional plane of the blood vessel needs to be considered.

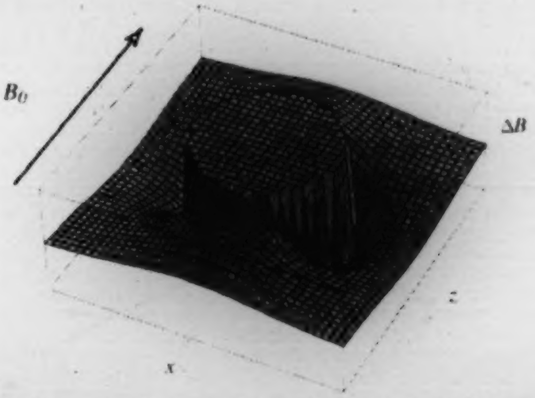

Figure 3.3.1: Field distortions around a magnetized blood vessel. A single magnetized cylinder oriented perpendicularly to the magnetic field B_o creates field offsets (ΔB) in the surrounding space, with the field increased along the main field axis and decreased along a perpendicular axis [16].

The average displacement of water protons can be calculated as $\sqrt{4DT}$ where the water diffusion constant $D \sim 1\mu m^2/ms$ in brain. At 4.7T and with a typical TE of 25ms, the average water displacement is $10\mu m$.

If the radius of the blood vessel is that of a vein ($d > 30\mu m$), the gradient fields produced are large compared to the diffusion distance ($10\mu m$). As a result, water protons feel approximately a constant magnetic field and accumulate a net phase which reduces the MR signal significantly.

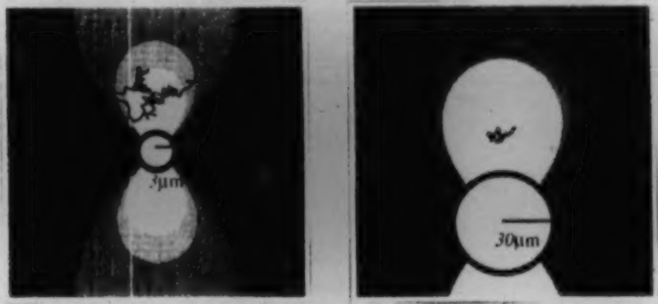

Capillary *Venule*

Figure 3.3.2: Diffusion produces an averaging over field offsets that is more effective for the smallest vessels. The random walk of a diffusing water molecule is shown as wiggly black line over-layed on the field distortion pattern around a capillary (left) and a venule (right) [16].

On the other, if the radius of the blood vessel is that of a capillary ($d < 3\mu m$), the gradient fields produced are small compared to the diffusion distance of $10\mu m$. As a result, water protons feel a dynamic range of magnetic fields which results in averaging of the phase over time. This averaging effect actually results in little phase dispersion.

As a result of diffusion, the signal drop around large veins is much greater than the capillary bed for the same level of blood oxygenation. Gradient-echo imaging sequences are sensitive to the EV effect for vessels of all sizes (Figure 3.3.3).

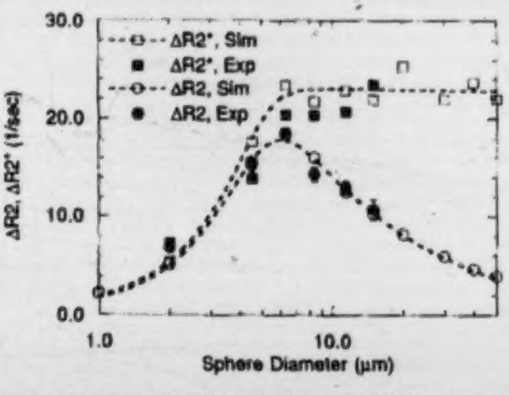

Figure 3.3.3: Spin-echo and gradient-echo T_2 and T_2* sensitivities to vessels of different diameters [17]. Spin-echo is more sensitive for smaller vessels (peaks around 7μm). Gradient-echo on the other hand is sensitive to vessels of all sizes.

Since water protons around large draining veins accumulate a net phase due to a constant magnetic field, the application of a 180° r.f. pulse refocuses these spins. This refocusing pulse is not as effective around the capillary bed due to the dynamic averaging effect. As a result, spin-echo imaging sequences map more closely to the capillary bed and as such are more specific to the site of neural activity than the gradient-echo imaging sequences. However, SE is less sensitive to the BOLD effect since some of the EV effect around the capillaries is nonetheless refocused.

3.3.3 The Intravascular Effect

The IV effect in general does not correlate well with the site of neural activity. Even though blood vessels occupy only 4% of the total tissue volume, the IV effect is comparable to EV effect due to the large gradient fields produced by Hb in blood vessels. The IV effect is intrinsically reduced at high magnetic fields since T_2 of blood becomes much shorter ($T_{2v,4.7T} = 22$ms, $T_{2v,1.5T} = 181$ms [10]). The use of long TE, especially feasible with spin-echo sequences, suppresses the IV component of the BOLD effect. Lee [24] showed that the IV contribution to the SE BOLD signal is 60% at 1.5T, **8% at 4.7T** and 1% at 9.4T. Thus, SE is more specific to the location of neural activity, but it less sensitive to the BOLD effect than GRE.

3.4 Field Strength and the BOLD Effect

Many studies have shown that fMRI at high field benefits from a higher signal to noise ratio (*SNR*), greater BOLD effect and more specificity to the actual site of activation. In fact, the "optimal" magnetic field strength for fMRI purposes has been the subject of further investigation [20].

The maximum BOLD contrast to noise ratio (*CNR*) is calculated as,

$$\Delta S/_{N}|\text{max} = S_o/_{N} * \Delta R_{2^*}/_{R_{2b^*}}, \qquad \textbf{(44)}$$

where S_o/N is the signal-to-noise ratio at TE = 0 in a fully-relaxed proton-density weighted GRE image, R_2* is the apparent transverse relaxation rate, and ΔR_2* is the change in the apparent transverse relaxation rate give by:

$$\Delta R_{2^*} = -\Delta S / S/_{TE}, \qquad \textbf{(45)}$$

where $\Delta S/S$ represents the fractional BOLD signal change, measured from functional maps (for more information on how Eqn. 44 and 45 are derived, refer to [4]). As seen in Eqn. 44, the BOLD CNR depends heavily on the available SNR and the R_2* contrast. Note that there is no standard method of measuring SNR in MRI. The method employed in chapter 6 consists of calculating the ratio of the mean signal in a ROI in brain and the standard deviation (SD) of noise in the background (free from artifacts). Since only magnitude images are employed however, the measured SD of noise is lower and may be corrected for a more accurate SNR measurement [14]. Due to inaccessibility of raw data at 1.5T system, the most commonly applied method of background noise estimation [1] was used however which may give an error of 4% in noise SD estimation for a 500-600 pixel region in the background.

Hoult [2], Gati [4], and Edelstein [25] showed a linear dependence of SNR to static field strength. In addition, Ogawa [22, 23] proposed that ΔR_2^* and thus the BOLD effect are proportional to B_o for large vessels and proportional to B_o^2 for small vessels and capillaries. Gati [4] and Turner [20] showed experimentally that the maximum BOLD CNR increases greater than linearly in tissues and less than linearly in blood vessels with B_0. These results demonstrated that high field fMRI is more localized to the site of neuronal activity, i.e. capillary bed. The preceding literature results have suggested that functional MRI at high fields carries some major advantages such as higher SNR, higher sensitivity (CNR) as well as more specificity to the site of neural activation.

3.5 Conclusions

This chapter introduced the reader to functional MRI and the physiological and physical basis of the BOLD effect. The extravascular and intravascular effects were discussed in conjunction with gradient and spin echo imaging sequences. The effect of the magnetic field on the BOLD signal was also discussed by mentioning several significant literature reviews in this area.

References

1. C. D. Constantinides, E. Atalar, E. R. McVeigh, Signal-to-noise measurements in magnitude images from NMR phase arrays. *Magn. Reson. Med.* **12**, 232-233 (1985).

2. D. I. Hoult, C. N. Chen, V. J. Sank, The field dependence of the nuclear magnetic resonance experiment. *J. Magn. Reson.* **24**, 71-85 (1986).

3. J. Frahm, H. Bruhn, K. D. Merboldt, W. Hanicke, Dynamic MR imaging of human brain oxygenation during rest and photic stimulation. *J. MRI* **2**, 501-505 (1992).

4. J. S. Gati., R. S. Menon, K. Ugurbil, K. Rutt, Experimental determination of the BOLD field strength dependence in vessels and tissue. *Magn. Reson. Med.* **38**, 296-302 (1997).

5. J. W. Belliveau, D. N. Kennedy, R. C. Mckinstry, B. R. Buchbinder, R. M. Weisskoff, M. S. Cohen, J. M. Vevea, T. J. Brady, B. R. Rosen, Functional mapping of the human visual cortex by magnetic resonance imaging. *Science* **254**, 716-719 (1991).

6. K K. Kwong, J. W. Belliveau, D. A. Chesler, I. E. Goldberg, R. M. Weisskoff, B. P. Poncelet, D. N. Kennedy, B. E. Hoppel, M. S. Cohen, R. Turner, H-M. Cheng, T. J. Brady, B. R. Rosen. Dynamic magnetic resonance imaging of human brain activity during primary sensory stimulation. *Proc. Natl. Acad. USA* **89**, 5675-5679 (1992).

7. K. R. Thulborn, J. C. Waterton, P. M. Matthews, G. K. Radda, Oxygenation dependence of transverse relaxation time of water protons in whole blood at high field. *Biochem. Biophys. Acta.* **714**, 265-270 (1982).

8. L. M. Klassen, R. S. Menon. NMR simulation analysis of statistical effects on quantifying cerebrovascular parameters. *Biophys. J.* **92**, 1014-1021 (2007).

9. L. Pauling, C. D. Coryell. The magnetic properties and structure of hemoglobin, oxyhemoglobin, and carbon monoxyhemoglobin. *Proc. Natl. Acad. Sci. USA.* **22**, 210–216 (1936).

10. M.-E. Meyer, O. Yu, B. Eclancher, D. Grucker, J. Chambron, NMR relaxation rates and blood oxygenation level. *Magn. Reson. Med.* **34**, 234-241 (1995).

11. M. J. Bronskill, S. J. Graham. NMR Characteristics of Tissue. The Physics of MRI 1992 AAPM Summer School Proceedings, American Institute of Physics Inc. Woodbury, NY (1993).

12. M. K. Stehling, F. Schmitt, R. Ladebeck, Echo-planar imaging of human brain oxygenation changes. *J. Magn. Reson.* Imaging **3**, 471-474 (1993).

13. P. Jezzard, P. M. Matthews, S. M. Smith. Functional MRI: An introduction to methods, Oxford University Press Inc. New York, NY (2001).

14. P. Kellman, E. R. McVeigh, Image reconstruction in SNR units: a general method for SNR measurements. *Magn. Reson. Med.* **54**, 1439-1447 (2005).

15. P. T. Fox, M. E. Raichle, Regional uncoupling of cerebral blood flow and oxygen metabolism during focal physiological activation: A positron emission tomographic study. *J. Cereb. Blood Flow & Metab.* **5**, S177-178 (1985).

16. R. B. Buxton. Introduction to Functional Magnetic Resonance Imaging Principles and Techniques, Cambridge University Press USA (2002).

17. R. M Weisskoff, C. S. Zuo, J. L. Boxerman, B.R. Rosen, Microscopic susceptibility variation and transverse relaxation theory and experiment. *Magn. Reson. Med.* **31**, 601-610 (1994).

18. R. S. Frackowiak, K. J. Friston, C. D. Frith, R.J. Dolan, J.C. Mazziotta. Human Brain Function, Academic Press Toronto, Canada (1997).

19. R. Turner, D. Le Bihan, C. T. Moonen, D. Despres, J. Frank, Echo-planar time course MRI of cat brain deoxygenation changes. *Magn. Reson. Med.* **22**, 159-166 (1991).

20. R. Turner R, P. Jezzard, H. Wen, K. K. Kwong, D. Le Bihan, T. Zeffiro, R. S. Balaban, Functional mapping of the human visual cortex at 4 and 1.5 Tesla using deoxygenation contrast EPI. *Magn. Reson. Med.* **29**, 277-279 (1993).

21. S. Ogawa, D. W. Tank, R. Menon, J. M. Ellermann, S.-G. Kim, H. Merkle, K. Ugurbil, Intrinsic signal changes accompanying stimulation: Functional brain mapping with magnetic resonance imaging. *Proc. Natl. Acad. Sci. USA* **89**, 5951-5955 (1992).

22. S. Ogawa, R. S. Menon, D.W. Tank, S. G. Kim, H. Merkle, J. M. Ellerman, K. Ugurbil, Functional brain mapping by blood oxygenation level-dependent contrast magnetic resonance imaging. A comparison of signal characteristics with a biophysical model. *Biophys. J.* **64**, 803-812 (1993).

23. S. Ogawa, T.-M. Lee, A. S. Nayak, P. Glynn, Oxygenation-sensitive contrast in magnetic resonance image of rodent brain at high magnetic fields. *Magn. Reson. Med.* **14**, 68-78 (1990).

24. S. P. Lee, A. C. Silva, K. Ugurbil, S.G. Kim, Diffusion-weighted spin-echo fMRI at 9.4T: Microvasculature/tissue contribution to BOLD signal changes. *Magn. Reson. Med.* **42**, 919-928 (1999)

25. W. A. Edelstein, G. H. Glover, C. J. Hardy, R. W. Redington, The intrinsic signal-to-noise ratio in NMR imaging. *Magn Reson. Med.* **3**, 604-618 (1986).

4 Single-shot Echo Planar Imaging

Echo planar imaging was invented by Sir Peter Mansfield [12] in 1970's. Due to the fast capability of this imaging protocol, EPI requires advanced hardware equipments and software post-processing solutions which have been addressed only in the past decade.

This chapter introduces the reader to single-shot echo planar imaging and its variations, namely spin-echo and gradient-echo EPI. Due to the rapid oscillation of the long readout gradient, EPI is prone to image artifacts which are unique to this imaging protocol. Nyquist ghosts, image distortions and blurring in images are discussed thoroughly in section 4.3.

Section 4.4 discusses parameter optimization prior to data acquisition for the best feasible image quality at 4.7T with available hardware capabilities. The final section presents post-processing methods using a single reference data set.

4.1 Conventional Imaging

As discussed in chapter 2 , in conventional imaging techniques, a readout gradient is applied along one direction during signal acquisition and a phase-encode gradient is applied briefly along the second orthogonal direction prior to readout. This process is repeated with separate excitations for as many phase-encode lines as necessary.

The following flow chart summarizes the conventional imaging scheme:

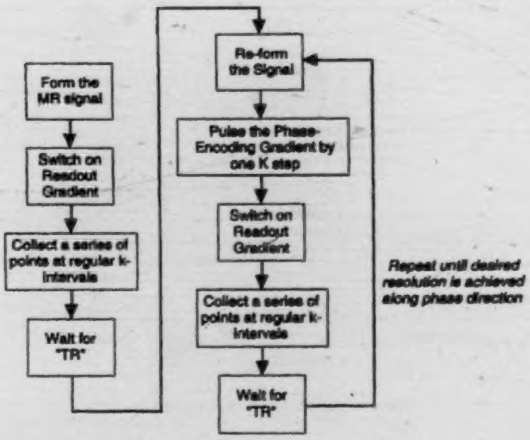
Form the MR signal
Switch on Readout Gradient
Collect a series of points at regular k-intervals
Wait for "TR"
Re-form the Signal
Pulse the Phase-Encoding Gradient by one K step
Switch on Readout Gradient
Collect a series of points at regular k-intervals
Wait for "TR"
Repeat until desired resolution is achieved along phase direction

Figure 4.1.1: Flow chart for the conventional gradient-encode scheme.

4.1.1 Echo Planar Imaging (EPI)

As seen in Figure 4.1.1, each line of k-space is acquired after an excitation pulse. As a result, conventional imaging techniques are slow and time-consuming. For fast imaging applications such as functional MRI (refer to chapters 3 and 5), EPI is employed where the entire k-space grid is acquired following a single excitation pulse. The following chart summarizes EPI:

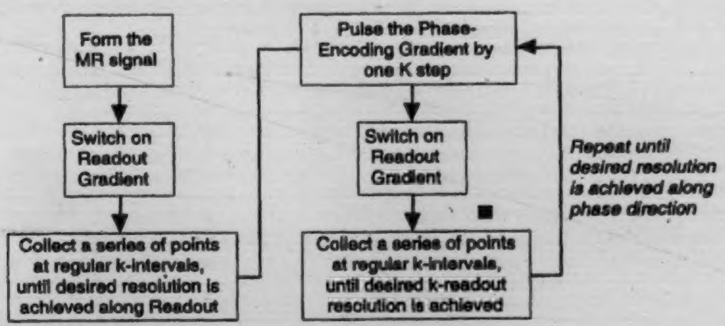
Form the MR signal
Switch on Readout Gradient
Collect a series of points at regular k-intervals, until desired resolution is achieved along Readout
Pulse the Phase-Encoding Gradient by one K step
Switch on Readout Gradient
Collect a series of points at regular k-intervals, until desired k-readout resolution is achieved
Repeat until desired resolution is achieved along phase direction

Figure 4.1.2: Flow chart for echo planar imaging sequence. Note that there is no reform of the signal. All of k-space is sampled after one excitation.

The k-space trajectory and imaging sequence for EPI were introduced in Figure 2.7.5 and Figure 2.7.6. Note that the raster-like k-space scan is achieved with positive and negative polarity readout gradients. The brief blip of the phase-encode gradient moves the data from line to line.

Since only one excitation pulse is applied in EPI, it is of paramount importance that all of k-space is sampled before the signal decays significantly (TE <= T_2^*). As a result, EPI puts enormous demands on acquisition and sampling hardware. The advancement in hardware technology in the past decade has resulted in leaps in echo planar imaging applications, especially at high fields where the rapid T_2* decay creates major challenges (T_2^*:20-30ms at 4.7T).

To show EPI hardware requirements, consider a 64x64 image with an isotropic in-plane resolution of 4mm. In order to sample all of k-space in a time less than T_2* decay at 4.7T, a gradient amplitude of 2.6 G/cm must be applied along with ramp-sampling and a bandwidth of 300 KHz. The Varian Inova 4.7T system in our lab currently has a G_{max} of 3.5 G/cm and maximum bandwidth of 400 KHz.

4.2 EPI sequence variations

4.2.1 Gradient-echo EPI

Gradient-echo EPI is the simplest form of an echo planar imaging sequence as only an initial r.f. pulse is applied.

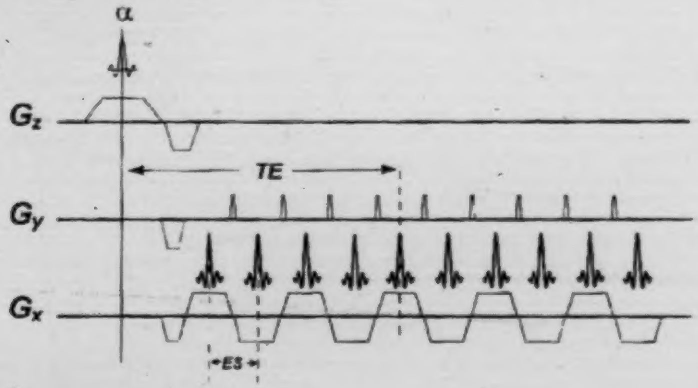

Figure 4.2.1: GRE-EPI sequence.

Gradient-echo EPI is T_2* weighted and may suffer from severe image artifacts. Section 4.3 discusses EPI image artifacts in detail.

4.2.2 Spin-echo EPI

Following an initial excitation pulse, a 180° r.f. pulse is applied prior to complete k-space sampling.

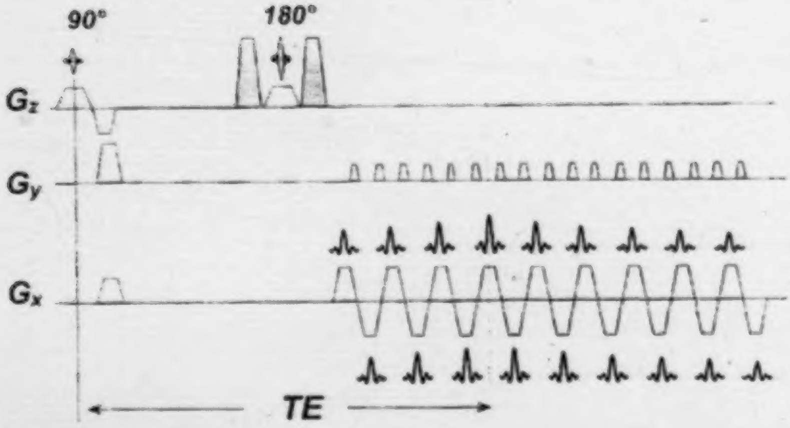

Figure 4.2.2: SE-EPI sequence.

As a result of the single refocusing pulse, spin echo EPI is less susceptible to blurring and static field inhomogeneities.

4.3 EPI Artifacts

Echo planar imaging is a fast acquisition technique, employed when high temporal resolution is needed e.g. functional MRI. EPI images suffer from many artifacts, and consequently image reconstruction is much more than just applying a simple inverse Fourier transform to the acquired k-space data. The following section outlines the most common EPI artifacts.

4.3.1 Nyquist Ghosting

Figure 2.7.6 shows that EPI k-space is acquired after one excitation with positive and negative gradient polarities. Any signal variation between the even and odd echoes results in shifted images of the object known as Nyquist or Half-FOV ghosts.

Nyquist Ghosts are generally caused by:

- Eddy currents
- System timing delays
- B_0 field inhomogeneity, and
- Patient motion

In EPI, a source of ghosting can be eddy currents, which is covered in the following section.

Eddy currents

Echo planar imaging gradients have fast switch rates with very short rise times (Δ in Figure 4.3.1). As a result, the gradient fields couple with the surrounding conductive components of the magnet such as the cryostat and r.f. coils, resulting in eddy currents.

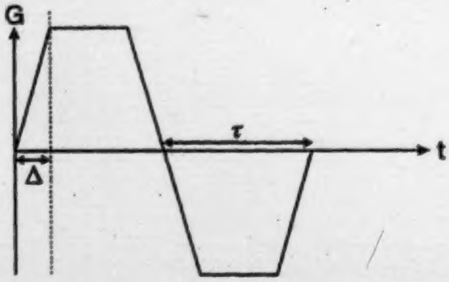

Figure 4.3.1: Every other line in k-space is acquired with a negative polarity gradient.

Eddy currents cause a time lag between the applied voltage driving a gradient and the resultant gradient field. Because of this latency, gradient fields stabilize late and echoes refocus later than the ideal k-space center. Since each second line in k-space must be time-reversed for Fourier transform reconstruction, this time-delay causes a *periodic* crisscross pattern in k-space which translates to ghosting in images.

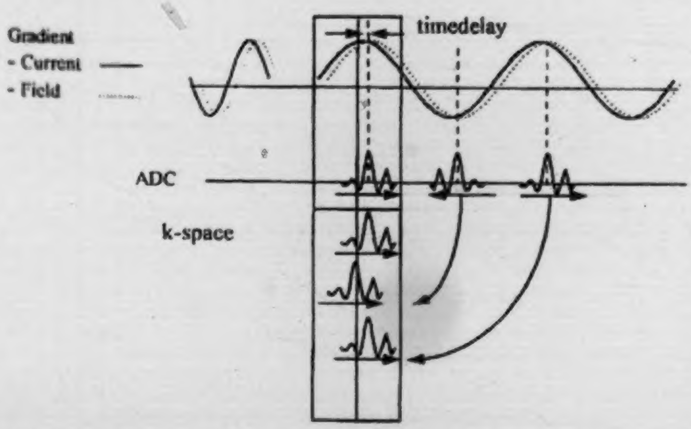

Figure 4.3.2: Eddy currents cause a constant periodic time-delay for every second line in k-space which leads to a periodic crisscross pattern after time-reversal.

The ghosting phenomenon may be explained mathematically using Fourier transform properties. Any shift in k-space, i.e. time delay results in linear phase modulation in the image domain:

$$S(k-k_o) \rightarrow FT \rightarrow S(x,y)e^{ik_o x}, \tag{46}$$

where k_o is the shift in the readout direction and $k_o x$ is the phase modulation in the image domain. Eddy currents in general are reduced by providing compensation currents to the gradient drivers.

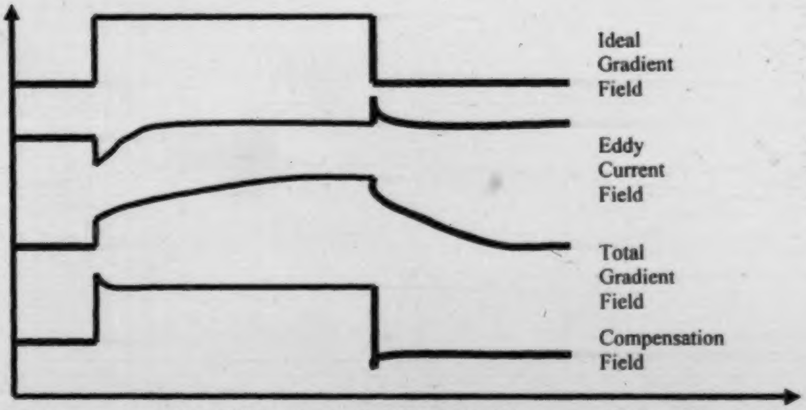

Figure 4.3.3: A compensation field reduces the effect of eddy currents on readout field gradients.

In spite of hardware solutions, eddy currents can not be eliminated entirely and post-processing methods such as phase multiplication are absolutely necessary to reduce ghosting artifacts further.

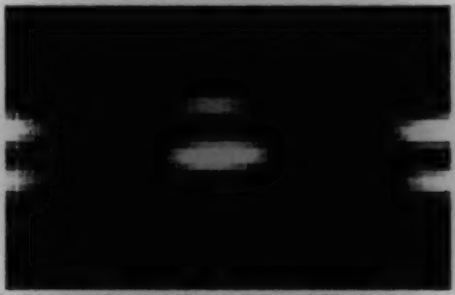

Figure 4.3.4: This original phantom image shows large shifts between odd and even lines, manifested as dark bands in the image.

The amount of phase modulation can be determined by a reference scan immediately prior to the actual image scan. Post-processing of echo planar images using a reference scan is discussed in section 4.5.

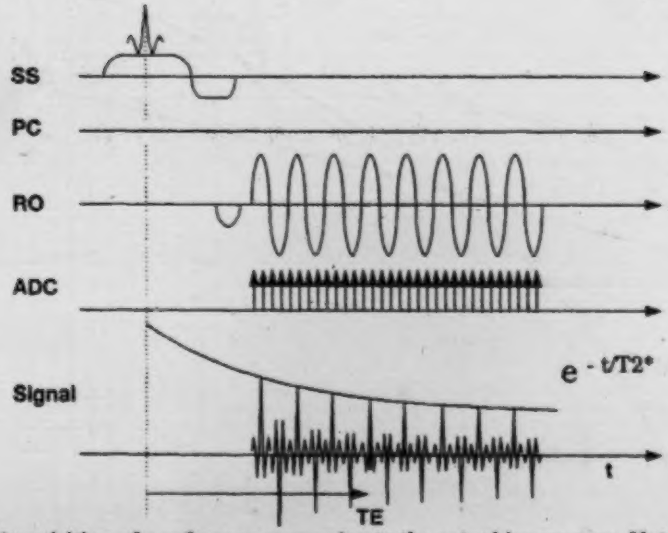

Figure 4.3.5: Acquisition of a reference scan prior to the actual image scan. Note the absence of phase-encode gradients in the reference scan.

4.3.2 Low-bandwidth Artifacts

The MR signal *S (t)* can be written as,

$$S(t) = \int M(x,y) e^{t/T_2^*} e^{i\theta} dxdy, \tag{47}$$

where $\theta = (\Delta\omega + \gamma\Delta B_o)t + \gamma \int G dt$, *Δω* describes off-resonance effects such as chemical shift and *ΔB*$_0$ describes field inhomogeneity sources.

Most artifacts in EPI are present in the phase-encode direction due to the low bandwidth along this direction. As a result, *S(t)* in Eqn. 47 can be written in one dimension (time-domain → k-space):

$$S(k(t)) = \int M(x) e^{ikx} e^{ikd} e^{-k/\gamma G T_2^* x} dx, \tag{48}$$

where $d = \Delta\omega/\gamma G + \Delta B_o/G$ describes pixel displacements due to off-resonance effects and 'field inhomogeneity.

Example 1: To show why bandwidth is lower in the phase-encode direction, consider an in-plane resolution of 4x4 mm. With a sampling rate of 300 KHz at 4.7T, the total acquisition time is 29ms (0.45ms per line). The bandwidth per pixel is then calculated as follows:

$$b_{ro} = 1/T_{ro}, \tag{49}$$

$$b_{pe} = 1/T_{acq} \qquad (50)$$

For this specific example, b_{ro} = *2222 Hz/pixel* and b_{pe} = *34Hz/pixel*. Due to low bandwidth, image artifacts are projected in the phase-encode direction.

Geometric distortions

As was seen in section 2.5, the MR signal is spatially-encoded using gradients. The presence of any field inhomogeneities consequently affects the spatial-encoding process. Geometric distortions are manifested as pixel shifts and signal loss in the phase-encode direction.

Field inhomogeneity comes from two main sources:

- A magnet has a finite length and imperfections in its design and construction. As result, it can not be perfectly homogenous.
- The sample brought into the magnet has intrinsic field inhomogeneities which are most extreme at boundaries with different magnetic susceptibility χ. At the interface, the change in the effective field is $\Delta B = (\chi_1 - \chi_2)B_o$, which causes spins to process with different frequencies, acquire different phases at time TE and combine destructively leading to signal cancellations.

The following figure shows a sagittal slice with its corresponding phase map. Note the presence of large phase variations in the nasal cavity.

Figure 4.3.6: A coronal slice of a human head and its corresponding phase map. Note that the abrupt change in phase from white to black is due to the cyclic nature of phase (-2π to 2π) and not actual abrupt phase change.

The following images were acquired with conventional GRE sequence at 4.7T to demonstrate severe signal loss in the nasal and auditory canals. Note that an increase in echo time results in more signal loss.

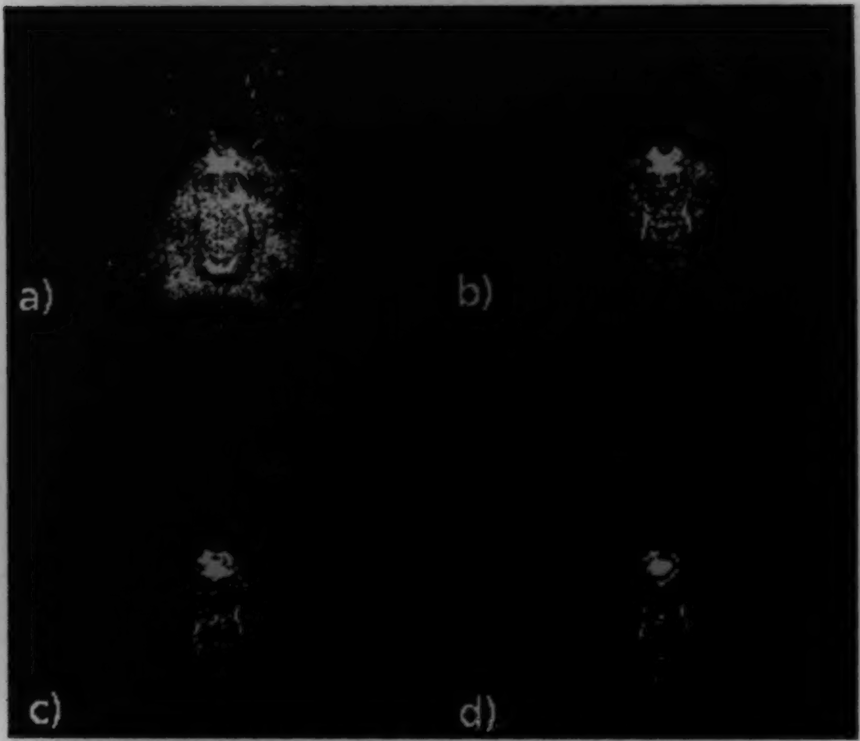

Figure 4.3.7: Conventional GRE images taken with TR: 50ms, 1x1x2mm resolution, a) TE: 10, b) 20, c) 30 and d) 40ms.

In order to explain signal loss in the presence of static field inhomogeneities, consider a negative gradient offset (not constant) in addition to the readout gradient. In the absence of a gradient offset, echoes refocus at the center of k-space. When a negative gradient offset is present, the echoes move gradually to the right of k-space towards the end of the readout window. As the strength of the gradient offset increases beyond that of the readout dephasing gradient the echoes eventually disappear. Consequently, the MR signal is lost.

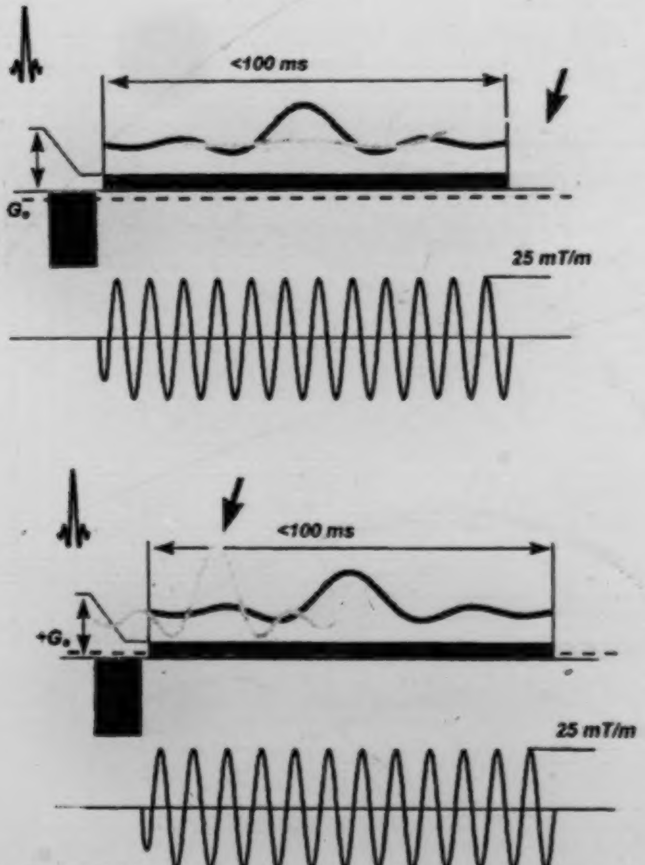

Figure 4.3.8: The presence of a negative (top) or positive (bottom) gradient offset during readout causes signal loss.

If the offset gradient is positive, the echoes get compressed in time and shift towards the start of the readout window. In either case, the echoes ultimately disappear due to dephasing, causing signal loss.

The major problem with field inhomogeneity is that is it spatially varying over the imaging volume. As a result, pixel displacements in the image are not constant. Image displacement (in cm) can be characterized in Eqn. 51:

$$d = \Delta B / G . \qquad \textbf{(51)}$$

The above equation demonstrates that pixel displacements are more severe at high fields and at lower gradient strengths. Several steps can be taken to avoid areas of great B_0 inhomogeneity, e.g. air-tissue interfaces. Smaller voxel dimensions minimize the change in magnetic field within the voxel and reduce intravoxel dephasing. Another trick is to use oblique slices to avoid regions of large magnetic susceptibility differences.

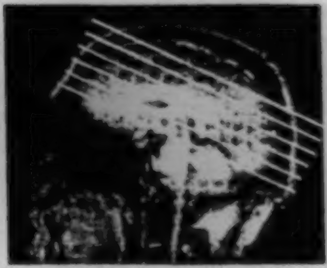

Figure 4.3.9: Use of oblique slices to avoid brain regions with large magnetic susceptibility differences.

It might also be beneficial to swap the direction of the readout and phase-encode gradients. These options and more are explored in detail in section 4.4 .

4.3.3 Constant Gradient Offset

A constant gradient offset (caused by poor shim) causes an increasing echo shift. The following figure shows echo shift in a reference scan on the Varian Inova 4.7T system:

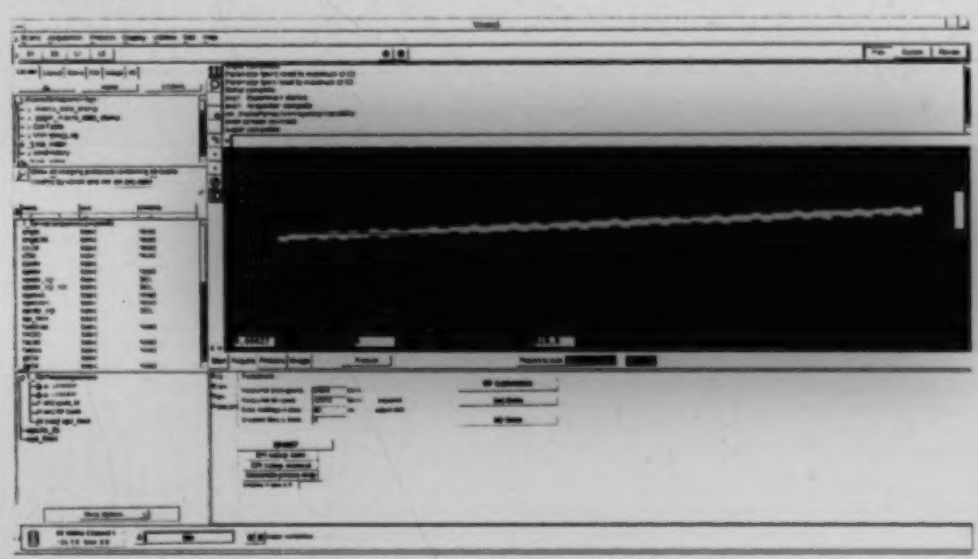

Figure 4.3.10: Echo drift in the presence of a 0.015mT/m gradient offset.

The increasing shift causes the echoes to refocus later than the ideal echo center. This causes an overall image shift.

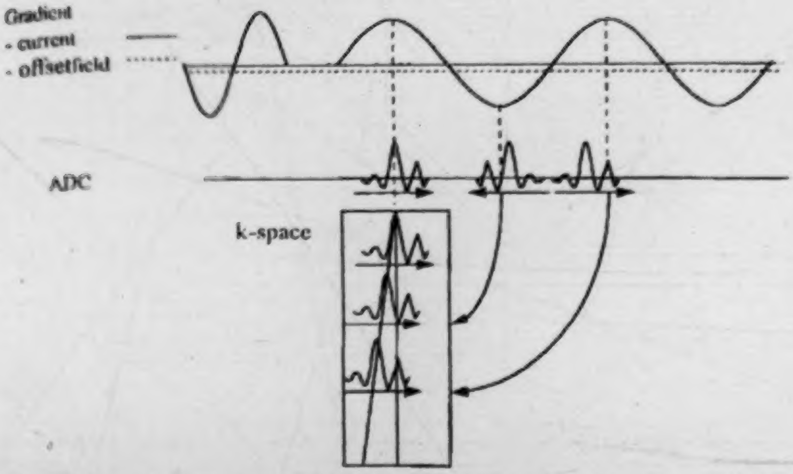

Figure 4.3.11: A constant gradient offset causes an increasing echo shift. However, this is not a source of ghosting since the echo shifts are not periodic from line to line.

The following figure shows the effect of a constant gradient offset on a phantom image:

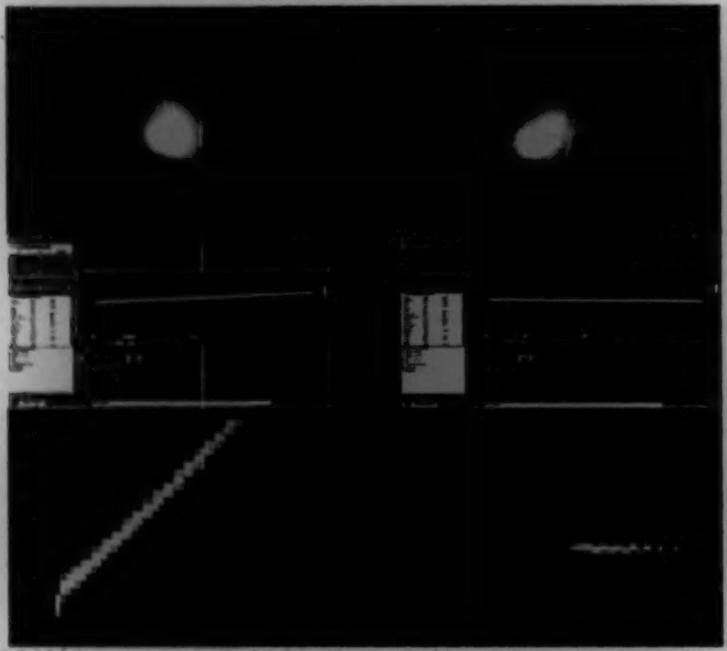

Figure 4.3.12: An uncorrected phantom image (left) and the post-processed image (right). Also shown are Varian Inova 4.7T and Matlab windows of echo drift in the reference scan.

As was discussed in the previous section, the presence of an offset gradient may cause signal loss if it is of a considerable strength compared to readout dephasing gradient.

4.3.4 Chemical Shift

Chemical shift refers to the shift in resonance frequency of nuclear spins in different chemical environments. Chemical shift results in pixel displacements which are more severe in the phase-encode direction in EPI. Eqn. 51 may be rewritten in terms of pixel displacement as,

$$d = \Delta\omega / b = \gamma\Delta B / b, \tag{52}$$

where b is bandwidth per pixel.

Example 2: Using information from example 1, fat-water displacements in the readout and phase encode directions can be calculated at 4.7T using Eqn. 52:

d_{ro} *= (3.5ppm)(200 MHz) / (2222Hz/pixel) = 0.3pixels*
d_{pe} *= (3.5ppm)(200 MHz) / (34Hz/pixel) = 21pixels.*

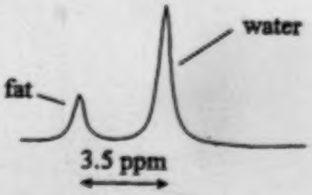

Figure 4.3.13: Fat and water Larmor frequencies differ by 3.5ppm in a homogenous field.

The shift in the readout direction is below a pixel which is negligible. By comparison, the shift in the phase direction is 21 pixels – 33% of the 64 acquired points! As a consequence, an incomplete or lack thereof fat suppression results in large mis-registration between fat and water signals in EPI images.

4.3.5 T2* decay

As was discussed in section 2.3, FID signal decays faster to its equilibrium state in the presence of B_0 field inhomogeneities. In echo planar imaging, the echoes obtained at the end of the echo train are heavily T_2*-weighted as compared to echoes obtained in the beginning. This means that low-frequency spatial components have higher signal intensity than high frequency spatial components. This fact mathematically amounts to multiplying the ideal k-space data with an exponential signal envelope which in image domain translates as convolution with a low pass filter. The convolution process leads to signal intensity smearing over a larger region which is referred to as image blurring or loss of resolution.

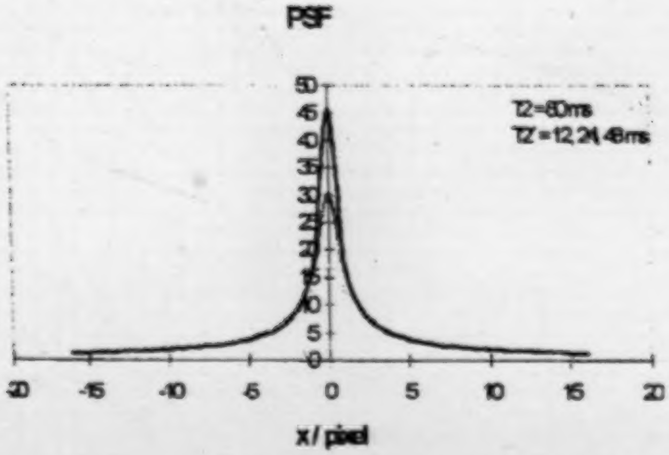

Figure 4.3.14: The effect of increasing B_o field inhomogeneity (T_2') on point spread function (*PSF*)[3]. Note that as T_2* decreases, PSF broadens and signal intensity decreases.

The signal loss due to T_2* relaxation is especially worse at high fields due to shorter T_2* decay and greater B_o inhomogeneity. Shimming makes the B_o field more homogeneous in a local region. The shimming process is especially important at high fields, both for reducing blurring and geometric distortions.

The spin echo sequence is less prone to image blurring since static B_o field inhomogeneities are refocused. Thus, the point spread function is narrower for spin echo than gradient echo images by a factor of $\sqrt{3}$.

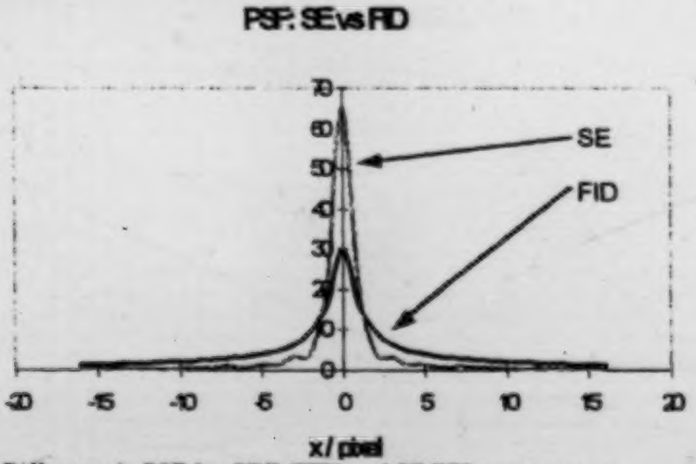

Figure 4.3.15: Difference in PSF for GRE (FID) and SE EPI sequences.

---

[3] The spatial resolution of an imaging system is the smallest separation of two point sources that remain resolvable in the image. The resolution limit of an imaging system is described by FWHM of its point spread function.

4.4 EPI acquisition parameters at 4.7T

As was shown in section 4.3, some of the major sources of artifacts in EPI are geometric distortions and signal dropouts which become even more problematic at high fields. For reasonable image quality, it is necessary to minimize these artifacts as much as possible. This section will discuss some of the most important echo planar imaging acquisition parameters and their optimization at 4.7T.

4.4.1 Acquisition time

T_2^* decay is much shorter at high fields. At 4.7T, for instance, T_2^* decay ranges from 20-30ms. In addition to blurring, longer acquisition time results in image distortions as the gradient offset builds up strength to disperse spin phases. For reasonable echo planar image quality, it is absolutely necessary to scan as fast as possible, i.e. reduce the echo train length. Faster acquisition may be accomplished by increasing the sampling bandwidth, using Partial Fourier methods, limiting spatial resolution or increasing the number of shots. Since this thesis deals with single-shot EPI, the multi-shot option was not explored.

Sampling rate (BW)

Sampling rate or bandwidth refers to how fast k-space is traversed in the readout direction. It can also be understood as the frequency difference from one pixel to another, determined by the time that elapses between collection of adjacent points. Bandwidth is a very important parameter for image quality: it determines the amount of blurring, distortions and chemical shift in the final image. Sampling on our system is non-uniform-time-sampling which means that the signal is sampled at equal 'k' increments: $\Delta k_x = \gamma \int G_x(t)dt = constant$. In other words, the area under the gradient is kept constant. Non-uniform time-sampling (also known as ramp-sampling), results in a uniform k-space Cartesian grid which is necessary for Fourier reconstruction. Ramp-sampling is achieved by scaling the gradient amplitude for the specified FOV while keeping the number of samples N the same as with a constant gradient. This can be clearly grasped by noting that $FOV_x = N_x \Delta x = 1/k_x = BW/\gamma G_x$ where FOV and BW are specified by the operator.

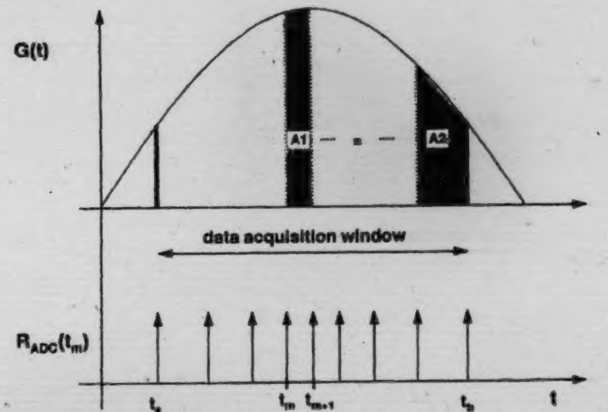

Figure 4.4.1: Non-uniform time-sampling. Note that the area under the gradient curve between two adjacent time points is kept constant.

Non-uniform time-sampling is superior to uniform time-sampling since there is no need for interpolation[4] to Cartesian k-space and consequently the acquisition of additional points. The following tables summarize the total acquisition time, gradient strength and rise time with different BWs for a FOV of 25.6cm.

Table 4.4.1: 4x4mm resolution.

BW	Total time (ms)	No. pts/ramp	No. pts/flat	Gradient	Rise time(µs)
200	30.6	16	32	1.83	157
300	**28.9**	31	2	2.59	222
400	Not achievable with the current FOV				

Table 4.4.2: 2x4mm resolution.

BW	Total time (ms)	No. pts/ramp	No. pts/flat	Gradient	Rise time(µs)
200	38.4	15	98	1.83	157
300	**32.0**	35	58	2.74	235
400	Not achievable with the current FOV				

Note from the second column in Table 4.4.1 and Table 4.4.2 that a significant number of data points are acquired during gradient ramp times. The following table demonstrates that ramp-sampling is essential for minimizing acquisition time:

Table 4.4.3: EPI acquisition time per data point with and without ramp-sampling.

BW	Ramp-samp	Readout time/pts (ms)	Rise time (µs)	Gradient (G/cm)
200	No	0.69	222	2.74
300	Yes	**0.45**	222	2.59

---

[4] Interpolation is computationally intensive.

Note from Table 4.4.3 that for a 64x64 matrix, the readout time is 29ms and 44ms with and without ramp-sampling respectively. Ramp-sampling hence results in acceptable readout times relative to T_2* decay of 20-30msec at 4.7T.

Even though the highest sampling rate at 4.7T is 400 KHz, it is not feasible for the typical readout field of view used for human head (< 240mm). To demonstrate this, let's calculate the readout gradient amplitude for FOV of 240mm and BW of 400KHz: $G = BW/\gamma FOV = 400KHz/(42.58\,MHz/T * 240mm) = 3.9G/cm$. Since the highest available gradient amplitude at 4.7T is 3.5G/cm, a bandwidth of 400 KHz is not feasible, unless FOV is increased or the gradient system is upgraded.

Alternatively, the minimum FOV may be calculated for a maximum bandwidth of 400 KHz and maximum gradient strength of 3.5G/cm: $FOV = BW/\gamma G = 400KHz/(42.58MHz/T * 3.5G/cm) = 268mm$. This FOV is bigger than the typical human brain. At 4.7T in vivo studies, a sampling rate of 300 KHz results in the fastest acquisition time.

Signal to noise ratio

Higher bandwidth results in lower SNR. The following equation shows the relationship between SNR and common MRI acquisition parameters:

$$SNR \alpha \Delta x \Delta y \Delta z \sqrt{N_{shots} N_{avg} N_x N_y / BW}, \qquad \textbf{(53)}$$

where N_{shots} is the number of excitations, N_{avg} is the number of averages, N_x and N_y are the number of points acquired in the frequency and phase-encode directions, and Δx, Δy and Δz are voxel dimensions.

A lower SNR due to a higher BW may be explained by noting that higher sampling rate results in faster digitization of the signal. This translates to sampling higher frequency components including white noise[5] which has a constant intensity at all frequencies. At high magnetic fields, SNR is not an issue since it linearly increases with B_o (signal intensity increases with B_o^2 whereas noise increases with B_o). In fact, higher available SNR is the main reason that very high resolution images, i.e. smaller voxel dimensions, are possible at high magnetic fields.

Resolution

As discussed before, the acquisition time has to be shorter than T_2* decay of the signal which limits the length of the echo train. In single-shot EPI, low resolution images of 64x64 and 128x64 pixels are typical considering the available maximum gradient strength and sampling speed. A system's hardware capabilities as a consequence play a key role.

---

[5] Noise in imaging systems arises from thermal motion (Brownian motion) of free electrons inside electrical components and human body, with human body noise dominating.

Partial Fourier Reconstruction/Acquisition

The number of acquired phase-encode lines may be reduced to shorten the acquisition time. This may be accomplished by Partial Fourier methods which refer to the acquisition of asymmetric k-space data. The shorter echo train reduces blurring and in some cases allows a desired echo time to be achieved.

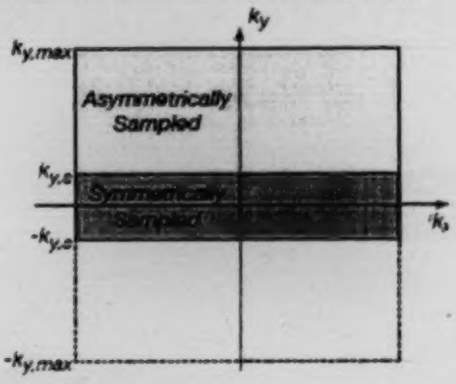

Figure 4.4.2: Partial-Fourier k-space Acquisition.

Partial Fourier data acquisition results in decreased SNR; however, at high fields SNR is not an issue and as such these methods are employed very frequently.

In theory, most MRI images are real-valued which means that only half of the k-space needs to be collected. The un-acquired lines may be synthesized by reflecting the data across the origin. This is due to conjugate symmetry[6] in the spatial frequency space:

$$S(k_x, k_y) = S^*(-k_x, -k_y). \tag{54}$$

In practice, there are many sources of phase error that violate the conjugate symmetry of real data. These phase errors are caused by variations in the resonance frequency, patient motion, etc. In this case, partial Fourier reconstruction requires the acquisition of more than half of k-space. There are many partial Fourier reconstruction methods. The simplest one is to zero-pad the uncollected k-space data prior to inverse Fourier transform.

---

[6] Also known as Hermitian symmetry

Zero-filling

Zero-filling works well if the collected k-space lines are equal to or greater than 75%. Going below this limit results in severe image blurring which is caused by multiplying the k-space data by an offset step function. The offset corresponds to the last acquired line:

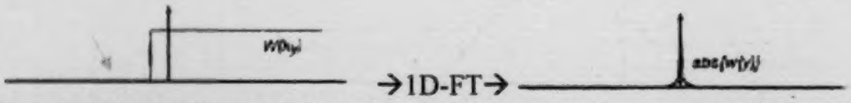
W(ky)
→1D-FT→
abs{w(y)}

Figure 4.4.3: Zero-filling partial Fourier reconstruction acts as a low-pass filter, causing blurring in the images.

This multiplication in k-space corresponds to convolution of the images with a low pass filter which smears out pixel intensities, causing blurring in the images. Other reconstruction methods such as homodyne may allow for a greater reduction in the acquired phase-encode lines (<75%). Homodyne was implemented and tested against zero-filling with EPI images; the results are presented in the following section.

Homodyne

The following diagram summarizes the homodyne reconstruction algorithm.

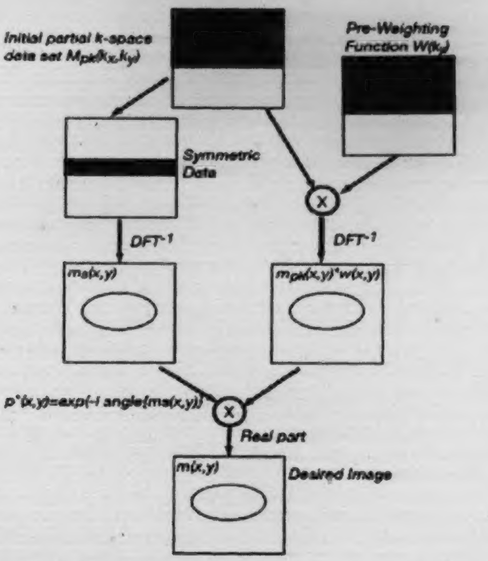
Initial partial k-space data set Mpk(kx,ky)
Pre-Weighting Function W(ky)
Symmetric Data
X
DFT-1
DFT-1
ms(x,y)
mpk(x,y)*w(x,y)
p*(x,y)=exp(-i angle(ms(x,y)))
X
Real part
m(x,y)
Desired Image

Figure 4.4.4: Homodyne Partial-Fourier Reconstruction.

In homodyne, the un-acquired data is zero-filled and the acquired k-space data is pre-weighted with a ramp function. The ramp function serves two purposes:

1. To minimize the sharp transition between the padded zeros and the measured data. Compare Figure 4.4.5 with Figure 4.4.3.
2. To offset the imbalance between the low and high frequency (k-space) data because of the lack of negative high-frequency data.

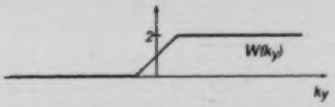

Figure 4.4.5: Ramp function.

A low resolution image is also synthesized from the symmetric k-space lines to extract phase information. The pre-weighted image is then phase-corrected and the final image is obtained by taking the real part of the result.

Homodyne and EPI

Homodyne partial Fourier reconstruction works well when the phase estimate is accurate. In practice, this means that the phase could be described using the low-frequency content. Figure 4.4.6 demonstrates the difference in homodyne and zero-filling partial-Fourier reconstruction for EPI images at 4.7T:

Figure 4.4.6: GRE-EPI images taken with TR/TE = 2000/25ms, 2x4x1.5mm resolution, 75% acquired lines and reconstructed with a) zero-filling and b) homodyne techniques.

The figure above shows that Homodyne Partial Fourier reconstruction results in severe signal voids in the anterior-inferior regions of brain. This is due to rapid phase variations in very inhomogeneous regions which are not accounted for by the low-frequency k-space data. Zero-filling actually results in better reconstruction as no phase corrections are performed.

4.4.2 B_o (in)homogeneity

Static field inhomogeneity is the main source of image artifacts in EPI, especially at higher fields where B_o is more inhomogeneous. Imaging at higher fields requires advanced hardware equipment e.g. higher gradient strengths; advanced shim methods and post-processing solutions (e.g. B_o field mapping (Jezzard [11]) and PSF mapping (Zaitsev [10]). Due to time-constraints, the focus of this thesis was directed at optimizing image acquisition parameters, shimming and basic post-processing methods.

Shimming

For echo planar imaging, it is important to have a 'good' shim in the desired imaging region. Shimming is accomplished by changing currents for a set of 'shim coils' which creates small magnetic fields in the imaging region, either enhancing or opposing the main magnetic field. The goal is to modify the applied current(s) such that the magnetic field in the imaging region becomes as homogenous as possible.

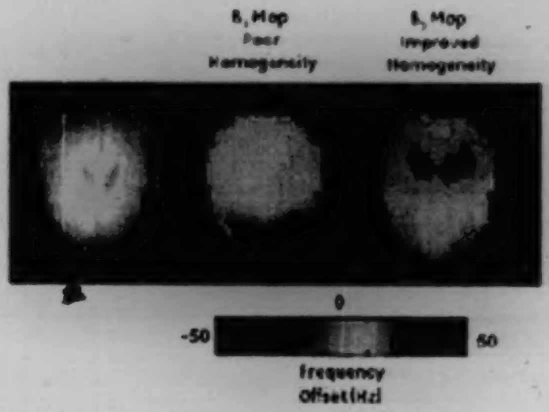

Figure 4.4.7: A demonstration of poor and acceptable shimming.

First-order shims are usually modified globally since they vary very slowly across the brain. Second-order shims on the other hand vary quickly and as a result, must be modified in a very local region. On our system, second order shims may be modified with PRESS pulse sequence where the slab of interest is confined to a local region.

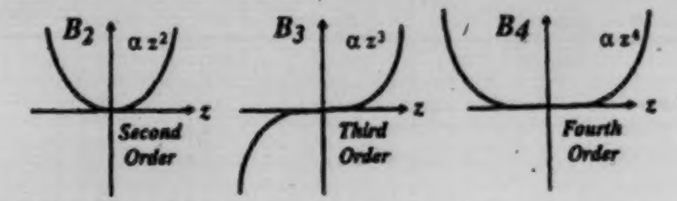

Figure 4.4.8: Higher order Shims.

The following figure is a snapshot of the Varian Inova 4.7T system manual shim window where the first and second-order shims may be modified for a longer FID decay and narrower water spectrum.

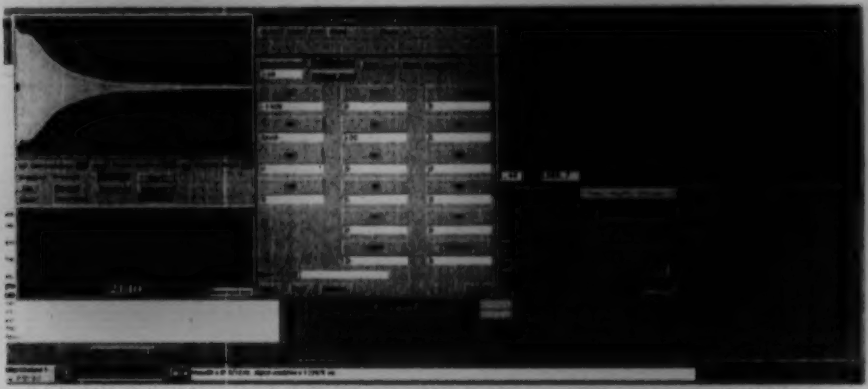

Figure 4.4.9: Window of manual shimming on Varian Inova 4.7T system. Left: FID signal, Right: power spectrum.

Higher shim order e.g. 3rd, 4th, etc. are extremely difficult to modify using manual shimming and need advanced 3D B_0 field mapping methods. On our system, the 3D shimming method has not been utilized due to difficulty in shim calibration. It has also been found that this method is unreliable and time-consuming which poses a significant problem when fMRI experiments are performed. Thus, first order and z^2 manual shimming has been the preferred choice.

Spectrum line shape and FID envelope decay

In order to evaluate the progress of a shim, it is important to look at the FID signal envelope or alternatively the power spectrum line shape. Two general rules apply:

1. Odd-order shims affect the line shape symmetrically whereas even-order shims cause an asymmetrical line shape.

2. The higher the shim order, the lower to the line base the defect is.

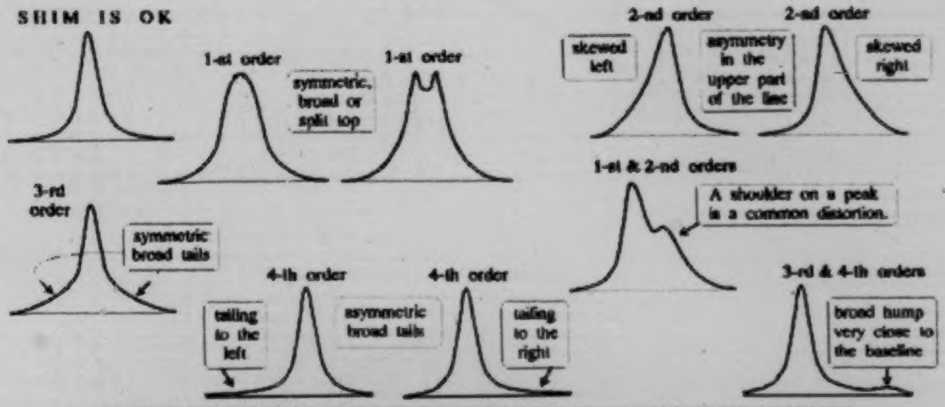
SHIM IS OK
1-st order
symmetric, broad or split top
1-st order
2-nd order
skewed left
asymmetry in the upper part of the line
2-nd order
skewed right
1-st & 2-nd orders
A shoulder on a peak is a common distortion.
3-rd order
symmetric broad tails
4-th order
tailing to the left
asymmetric broad tails
4-th order
tailing to the right
3-rd & 4-th orders
broad hump very close to the baseline

SKETCHES OF LINE DISTORTIONS CAUSED BY VARIOUS GRADIENTS

Figure 4.4.10: Common defects in line shape caused by mis-adjustment of shim currents.

The following figures demonstrate the changes in the FID envelope and the corresponding changes in line shape when shim currents are misadjusted. Note from Figure 4.4.11 that first order shims are better adjusted when focusing on the FID envelope while the line shape is an unambiguous tool when considering higher-order shims (Figure 4.4.12 and Figure 4.4.13).

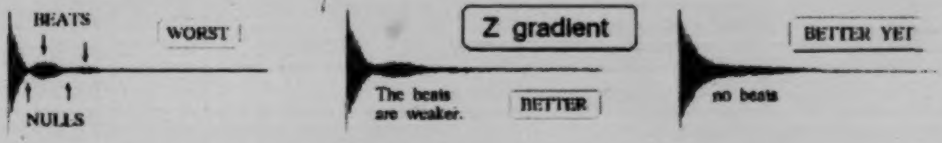

Figure 4.4.11: Adjusting first-order 'z' shim to eliminate beats and nulls in the FID signal.

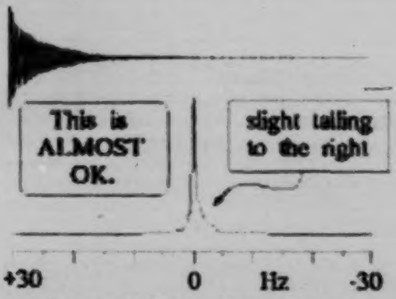

Figure 4.4.12: Adjusting second-order 'z' shim due to the asymmetrical skew of the line in addition to its existence close to the base of the line. The FID in this case decays faster in the first part of the envelope than the later parts.

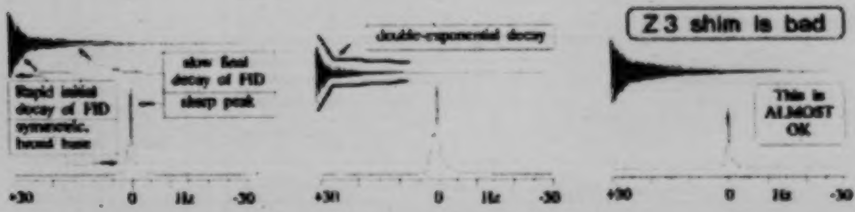

Figure 4.4.13: Adjusting third-order 'z' shim due to symmetric broadening at the base of the line shape. The FID envelope in this case is misleading as its faster initial decay can be categorized as a 'z2' or 'z4' shim.

When shimming, it is important to have a proper line shape in addition to a narrow line width (i.e. spectrum range) in order to set water resonance frequency accurately. At 4.7T, a line width of less than 20Hz (0.1ppm) indicates a proper line width over a slab of several millimeters.

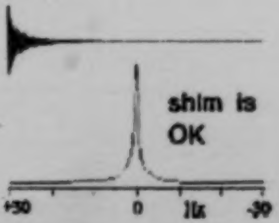

Figure 4.4.14: An example of a proper shim where the FID signal decays slowly, the line shape is symmetric and the bandwidth is below 20Hz.

Limited brain coverage

Shimming is not an issue at 1.5T but becomes a major limiting factor at high fields such as 4.7T. At high field strengths, there is a large variation in resonance frequency across the imaging region due to increasingly inhomogeneous magnetic field. In order to successfully shim, it is important to confine the imaging region for correct water frequency determination (ω_o). As a result, whole brain imaging with reasonable image quality at high fields becomes almost impossible.

Voxel Dimension

As was discussed in section 4.3, it is important to minimize image distortions and signal loss at areas where magnetic susceptibility difference is most severe. Even though smaller voxel dimensions in general result in lower SNR (Eqn. 53), they actually compensate for some signal loss by reducing intravoxel dephasing and limiting T_2^* range. This is clearly evident in auditory and nasal cavity regions in Figure 4.4.15 for 8mm and 2mm thick slices:

Figure 4.4.15: Conventional GRE images taken with two slice thicknesses at 4.7T with TR/TE: 50/25ms, α: 20°, a) 1x1x8mm b)1x1x2mm with 4 averages.

The minimum slice thickness using a 4ms Sinc r.f. pulse is 1.5mm on our system. Thinner slices may be achieved by increasing the r.f. pulse length.

Table 4.4.4: R.F. pulse lengths required for the listed slice thicknesses (considering a maximum slice-select gradient of 3.5G/cm).

R.F. pulse width (ms)	4.0	5.8	6.2	6.7	7.3	8.0
Min. thk achievable	1.5	1.4	1.3	1.2	1.1	1.0

Depending on the brain region, slice thicknesses of less than 2.0mm may be used at 4.7T. Due to T_2^* decay, matrix sizes of greater than 128x64 are not recommended with single-shot EPI unless parallel imaging techniques are employed.

Gradient Orientation

Due to the low bandwidth in the phase-encode direction (see example 1, section 4.3.2), it is important to consider the direction of phase-encode gradient. The following transverse images were obtained with left-right (L/R) and anterior-posterior (A/P) phase-encode gradients:

Figure 4.4.16: EPI images taken with 2x4x2mm resolution, a) A/P phase-encode and b) L/R phase-encode.

It is quite visible in the figure above that the L/R phase-encoded image is severely prone to image distortions and blurring. Table 4.4.5 also shows that the L/R phase-encoding results in higher intensity ghosts:

Table 4.4.5: Ghost intensity (%) for A/P and L/R phase-encodes.

L/R		A/P
Left (%)	Right (%)	Top (%)
20.1	14.5	5.0

The L/R phase-encoded images are more prone to artifacts since the phase variations in brain along this direction are more rapid. A/P phase-encoding therefore should be used to minimize EPI sensitivity to induced magnetic susceptibility variations at 4.7T.

Slice Orientation

For higher cognitive studies involving language areas of the brain, it is desirable to image the anterior-inferior regions of the brain. Due to the vicinity of these regions to large susceptibility gradients, it is important to consider the slice orientation in addition to phase-encode gradient direction. As was shown in Figure 4.3.9, oblique slices may be used to avoid problematic areas as much as possible.

Implementation

The original echo planar imaging sequence on the 4.7T console did not allow for oblique slices with phase-encode in the A/P direction. This was a set-back since oblique slices with phase-encode in the L/R direction result in severe ghosting and image distortions. To understand why this is the case, consider a transverse oblique slice in 'y' and 'z' directions. The readout gradient in this case has both a 'y' and 'z' component whereas the phase-encode gradient is in the 'x' direction. The two readout gradients are difficult to balance, causing severe timing differences between odd and even lines.

In order to get reasonable image quality, it was essential to implement oblique slices in the transverse90 orientation where the directions of the phase and readout gradients are swapped. For the example above, the readout gradient is now in the 'x' direction and the phase-encode gradient has a 'y' and 'z' components. The readout gradient behaves as in the non-oblique case and no additional adjustments are needed prior to acquisition.

Fat suppression

The lower bandwidth in the phase-encode direction results in pixel displacements caused by off-resonance effects such as chemical shifting. As was shown in example 2 in section 4.3.4, fat suppression in EPI is absolutely necessary.

In the current implementation of EPI on our system, fat suppression is achieved by applying a 90° saturation pulse simultaneously with spoiling gradients to dephase the lipid signal. To achieve reliable fat suppression, the frequency of the saturation r.f. pulse must match the resonance frequency of fat. An inhomogeneous magnetic field shifts the resonance frequencies of water and fat (fat and water differ by 3.5ppm in Larmor frequency in a homogenous field). As a result, the r.f. pulse may not center on the fat resonance frequency, resulting in incomplete fat suppression. It becomes extremely important to reduce the FOV as much as possible and shim locally on the region of interest to obtain reliable fat suppression.

4.4.3 B_1 (In)homogeneity

In addition to a uniform static B_o field, a homogeneous B_1 field is also desired for uniform transmission and reception (T/R). At low magnetic fields (< 4T), the RF wavelength is much larger than the human head (Refer to Table 4.4.6). The RF electromagnetic field (i.e. near-field regime) behaves as a standing wave (rather than a traveling wave) and the wavelength of the MR signal has no effect on coil operation.

Table 4.4.6: RF wavelength as a function of static magnetic field for invivo brain [3].

B_o(T)	λ_{RF} (m)
1.5	0.44
3.0	0.27
4.7	0.19
7.0	0.13
9.4	0.10
11.5	0.086

At high fields, the RF wavelength (e.g. $\lambda_{RF,4.7T}$:190mm) is much smaller than the human head (180-240mm). The RF electrodynamics (i.e. wave regime) as a result becomes more complex due to the onset of wave propagation (i.e. diffraction, interference and reflection) within the human head, resulting in a more inhomogeneous RF field. Vaughn et. al. (2001) for instance showed that the RF field is twice as inhomogeneous at 7T as 4T.

Variations in B_1 with position during transmission mode leads to variable flip angles across the imaging region. The T/R properties of an RF coil are linked by the reciprocity relationship. A coil that is well designed for transmission is also suitable for signal reception. As a result, separate analysis is not required in these two cases. The following figure shows a profile of the B_1 field for a transverse slice located at iso-center at 4.7T. Note that the B_1 field is strongest in the center of the slice and falls off at the brain peripheries.

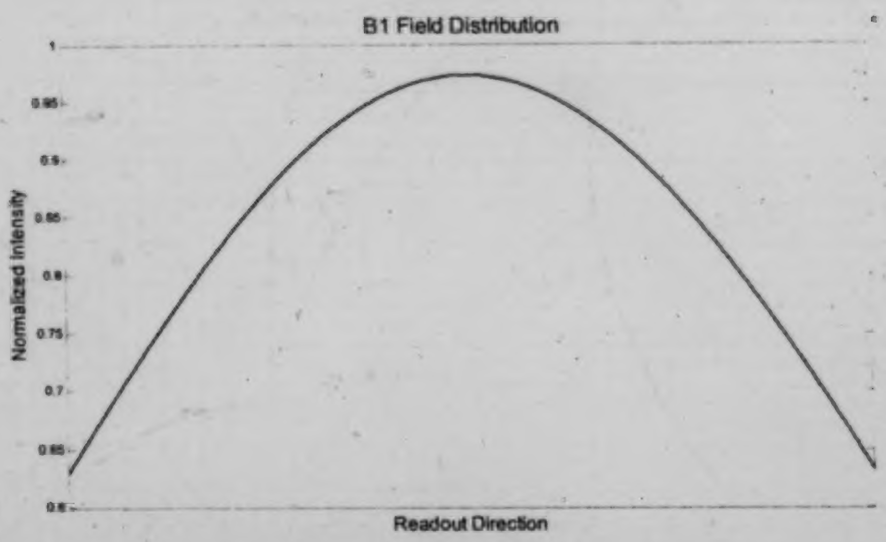

Figure 4.4.17: Fitted B$_1$ distribution for a transverse slice.

The flip angle distribution may be calculated directly by utilizing the B$_1$ field map above:

$$B_1 = B_1 \sin(\gamma B_1 \tau) = B_1 \sin\theta, \qquad \textbf{(55)}$$

where the flip angle θ is the area under the RF pulse (refer to section 2.2.2). The following figure shows the flip angle distribution for the transverse slice above:

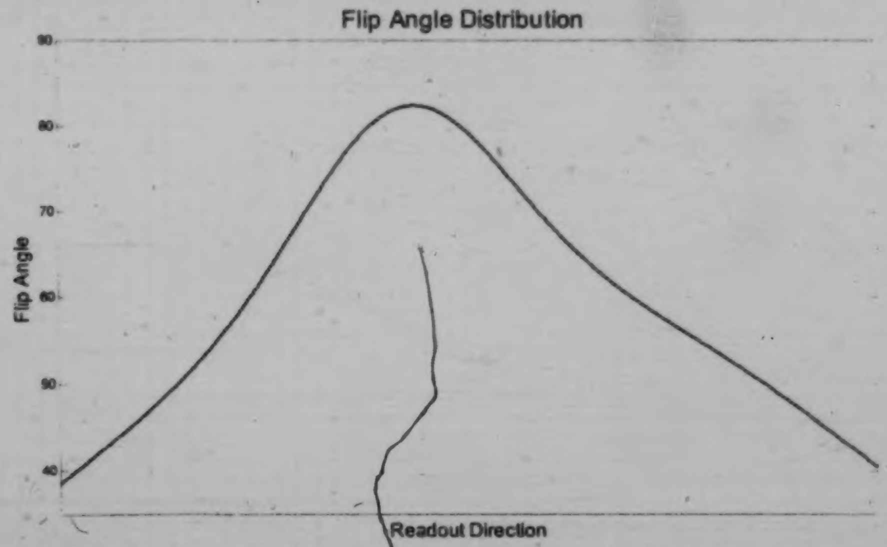

Figure 4.4.18: Fitted flip angle distribution for a transverse slice, calculated from B$_1$ map in Figure 4.4.17.

As seen from Figure 4.4.18, the center of the brain experiences the maximum flip angle. The signal intensity profile in GRE images may also be calculated for the above slice using the following equation:

$$S\alpha\theta \frac{(1-e^{-TR/T_1})}{(1-\cos\theta e^{-TR/T_1})}\sin\theta, \tag{56}$$

where θ is the flip angle, TR is the time of repetition and T_1 is the longitudinal relaxation for gray matter – 1.5sec at 4.7T. Figure 4.4.19 shows the signal intensity profile at 4.7T for the same slice using TR: 3sec. Note that signal intensity is highest at the center of the slice whereas it drops off at the peripheries of the brain. Signal variations in the slice are important factors to consider when making SNR measurements at high fields. Images therefore may be intensity-corrected.

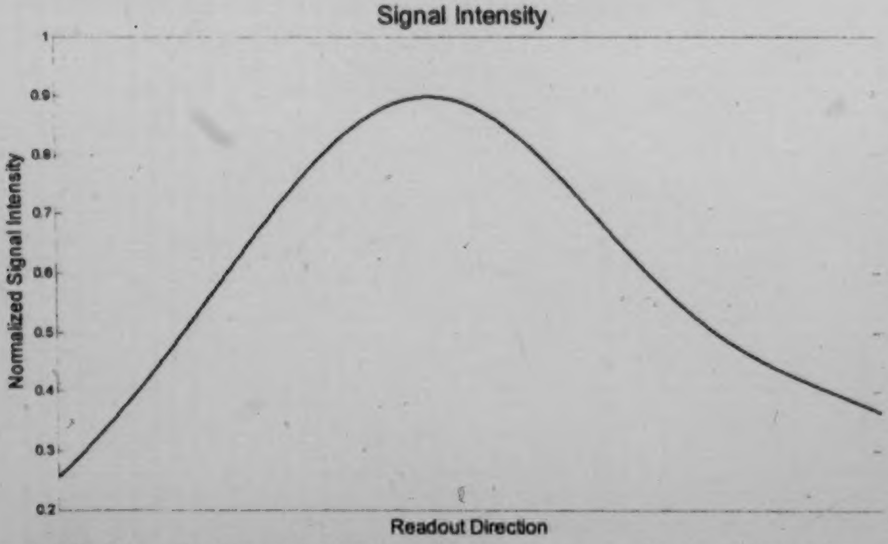

Figure 4.4.19: Normalized signal intensity profile for a transverse slices, calculated from flip angle distribution in Figure 4.4.18 and Eqn. 56.

RF power calibration

At 4.7T, the RF power was determined using readout projections of the center slice in the imaging region (no phase-encode gradient) using a conventional SE sequence. The RF power (dB) was incremented by 1 dB for 90° and 180° RF pulses[7] with a 4ms pulse duration. The RF power setting that resulted in the highest signal in the projection was chosen as the best average 90° flip angle, assuming a short TE (4ms) and a long TR (5 sec). As was observed in Figure 4.4.18, there is a strong spatial dependence of flip angle on RF power due to B_1 field inhomogeneity. Consequently, RF power may be set more accurately using B_1 field maps (Figure 4.4.17) to obtain 90° flip angles in a local region.

---

[7] The 180° RF pulse voltage was set twice as high as the excitation pulse.

Echo train adjustment using preparation reference scans

In EPI, any imperfection in the MR system (e.g. gradient offsets, improper shim) leads to misalignment of odd and even gradients. Thus, signal varies between the odd and even lines, causing Nyquist ghosts. The pattern of even and odd gradients can be reflected in a preparatory reference scan. As was shown in Figure 4.3.5, a reference scan is obtained by switching the phase-encode gradient off while keeping everything else as identical as in the imaging sequence.

In the ideal case, all even and odd echoes should be identical in the reference scan since no phase-encode gradient is involved. Differences however, do exist! A reference scan as a result provides significant information about the magnetic state of the imaging sequence and hence is an important part of EPI echo train adjustments. The following figure shows a balanced echo train on the Varian Inova 4.7T system where the positive and negative gradients are identical:

Figure 4.4.20: A balanced echo train.

The echo train may be balanced by 'tweaking' two main parameters:

1. In the presence of a constant gradient offset, the echoes increasingly drift to the right (or left) of the acquisition window. To balance the echo train, an additional gradient field is added to the readout refocusing gradient to cancel the gradient offset. Figure 4.3.12 shows a case where a gradient offset leads to an overall image shift.

Figure 4.4.21: An echo train drift to the right due to a negative background gradient offset. An additional positive gradient field may be applied to the readout refocusing gradient to null the gradient offset.

2. Large shifts between odd and even gradients which cause ghosting may be adjusted by adding an initial delay to the readout train to force the echoes to refocus at the center of k-space. Figure 4.3.4 shows an instance where an uncorrected shift between odd and even echoes cause fringes in the image.

Figure 4.4.22: Large echo shifts between even and odd lines. A delay (μs) may be added initially to ensure echoes are refocused at the center of k-space.

4.5 EPI Image Reconstruction with a Reference Scan

No matter how well the echo train is adjusted using preparatory reference scans, system variations during the actual imaging scan cause changes in the echo train state. As a result, reference scans acquired *immediately* before the imaging scan may be used in post-processing reconstruction to further reduce EPI artifacts. The following section discusses two reconstruction methods for reducing ghosting artifacts. The implemented Matlab code is included in appendix A.

4.5.1 Method 1: Linear Phase Correction

Echo shift

The following figure shows a sample echo position map, extracted from a subject's reference scan for 64 phase-encode lines (shown for 32 phase-encode lines):

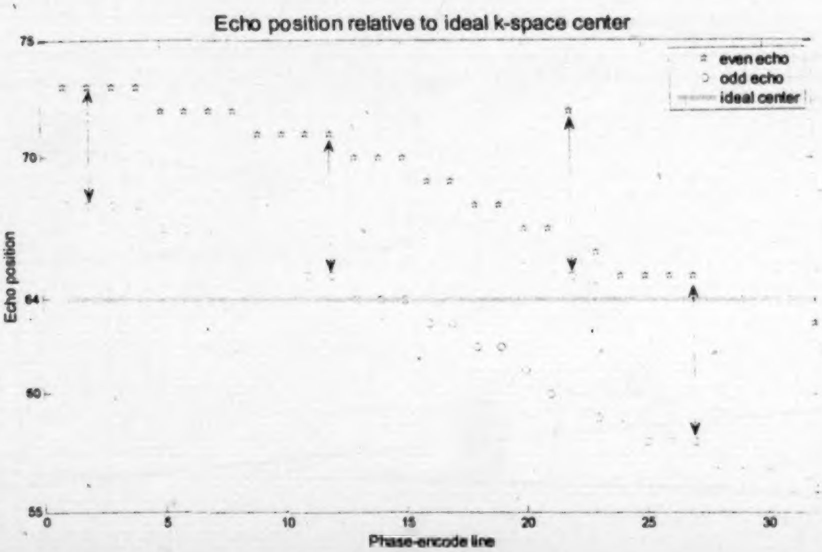

Figure 4.5.1: Echo position per k-space line acquired from a subject's reference scan (128x64 resolution). The scattered dots represent the 'actual' echo position for each k-space line whereas the solid line represents the ideal k-space position. The double arrows show the time delay (or k-space shift) between odd and even echoes.

Figure 4.5.1 shows that odd and even echoes shift linearly to the end of the readout window as more phase-encode lines are acquired. This linear shift is due to the presence of a constant background gradient offset e.g. misadjusted shim (as discussed in section 4.3.3) and causes an overall image shift. Also note from the same figure that there exists a constant shift between odd and even echoes. The source of this time delay may be eddy currents which cause Nyquist ghosts in images.

Constant Phase

In addition to echo shift, there also exists a constant phase per k-space line. Figure 4.5.2 shows a sample phase map for 64 k-space lines, extracted from a subject's reference scan. The phase for each k-space line is calculated from the echo peak as $phase = \tan^{-1}(\mathrm{Im}(S(k))/\mathrm{Re}(S(k)))$. Note from the figure that constant phase increases linearly for even and odd echoes.

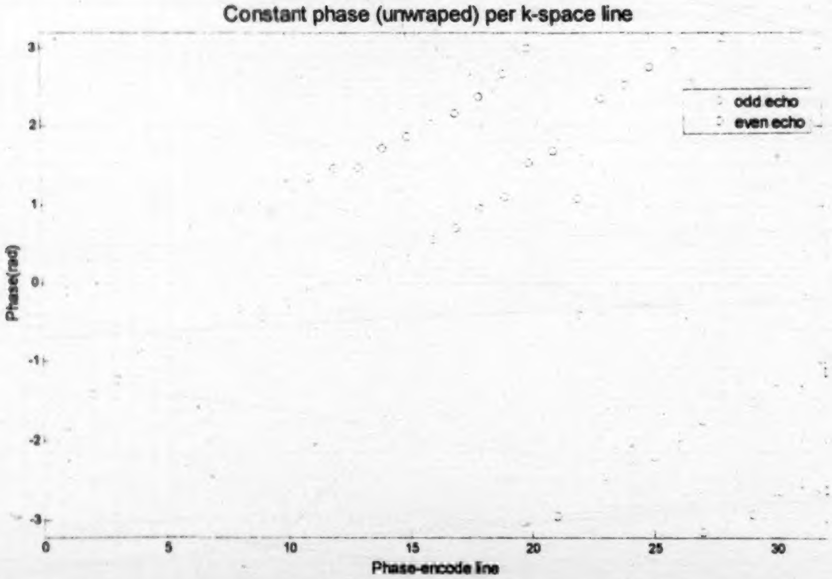

Figure 4.5.2: Constant phase per k-space line acquired from a subject's reference scan. The abrupt change in phase (π to $-\pi$) is due to the cyclic nature of phase, and not due to phase discontinuity.

In order to minimize ghosting artifacts, both linear and constant phase modulations must be corrected.

Figure 4.5.3: An axial slice showing the presence of dark bands and iso-intense ghosts when no phase-corrections are done.

Complications

The corrections based on the reference scan sometimes result in more ghosting when the echo center in the reference scan differs from the actual image data. This may be due to patient motion or clipping of the echo peaks by the A/D converter[8]. There may also exist nonlinear phase variations in the EPI data. In that case, a nonlinear phase correction might be more suitable.

---

[8] Data clipping occurs when the received signal is larger than what the A/D converter can handle.

Matlab implementation

From a reference scan corresponding to a slice, echo position k and phase θ_o is extracted for each phase-encode echo peak. The echo with the highest signal is used as the reference position and the relative echo shifts 'k_o' are calculated. Echo shift and constant phase is translated as linear phase modulation[9] in the half domain (phase-encode projections):

$$S(k-k_o)e^{i\theta_o} \rightarrow FT \rightarrow S(x,y)e^{i2\pi k_o x}e^{i\theta_o}, \qquad \textbf{(57)}$$

Phase correction is done by inverting the sign of the phases. The phase-correction filter F is,

$$F(x) = e^{-i2\pi k_o x}e^{-i\theta_o}, \qquad \textbf{(58)}$$

and the corrected data is,

$$S(x) = S'(x)F(x), \qquad \textbf{(59)}$$

where $S'(x)$ is the imperfect phase-encoded k-space data and $S(x)$ is the ideal phase-encoded k-space data.

4.5.2 Method 2: Nonlinear Phase Correction

In general, EPI reference scans show nonlinear phase modulations, especially in very inhomogeneous brain regions. In that case, nonlinear phase correction is more suitable.

Matlab implementation

The phase θ_o of each point in k-space is extracted from the phase-encode projections of the reference scan. The nonlinear phase correction filter $F(x) = e^{-i\theta_o(x)}$ compensates for nonlinear phase errors by simply inverting the sign of the phase. The correction is then made as $S(x) = S'(x)F(x)$.

---

[9] Fourier shifting theorem.

4.5.3 Comparison between the Linear and Nonlinear Phase Corrections

The following figures demonstrate the difference between linear and nonlinear phase correction methods. The image contrast and brightness are identical in both phantom images.

Figure 4.5.4: Nonlinear (left) and linear phase corrections (right).

The nonlinear phase correction method in general results in better image reconstruction apart from single pixel displacements across the image.

Figure 4.5.5: Nonlinear (left) and linear (right) phase-corrected EPI images.

For more information on linear and nonlinear phase-correction methods discussed here, the reader is directed to appendix A for the implemented Matlab code.

4.5.4 Reconstruction Summary

The following figure summarizes EPI reconstruction process as implemented in appendix A Matlab code.

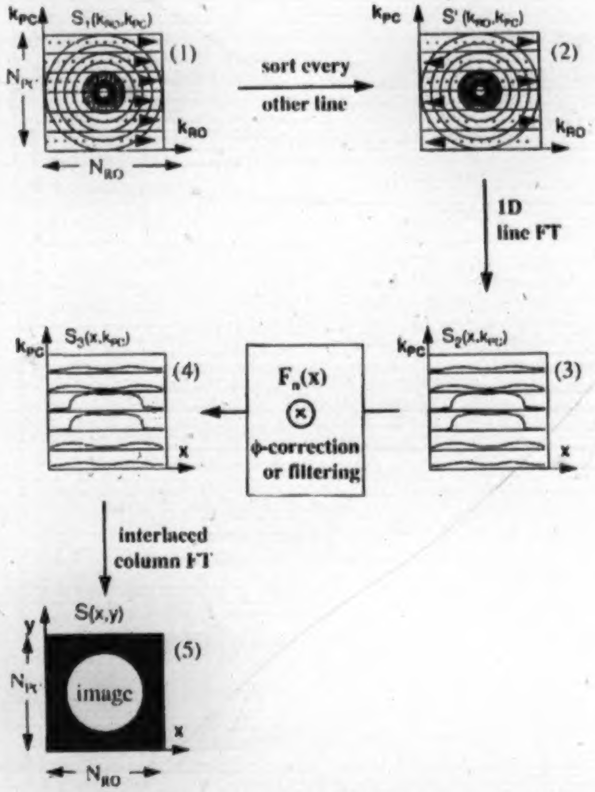
k_PC
S_1(k_RO,k_PC)
(1)
N_PC
k_RO
N_RO
sort every
other line
k_PC
S' (k_RO,k_PC)
(2)
k_RO
1D
line FT
k_PC
S_3(x,k_PC)
(4)
x
F_n(x)
⊗
ϕ-correction
or filtering
k_PC
S_2(x,k_PC)
(3)
x
interlaced
column FT
y
S(x,y)
(5)
N_PC
image
x
N_RO

Figure 4.5.6: EPI reconstruction method for uniform k-space data sampling.

As seen from Figure 4.5.6, alternate phase-encode lines are first reversed in time to account for negative polarity readout gradients. Next, the phase information is extracted from a reference scan and applied to the k-space data after Fourier transformation along the frequency-encode direction. The data is then Fourier transformed along the phase-encode direction to obtain the final image.

4.6 Conclusions

In this chapter, echo planar imaging and its variations were introduced. Since EPI k-space is acquired after one excitation with rapidly switching gradients, it suffers from severe phase variations which translate as Nyquist ghosts and geometric distortions in images. Various acquisition parameters were therefore optimized at 4.7T to obtain the best feasible image quality. Post-processing phase correction methods were also developed in Matlab to reduce ghosting artifacts and correct for image shifts.

References

1. D. C. Noll, D. G. Nishimura, A. Macovski, Homodyne detection in magnetic resonance imaging. *IEEE Transact. Biomed. Eng.* **10**, 154-163 (1991)

2. F. Schmitt, M. K. Stehling, R. Turner, Echo-Planar Imaging: Theory, Techniques and Application. Springer-Verlag Berlin, Germany (1998).

3. F. Wiesinger, P.-F. Van de Moortele, G. Adriany, N. De Zanche, K. Ugurbil, K. P. Pruessmann, Potential and feasibility of parallel MRI at high field. *NMR in Biomed.* **19**, 368-378 (2006).

4. G. A. Pearson, Shimming an NMR magnet, 1-16 (1997).

5. G. Johnson, J. M. S. Hutchinson, The limitations of NMR recalled echo imaging techniques. *J. Magn. Reson.* **63**, 14-30 (1985).

6. J. Pauly, Partial k-space Reconstruction online notes.

7. K. M. Koch, B_0 inhomogeneity: Causes, effects and measurements. *ISMRM Workshop on Advances in High Field MR* (2007).

8. M. K. Stehling, Echo planar proton magnetic resonance imaging. Ph.D Thesis, University of Nottingham, UK.

9. M. S. Cohen, R. M. Weisskoff, Ultra-fast imaging. *Magn. Reson. Imaging* **9**, 1-37 (1991).

10. M. Zaitsev, Software correction of B_0 distortions: What can be corrected in the post-processing? *ISMRM Workshop on Advances in High Field MR* (2007).

11. P. Jezzard, R. S. Balaban, Correction for geometric distortion in echo planar images from B_0 field variations. *Magn. Reson. Med.* **34**, 65-73 (1995).

12. P. Mansfield, Multi-planar image formations using NMR spin echoes. *J. Phys. C.* **10**, L55-58 (1977).

13. R. J. Ordidge, P. Mansfield, NMR methods. United States Patent 4509015

14. R. R. Edelman, P. A. Wielopolski, F. Schmitt, Echo-planar MR imaging. *Radiology* **192**, 600-612 (1994).

15. VnmrJ Imaging User Guide. Varian Inc. Palto Alto, CA (2005).

16. V. Kuperman, Magnetic Resonance Imaging Physical Principles and Applications. Academic Press San Diego, CA (2000).

10. Z-P. Liang, P. C. Lauterbur, Principles of Magnetic Resonance Imaging: A Signal Processing Perspective. IEEE Inc. New York, NY (2000)

5 FMRI Imaging and Analysis Methods

Due to the nature of the hemodynamic response function, functional MRI studies require high temporal and spatial resolution. It has been found that echo planar imaging is the preferable method over conventional imaging methods due to its fast acquisition capabilities among many other benefits discussed in the upcoming section.

In addition to reasonable image quality, echo planar imaging parameters need to be optimized for the fMRI study under investigation. The selection of echo time, repetition time and voxel dimension needs to be considered prior to a study to achieve the best feasible fMRI result. Other factor to consider is the selection of appropriate paradigms, in order to correctly identify the functional anatomy in response to stimulation. These factors are discussed thoroughly in the following sections.

For functional MRI data analysis, many software packages are available to the user. However, the most widespread package cited in literature is SPM. Thus, in this chapter, a general step by step outline is provided for the processing and analysis or fMRI data using SPM5. The procedure described here applies to any fMRI statistical software and may be replicated accordingly.

5.1 Imaging Technique

Echo planar imaging is the preferable imaging protocol for BOLD functional MRI. Aside from providing reasonable image quality (2-4mm in-plane resolution), EPI is intrinsically sensitive to field inhomogeneities and thus the BOLD signal. The BOLD signal change during brain activation is 1-2% at 1.5T and 2-6% at 4.7T[10]. This small signal change needs to be enhanced relative to noise to be detectable and hence it is usual practice in fMRI to acquire hundreds of brain volumes to average the BOLD signal. Since HRF lasts on the order of seconds, fMRI time-series has to also be obtained as fast as possible. EPI has the capability to collect a brain volume in 2-3 seconds which makes it an ideal tool for capturing the temporal characteristics of HRF. In addition, the shorter scan time helps to minimize subject's movement in the magnet. Most subjects can tolerate up to an hour in the magnet and longer scan times lead to large motion artifacts. Figure 5.1.1 shows a subject's movement behavior as the function of scan time.

---

[10] Refer to chapter 6.

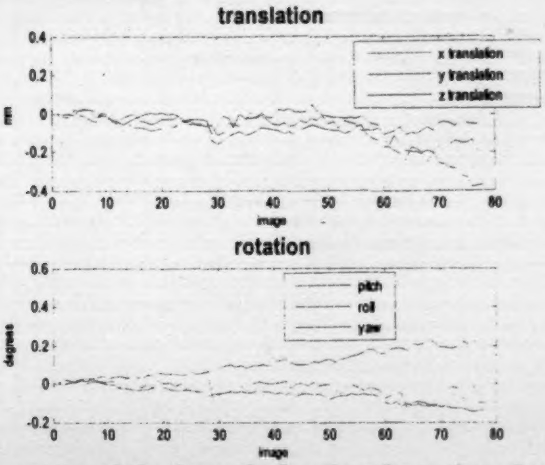

Figure 5.1.1: Subject movement behavior as the function of scan time, characterized in 3-D by translation (x,y,z) and rotation (pitch, roll, yaw).

EPI also has a higher SNR per unit time in comparison to conventional gradient-echo sequences since more brain volumes are captured in time. Another advantage of EPI is the use of long repetition times which eliminates the inflow of fresh blood into the imaging region.

As was discussed in chapter 4, echo planar imaging suffers from severe blurring, distortions and signal dropouts. However, the fast acquisition capability of EPI outweighs its disadvantages. In addition, recent hardware innovations and novel post-processing solutions are succeeding in improving EPI image quality.

5.2 Parameter optimization at 4.7T

In addition to image quality, EPI acquisition parameters need to be optimized for maximal BOLD CNR. The following section highlights the most important fMRI imaging parameters and their optimization at 4.7T.

5.2.1 Echo time (TE)

Echo time in fMRI is chosen such that the signal difference between stimulus and control states is maximized. If TE is too short, the signal is insensitive to T_2*. If TE is too long, the MR signal decays away before it is measured, thus a severe reduction in SNR. Gati [1] showed that maximal BOLD contrast occurs at $TE = T_2^*$ (of either tissue or vessel). Figure 5.2.1 shows the BOLD signal change as a function of echo time at 1.5T and 4 T. The ideal T_2* and T_2 values are measured as 23 and 55ms at 4.7T [3].

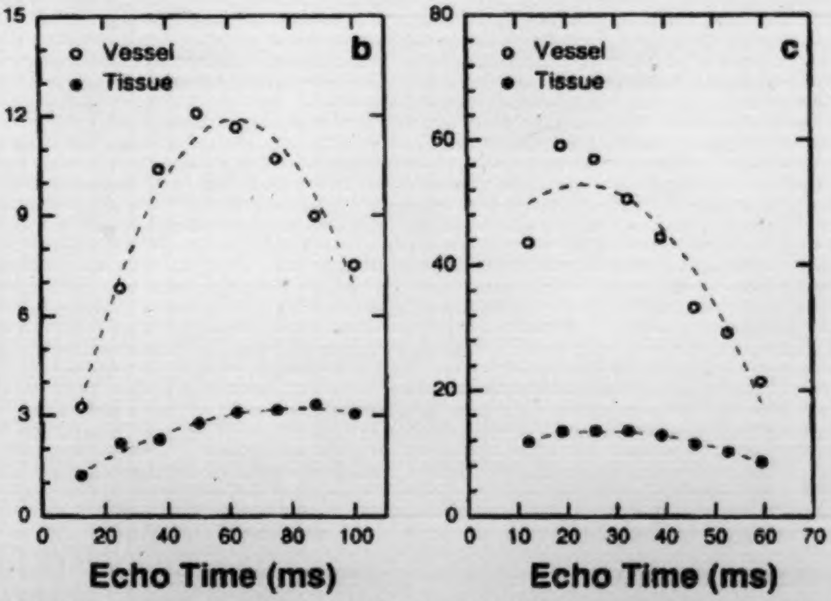

Figure 5.2.1: BOLD contrast as a function of echo time within vessel and tissue for b) 1.5T and c) 4T to illustrate that maximum contrast occurs at $TE=T_2$* in vessel and tissue regions [1].

The "ideal" echo time in practice is affected by the brain region under consideration. T_2* values change significantly in different brain regions due to magnetic susceptibility gradients and thus field inhomogeneity. Since these regions are often associated with poor shim, the echo time may have to be decreased to maximize the BOLD CNR (Eqn. 44). Brain regions such as the inferior frontal lobe and the temporal lobe are especially prone to signal losses and require the use of shorter TE to compensate for some of the SNR.

In summary, echo time selection in fMRI is a compromise between BOLD signal change and SNR. In chapter 6, fMRI scans are initially performed on one subject with multiple echo times. The echo time which results in the maximum BOLD CNR is chosen as the optimal TE.

5.2.2 Time of Repetition (TR)

At high fields, the longitudinal magnetization increases. To avoid signal saturation effects, longer TR has to be used which implies that fewer brain volumes are collected per unit time – thus a lower SNR per unit time. At 4.7T, a TR of 2 to 3sec is used to allow for the reasonable recovery of magnetization and to avoid blood inflow problems.

5.2.3 Voxel dimensions

In functional MRI, the voxel dimension has to match the size of the activation region. If the voxel size is too large, partial volume averaging effect takes place where the measured BOLD signal is diluted over a large region resulting in reduced BOLD signal change. At 4.7T, in-plane EPI resolutions of 2x2 mm and 4x2 mm are used along with slice thicknesses of 2mm and lower. As was discussed in chapter 4, in-plane resolution is limited by T_2* decay, and voxel dimension is chosen to limit signal loss in areas of large magnetic susceptibility differences.

5.3 Paradigm Design

The fMRI response is dependent on the brain stimulation method in addition to acquisition parameters. The method that was utilized in this thesis is block design[11] which is characterized by fixed periods of stimulus condition alternated with fixed periods of control condition. For instance, to study brain activation in the primary visual cortex (V1), a paradigm would consist of five 30sec blocks of a flashing checkerboard alternated with five 20sec blocks of a black screen (see Figure 5.3.1).

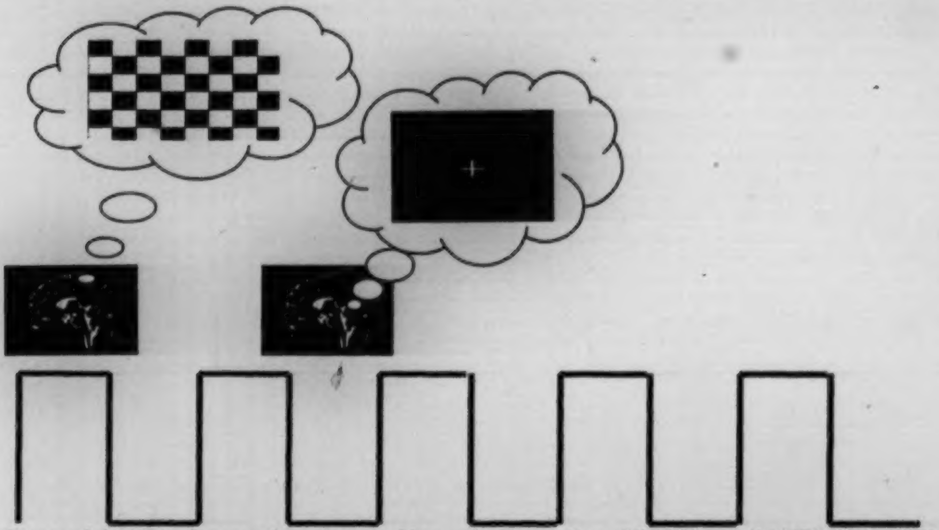

Figure 5.3.1: Block paradigm design. Shown is five cycles of "ON" and "OFF" period. The stimulus condition involves looking at a flashing checkerboard. The control condition involves fixating on a white dot in the middle of the screen.

Since BOLD signal change is relative, the control condition has to be chosen appropriately. The following rules apply: the control condition has to be repeated at a higher frequency than noise and it must involve only those mental processes that are engaged in the stimulus condition. When chosen appropriately, the latter rule ensures that the "desired" mental process is localized. The reader is directed to chapter 6 for sample fMRI paradigm designs.

---

[11] Also referred to as box-car design.

It is difficult to determine the block duration for an fMRI study. Most studies to date as well as those designed in chapter 6 have used 20 to 30sec blocks corresponding to relative HRF duration. It is important to keep in mind however that HRF varies in response to different types of tasks which may require different block durations (Figure 3.1.3).

The block design is typically used to detect activation in a region. Even-related fMRI – another stimulation method – is usually employed to study higher cognitive functions in brain. Since the purpose of this thesis was to evaluate fMRI performance at 4.7T, the event-related method was not employed. Instead, tried-and-true paradigms were evaluated. For more information, refer to chapter 6.

5.4 Data analysis

As discussed in chapter 3, the difference in signal intensity between the control and task states results in the BOLD signal. The most obvious method for identifying activated voxels is to subtract the average of the task images from the average of the control images. However, simple subtraction does not distinguish between actual activation and false activation caused by residual noise.

If the only noise source in the time-series was random thermal noise, it would be independent at different time points, with the same variance. In fMRI, the second noise source comes from physiological sources such as respiratory cycle, which is spatially and temporally correlated. The difference map for each voxel therefore needs to be normalized by the signal variance in that voxel to eliminate false activations caused by large signal fluctuations. The resulting SNR map is referred to as statistical parametric map (*SPM*).

5.4.1 SPM5 Statistical Software

For fMRI data analysis, there was no need to re-invent the wheel. There are several commercially available fMRI analysis software including SPM, FSL and Brain Voyager. In this thesis, SPM5 was used as the tool of choice due to its easy installation, readily available documentation in addition to its widespread use in fMRI research literature. The following section will briefly outline general procedures for fMRI data analysis.

Realignment

Since fMRI statistical analysis is done on a voxel by voxel basis, subject movement in the scanner (on the order of millimeters) results in large motion artifacts. If motion is correlated with stimulus presentation, it may be mistaken as real BOLD effect on the activation map[12]. Hence, the first preprocessing step in fMRI data analysis is realigning fMRI brain volumes.

In SPM5, six rigid body transformation parameters (3 translations, 3 rotations) are first estimated such that the mean square difference between each image and a reference image is minimized. The reference scan may either be the first image in the time-series or the calculated mean image.

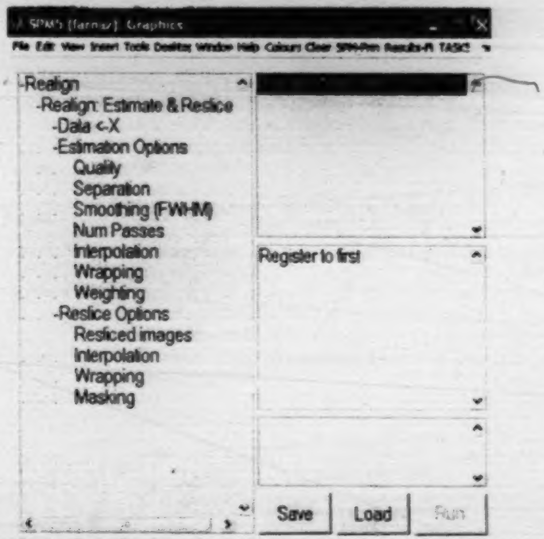
SPM5 (farnaz): Graphics
File Edit View Insert Tools Desktop Window Help Colours Clear SPM-Print Results-Fi TASKS
-Realign
-Realign: Estimate & Reslice
-Data <-X
-Estimation Options
Quality
Separation
Smoothing (FWHM)
Num Passes
Interpolation
Wrapping
Weighting
-Reslice Options
Resliced images
Interpolation
Wrapping
Masking
Save
Load
Run

Register to first

Figure 5.4.1: SPM5 snapshot of realignment procedure. In this case, the first volume in the time-series is chosen as the reference scan.

All the images in the time-series are realigned to the reference scan by applying the estimated transformation parameters. This is done by interpolation which may be either trilinear (nearest neighbor) or n^th^-order spline. The degree of interpolation depends on the desired accuracy and speed.

Smoothing

Smoothing is basically an averaging process where each new image value is a combination of its original value and those of its neighbors.

---

[12] Motion artifacts usually appear on the edges of the brain.

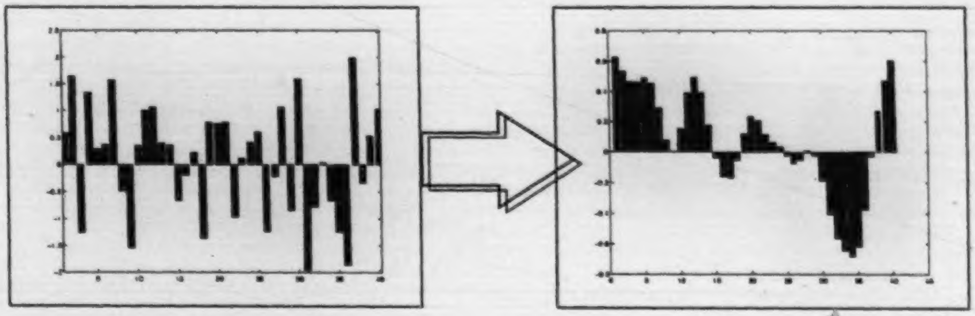

Figure 5.4.2: Smoothing process.

Smoothing is performed in SPM5 by convolving the fMRI images with a 3D Gaussian kernel of specified full-width at half maximum (*FWHM*). According to the matched filter theorem, the smoothing kernel has to be the size of the expected signal – in this case, the BOLD signal – to give the optimal SNR. As a rule of thumb, the kernel chosen is 2 to 3 times the voxel dimension. For a 4x4mm in-plane resolution for instance, an isotropic Gaussian kernel of 8mm may be used. If not sure, it is advisable to smooth with varying kernel sizes to find the best match.

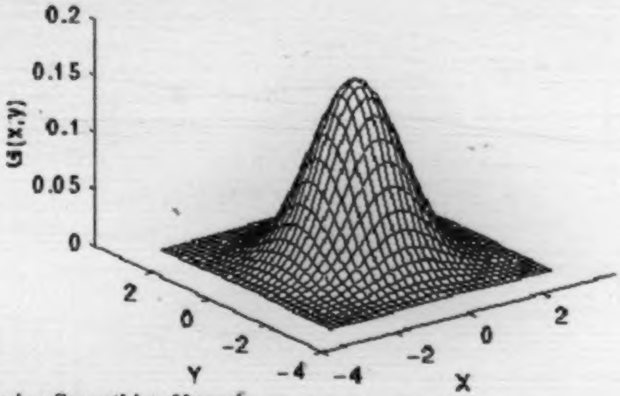

Figure 5.4.3: Gaussian Smoothing Kernel.

Smoothing is a necessary step in pre-processing since it increases the signal to noise ratio in the images – suppressing noise as a result. For multi-subject analysis, smoothing also reduces the functional and anatomical differences between subjects. Common activation regions may then be identified.

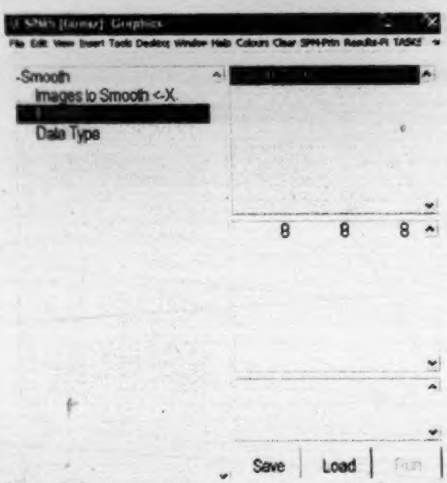
-Smooth
Images to Smooth <-X
Data Type
8 8 8
Save
Load
Run

Figure 5.4.4: SPM5 snapshot of the smoothing procedure. An 8mm isotropic Gaussian kernel is used for typical EPI voxel dimensions at 4.7T.

Statistical Analysis

Design Matrix

Statistical analysis of fMRI data is based on the general linear model (*GLM*). The estimation compromises of fitting a linear combination of one or more models[13] (plus noise) to the observed fMRI data on a voxel by voxel basis. As an initial step, a design matrix is appropriately chosen based on the stimulation paradigm. In the block design case, this would involve specifying TR, onset times of the task blocks and their duration.

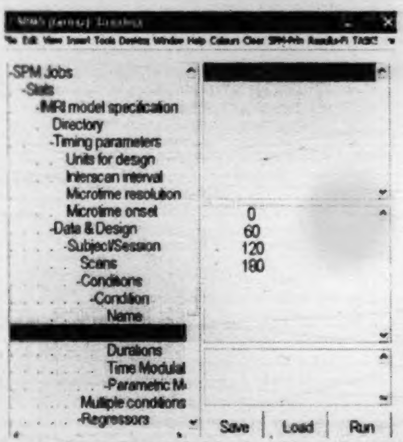
-SPM Jobs
-Stats
-fMRI model specification
Directory
-Timing parameters
Units for design
Interscan interval
Microtime resolution
Microtime onset
-Data & Design
-Subject/Session
Scans
-Conditions
-Condition
Name
Durations
Time Modulat
-Parametric M
Multiple conditions
-Regressors
0
60
120
180
Save
Load
Run

Figure 5.4.5: Specifying the onset times for task blocks. Note that this may be done in seconds or scan number. In this figure, the onset times are 0, 60, 120 and 180 seconds.

---

[13] The models themselves need not be linear.

The design matrix also includes high-pass and low-pass filters. The data is high-pass filtered to remove low-frequency drifts in the signal, such as the cardiac and respiratory cycles. It is important to set the filter periodicity appropriately to the experimental design in order to not remove the signal of interest. The width of the high-pass filter is chosen as two times the duration of a block cycle. For a 60sec block cycle for instance, a 120sec filter may be used.

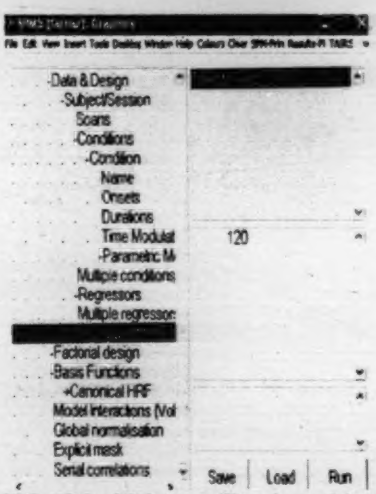
File Edit View Insert Tools Desktop Window Help Colours Clear SPM-Print Results-Fi TABS
-Data & Design
-Subject/Session
Scans
-Conditions
-Condition
Name
Onsets
Durations
Time Modulat
-Parametric M
Multiple conditions
-Regressors
Multiple regressor
-Factorial design
-Basis Functions
+Canonical HRF
Model Interactions (Vol
Global normalisation
Explicit mask
Serial correlations
Save
Load
Run

120

Figure 5.4.6: Specifying the width of the high-pass filter kernel in seconds.

The data is also convolved with the hemodynamic response function (SPM canonical HRF) to account for its sluggish behavior (i.e. shape and latency) as well as to remove high-frequency noise. In summary, the design matrix is "where the experimental knowledge about the expected [BOLD signal] is quantified" [4].

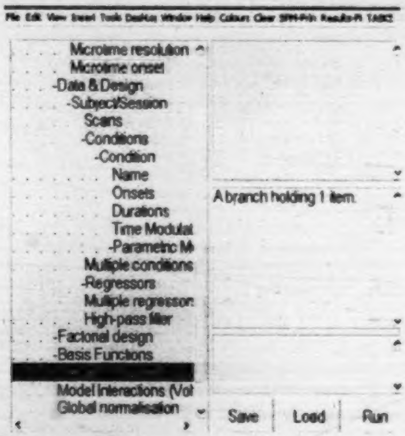
File Edit View Insert Tools Desktop Window Help Colours Clear SPM-Print Results-Fi TABS
Microtime resolution
Microtime onset
-Data & Design
-Subject/Session
Scans
-Conditions
-Condition
Name
Onsets
Durations
Time Modulat
-Parametric M
Multiple conditions
-Regressors
Multiple regressor
High-pass filter
-Factorial design
-Basis Functions
Model Interactions (Vol
Global normalisation
Save
Load
Run

A branch holding 1 item.

Figure 5.4.7: Specifying the low-pass filter.

Parameters Estimation

After the design matrix is constructed, the GLM is used to estimate parameters that best fit the design matrix to the observed time-series data. This is mathematically represented by the linear regression equation:

$$\vec{Y} = \vec{X}\beta + \vec{\varepsilon}, \qquad \textbf{(60)}$$

where $\overline{Y}$ is the observed fMRI time-series, $\overline{X}$ is the design matrix and β is the estimated parameters that fit the specified model ($\overline{X}$) to the observed data ($\overline{Y}$). The error term ε is the residual difference between the observed data and fitted model:

$$\vec{\varepsilon} = \vec{Y} - \vec{X}\beta. \qquad \textbf{(61)}$$

The fitted parameters β are determined by minimizing the least sum of squares between the observed data and specified model i.e. minimizing ε :

$$\beta = (\overline{X}^T \overline{X})^{-1} \overline{X}^T \overline{Y} \qquad \textbf{(62)}$$

As seen from Eqn. 60-62, it is important to specify the design model as accurately as possible to minimize ε .

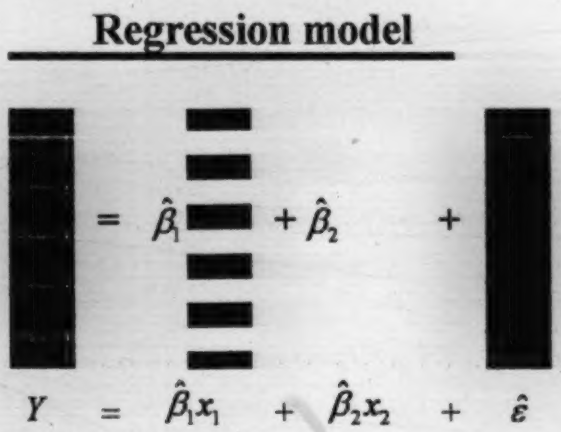
Regression model
=
$\hat{\beta}_1$
+ $\hat{\beta}_2$
+
$Y = \hat{\beta}_1 x_1 + \hat{\beta}_2 x_2 + \hat{\varepsilon}$

Figure 5.4.8: General Linear Model.

Figure 5.4.9 shows a SPM5 design matrix corresponding to four 30sec blocks alternated with four 20sec blocks. Gray and white blocks represent the control and task conditions respectively.

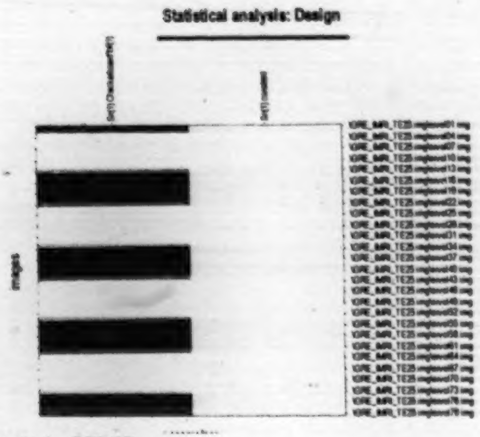

Figure 5.4.9: Design Matrix in SPM5.

Statistical Significance

As discussed in the introduction, a simple subtraction method does not distinguish between actual activation and false activation caused by large signal variations. Thus, to quantify the quality of the measured activation (i.e. test the null hypothesis), t-statistics may be calculated for each voxel using Eqn. 63:

$$t = t - stat = {}^{\beta\overline{X}\sqrt{N-1}}\!\big/_{\varepsilon}\,, \qquad \textbf{(63)}$$

where ${}^{\varepsilon}\!\big/_{\sqrt{N-1}}$ is the standard deviation of noise, N is the number of scans and (N-1) is the degrees of freedom in the error space. The resulting statistical map is referred to as an SPM map (spmT_0001 file in SPM5). As seen from Eqn. 63, the t-statistic is a measure of how large the difference between the task and control conditions is as compared to the variability of noise in a voxel (SNR map). As t gets larger, the probability that activation comes from large noise variations becomes less and less likely. Thus, the statistical significance reflects the *confidence* with which the null hypothesis (i.e. no activation) is rejected.

The test of significance may be followed by a selecting a probability threshold, e.g. $p < 0.05$ which corresponds to a certain t-value. Consequently, voxels whose t-values pass the threshold are picked out and displayed in color (statistical activation map).

Final Results

Following model estimation and statistical threshold, SPM5 overlays the statistical activation map upon a glass brain for quick visualization. In addition, a table of statistically significant clusters along with their spatial coordinates is provided. It is important to note that for multi-subject comparison or for identifying Brodmann areas, the activation maps need to be in MNI space. In that case, the realigned volumes may be normalized to an SPM5 common template prior to smoothing. The resulting activation map is then in MNI coordinates which may then be converted to Talaraich & Tourneau coordinates in Matlab (The MathWorks Inc.) using mni2tal script (available online). Subsequently, Talaraich Daeomon Client [8] may be used to identify Brodmann areas associated with the coordinates provided.

SPM5 also provides fMRI time-course plots, which shows the BOLD signal change as a function of scan time. Alternatively, MARSBAR toolbox may be used to quantify the BOLD signal change in a desired region of interest (ROI). For more information, refer to [2, 6], [7] and chapter 6.

5.4.2 Summary

The following figure summarizes the processing and analysis procedures described in this chapter:

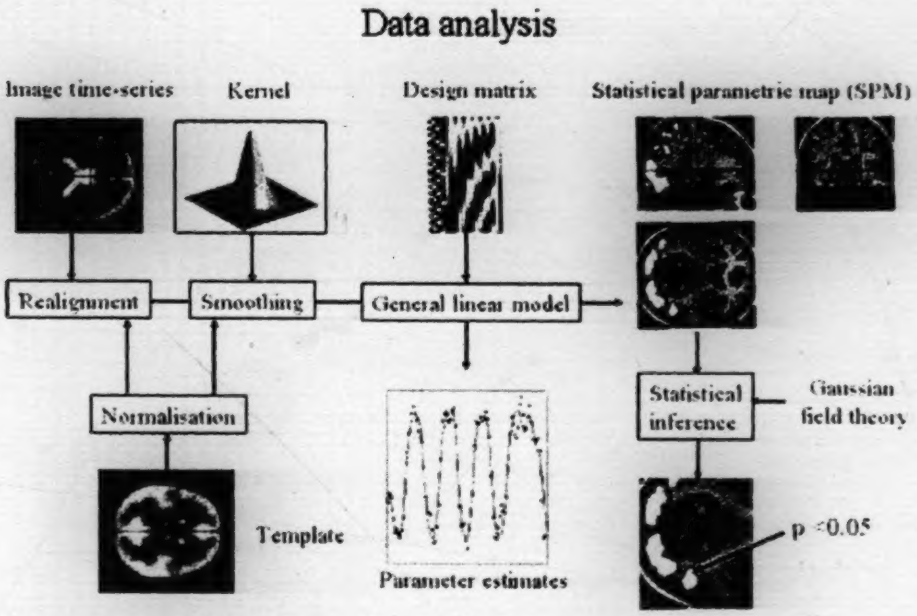
Data analysis
Image time-series
Kernel
Design matrix
Statistical parametric map (SPM)
Realignment
Smoothing
General linear model
Normalisation
Template
Parameter estimates
Statistical inference
Gaussian field theory
p <0.05

Figure 5.4.10: Summary of fMRI data processing and analysis.

5.5 Conclusions

In this chapter, the reader was introduced to the general data acquisition and analysis methods used in fMRI. Echo planar imaging has become the imaging sequence of choice as it offers high temporal resolution combined with reasonable image quality. The data analysis steps outlined in SPM5 are applicable to other fMRI statistical software and may be replicated accordingly. Realignment, normalization and smoothing are followed by model estimation, and statistical threshold to identify all statistically active voxels.

References

1. J. S. Gati., R. S. Menon, K. Ugurbil, K. Rutt, Experimental determination of the BOLD field strength dependence in vessels and tissue. *Magn. Reson. Med.* **38**, 296-302 (1997).

2. M. Brett, J-L. Anton, R. Valabregue, J-B. Poline, Region of interest analysis using an SPM toolbox. *NeuroImage* **16**, Supplement 1, 769-1198 (2002).

3. M. J. Silvennoinen, C. S. Clingman, X. Golay, R. A. Kauppinen, P. C. M. van Zijl, Comparison of the dependence of blood R2 and R2* on oxygen saturation at 1.5 and 4.7 Tesla. *Magn. Reson. Med.* **49**, 47-60 (2003).

4. R. B. Buxton. Introduction to Functional Magnetic Resonance Imaging Principles and Techniques, Cambridge University Press USA (2002).

5. R. S. J. Frackowiak, K. J. Friston, C. Frith, R. Dolan, C. J. Price, S. Zeki, J. Ashburner, W. D. Penny. Human Brain Function, 2nd edition. Academic Press San Diego (2003).

6. MARSBAR, http://marsbar.sourceforge.net.

7. SPM5 Manual, http://www.fil.ion.ucl.ac.uk/spm/doc/manual.pdf.

8. Talaraich Daemon Client, ric.uthscsa.edu/projects/talairachdaemon.html.

6 Evaluation of fMRI at 4.7T

It has been proposed in literature that the BOLD contrast to noise ratio increases greater than linearly in voxels containing tissues and capillaries at higher fields [8, 21]. Given that the BOLD CNR is dependent on SNR *and* ΔR_2^* (see Eqn. 44) however, the advantages of fMRI at high fields (>4T) are not as straightforward as it is often portrayed. In fact, the present findings of SNR and CNR enhancements at high fields are focused on small homogeneous regions of the brain such as the primary visual and motor cortices [5, 8, 20, 21, 23, 24], where the signal decay is mono-exponential and optimal shimming is easily achieved. Single-shot echo planar images suffer from severe signal loss, especially in frontal and temporal brain regions that are in close proximity to air/tissue interfaces (e.g. nasal cavity). The signal loss is greater at high fields since magnetic susceptibility scales with B_0. In regions close to susceptibility gradients, the signal decay is more complex [5] due to variations in local magnetic fields (phase) across the imaging region and may deviate from a mono-exponential model. Gradient echo images may then suffer from severe signal losses due to phase cancellations within voxels which may inhibit fMRI studies in some brain regions at high fields.

A recent study demonstrated activation in the fusiform face area and amygdala with single-shot gradient echo EPI at 7T using a subtle cognitive paradigm [1] which had previously not produced significant activation at lower field strengths. Studies that focus on the inferior regions of the brain or the frontal lobule are infrequent in literature however. Thus, a comprehensive fMRI study was designed here to assess the benefits of high field fMRI in homogeneous as well as inhomogeneous brain regions. In this chapter, functional MRI was experimented in six volunteers with single-shot gradient echo and spin-echo EPI at 4.7T. Even though GRE-EPI is more sensitive to the BOLD signal, it is more prone to signal loss especially in the language functional regions of brain. Consequently, SE-EPI was also evaluated for the BOLD effect since it refocuses some of the field inhomogeneities. In order to correctly assess fMRI performance at 4.7T, the experiments were replicated at the clinical 1.5T system. In order to compare the two field strengths, imaging parameters such as the sampling time, total scan time and imaging region were kept as identical as possible. In addition, the echo (TE) and repetition (TR) times were scaled for 4.7T for similar BOLD sensitivities across the two field strengths.

6.1 *Method*

6.1.1 Imaging Equipment

Functional MRI experiments were conducted on a Varian Unity INOVA whole body 4.7T MRI scanner (Palto Alto, CA) and replicated on a Siemens Sonata whole body 1.5T system (Erlangen, Germany), equipped with standard transmit/receive (T/R) head coils. Prior to EPI data acquisition, manual shimming was done on the slices, resulting in an average 20Hz water line width over the imaging region (refer to section 4.4.2). Since the primary purpose of this thesis was to assess high field fMRI across the imaging region, shimming on a very local region was not done which may result in better image quality in a very local region. Note that assessment of high field fMRI across the brain volume (despite limited coverage) is important for fMRI researchers who wish to test novel stimulation methods and identify all related activation regions.

6.1.2 Functional Imaging

Three paradigms were evaluated at 4.7T and 1.5T. They consisted of visual stimulation (flashing checkerboard and passive face viewing) and a verbal fluency task. Six subjects (21-40 years, right-handed) with normal to corrected vision were recruited from University of Alberta BME department and consented to participate in the fMRI experiments. Stimuli were programmed using Matlab (The MathWorks Inc.) and Estudio (Psychology Software Tools Inc.) and presented to the subject via a digital projection setup, identical for both systems. On the 4.7T system, subjects wore home-made prism glasses to view the projection screen; on the 1.5T system, subjects viewed the screen by a mirror attached to the coil. Button responses were recorded using fiber optic buttons (MRA Inc.) connected to the stimulus computer. To minimize head motion during scans, subjects were restrained with foam pads at 4.7T. On the 1.5T system, the head coil was equipped with adjustable bilateral plates to limit subject's movements.

Statistical analysis of data was done in SPM5 and consisted of realignment (to the first volume), smoothing with an 8mm 3D Gaussian kernel and model estimation using GLM. To evaluate the feasibility of fMRI at 4.7T, the BOLD signal change was calculated using MARSBAR toolbox and additional code written in Matlab (refer to appendix D). The BOLD signal change is defined as "the average response calculated from the plateau portion of the hemodynamic response, 8 seconds[14] after stimulus origination until stimulus termination" [11]. The BOLD signal was evaluated in a sphere of several millimeters centered on the most statistically active voxel[15]. The BOLD CNR was also calculated using Eqn. 44-45.

---

[14] The HRF rise time varies across subjects from 4-10 seconds [21].

[15] It has been observed that the highest statistical significance corresponds to the voxel with the greatest BOLD signal change.

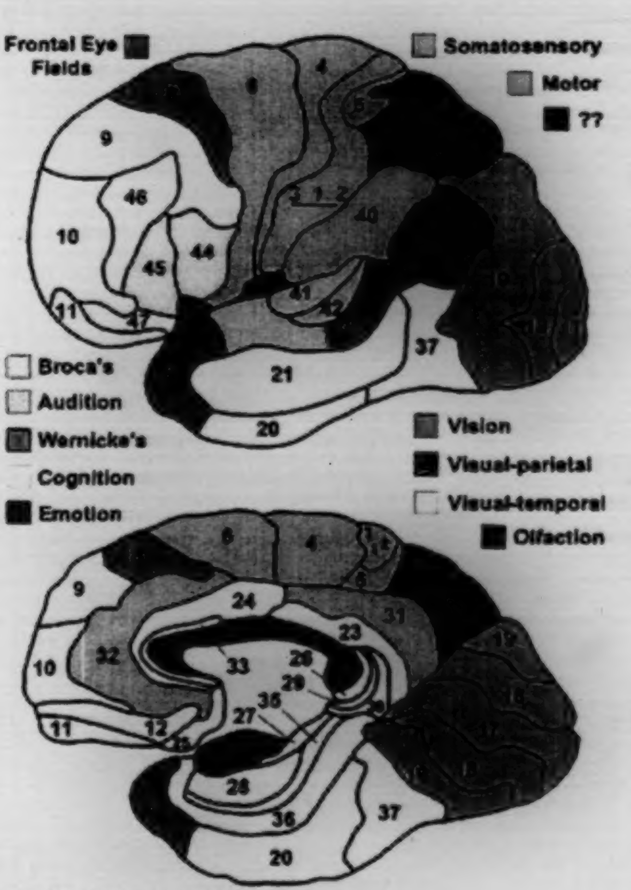
Frontal Eye Fields
Somatosensory
Motor
??
Broca's
Audition
Wernicke's
Cognition
Emotion
Vision
Visual-parietal
Visual-temporal
Olfaction
9
8
6
4
5
46
10
45
44
3 1 2
40
41
42
11
47
21
37
20
24
31
32
23
33
26
29
35
27
12
28
36
19
18

Figure 6.1.1: Outlines with functional attribution.

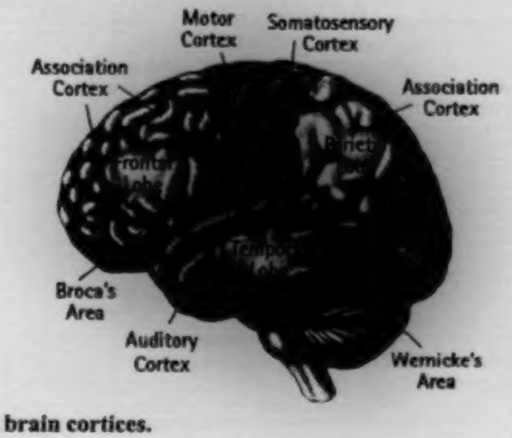
Motor Cortex
Somatosensory Cortex
Association Cortex
Association Cortex
Frontal Lobe
Parietal Lobe
Temporal Lobe
Broca's Area
Auditory Cortex
Wernicke's Area

Figure 6.1.2: Different brain cortices.

Visual stimulation (flashing checkerboard) – Homogeneous Region

Paradigm

In order to stimulate the primary visual cortex (V1) (Brodmann area 17 in Figure 6.1.1), a flashing black-white checkerboard (task) was contrasted against a black screen with a fixation cross (control). Since the occipital lobe (Figure 6.1.2) is far from regions of large magnetic susceptibility gradient, this paradigm was chosen to compare the BOLD effect at 1.5T and 4.7T in a homogeneous brain region, without concerns for significant SNR loss, which is intrinsic to areas proximal to air-tissue interfaces.

The checkerboard reversed at 8 Hz to produce the highest activation [3]. Subjects were instructed to fixate on the center of the screen and pay close attention. The experiment consisted of four repetitive cycles with alternations between 30s stimulation and 30s control condition (block-design). Four dummy scans were acquired to allow the signal to reach steady state as T_1 increases with field strength [16, 18]. The fMRI scan time[16] was four minutes.

Imaging parameters

To cover the primary visual cortex (encompassing major parts of the calcarine fissure), 20x1.5mm (gap 0.5mm) transverse oblique slices (20°) - parallel to the AC-PC line - were selected. As discussed in section 4.4.2, slice thickness may be reduced (1.5mm) to minimize through-plane intravoxel dephasing, and consequently reduce image distortions and signal loss at high fields. The phase-encode direction was in the anterior-posterior direction to minimize phase variations across the imaging region and obtain the best image quality (refer to section 4.4.2). The number of slices was limited at 4.7T to allow for good shimming and restrict SAR[17] (for SE-EPI). To keep the imaging region and SNR identical across imaging protocols with regards to hardware limitations, 20x1.9mm (gap 0.1mm) and 15x2.0mm (0.67mm) slices were chosen for GRE-EPI at 1.5T and SE-EPI at 4.7T respectively.

There is no set standard for image resolution in fMRI literature. At high fields, low resolution, 128x64 or 64x64 image matrices are common since T_2^* decays rapidly (20-30ms at 4.7T), limiting the echo train duration. For this particular paradigm, 128 x 64 images were obtained with 6/8 partial Fourier (to allow for TE used at 4.7T) with 23 cm isotropic FOV. A sampling bandwidth of 300 KHz was used at 4.7T for the fastest acquisition time to minimize the echo train length as necessitated by the intrinsic short T_2* decay. For comparison purposes and to keep SNR similar across the two fields, the highest available bandwidth (1955pix/Hz) was chosen on the 1.5T system. The imaging parameters were: TR: 3sec, TE: 25/55/50ms for GRE /SE at

---

[16] The fMRI scan time does not include the acquisition of dummy scans.

[17] SAR: specific absorption rate (W/kg)

4.7T and GRE at 1.5T respectively. The long repetition time with respect to gray matter T_1 resulted in Ernst angles close to 90° at both fields. The long TR suppresses blood inflow effects. Echo time was determined as outlined in section 5.2.1.

Verbal Fluency – Very Inhomogeneous Region

Paradigm

The study of the language area of brain is complicated by several factors. First, the use of words is a complex task which involves many linguistic subsystems (syntactic, semantic, phonological, etc.) in addition to motor function, attention and episodic memory. Consequently, to separate a unique mental process, the design and interpretation of language studies require the selection of appropriate stimulus and control conditions. Second, there is subject variability in handedness, gender, age, education and intelligence which affects the fMRI results [17]. Finally, the frontal lobe (Figure 6.1.2) is proximal to the nasal cavity and as a result is susceptible to severe signal loss and image distortions.

Since the one purpose of this thesis was to evaluate fMRI performance at 4.7T in a very inhomogeneous region such as the language cortex, a robust word generation task was selected that has consistently produced activation in the frontal lobe, lateralized strongly to the left hemisphere in right-handed subjects (Brodmann areas 44, 45, 47 in Figure 6.1.1) [2, 22]. The task condition consisted of single letter cues, randomly chosen from the English alphabet (A-Z with equal weighting) and displayed at 6 sec intervals. Subjects responded at their own pace by generating as many nouns as possible beginning with the letter, repeating them covertly (silently) and pressing a button accordingly. In the control condition, subjects were asked to repeat the word "Rest" covertly and hence press a button. The control condition prevented inadvertent word generation. Button presses were recorded to make sure subjects were engaged in the task. The experiment consisted of five repetitive cycles of each condition beginning and ending with a "REST' block. The letter and "REST" conditions lasted 30s and 20s respectively (block design). Four dummy scans were acquired to allow the signal to reach steady state. The fMRI scan time was four minutes and thirty seconds.

Imaging parameters

To avoid the nasal cavity region as much as possible, 16x1.5mm (gap 0.67mm) transverse oblique slices (15°) covered the frontal lobule. As discussed in section 4.4.2, slice thickness may be reduced to minimize through-plane intravoxel dephasing, and consequently reduce image distortions and signal loss, especially in the anterior parts of the brain that are affected by the air-tissue interfaces. The phase-encode direction was in the anterior-posterior direction to minimize phase variations across the imaging region and obtain the best image quality (refer to section 4.4.2). The number of slices was limited at 4.7T to allow for good shimming and restrain SAR (for SE-EPI). To keep the imaging region and SNR identical across imaging protocols with regards to hardware limitations, 16x1.9mm (gap 0.60mm) and 12x2.0mm (1.0mm) slices were chosen for GRE-EPI at 1.5T and SE-EPI at 4.7T respectively.

To limit echo train duration and to compare our results to available literature for this particular task, 64x64 images were obtained over an isotropic FOV of 23cm. A sampling bandwidth of 300 KHz was used at 4.7T for the fastest acquisition time to minimize the echo train length as necessitated by the intrinsic short T_2* decay. For comparison purposes, the highest available bandwidth (3906 pix/Hz) was chosen on the 1.5T system. The imaging parameters were: TR: 3sec, TE: 20/55/50ms for GRE /SE at 4.7T and GRE at 1.5T respectively. The long repetition time with respect to gray matter T_1 resulted in Ernst angles close to 90°. The long TR suppresses blood inflow effects. For 4.7T experiment, the echo time was reduced to 20ms to compensate for signal loss in the language cortex associated with field inhomogeneities. Echo time was determined as outlined in section 5.2.1

Visual Stimulation (Face Perception) – Inhomogeneous Region

Paradigm

Behavioral literature suggests that different types of visual stimulus such as faces, objects, scenery and houses may involve distinct brain mechanisms. Kanwisher [13-15] for instance provided evidence of dissociation between face and object recognition in humans. She coined the face association area as Fusiform Face Area (FFA) located in the inferior fusiform gyrus, lateralized more strongly to the right hemisphere.

Figure 6.1.3: Diagram of the FFA with transverse and coronal cuts revealing the site of this region.

In theory, functional MRI benefits from higher sensitivity at high fields. However, as discussed in the introduction, the higher BOLD effect has been observed mostly in homogeneous regions of the brain such as the primary visual and motor cortices. To test this hypothesis in a relatively inhomogeneous region, a higher cognitive paradigm was designed that mirrored the passive face viewing paradigm used in

[14]. The face perception paradigm consisted of two conditions. In the first condition, subjects viewed gray-scale photographs of faces with neutral expressions. The face images used in this work have been provided by the Computer Vision Laboratory, University of Ljubljana, Slovenia [25]. The database consists of 114, 640x480 pixel color photographs of individuals (90% male). The object database was obtained from various sources and consisted of everyday familiar objects such as cups, pots and chairs. The photographs were converted to gray-scale in Matlab with identical window and level (refer to Appendix C). The paradigm consisted of six cycles of face viewing alternated with object viewing. The face and object viewing conditions lasted 30 and 20 sec respectively (block design), with one photograph presented per second. The photos were assembled into an AVI video file in Matlab and presented to the subject via the projection system. The fourth face block was identical to the first block, fifth face block was identical to the second block and so on. The object blocks were different throughout. Four dummy scans were acquired to allow the signal to reach steady state. The fMRI scan time was five minutes.

Imaging Parameters

To cover the inferior fusiform gyrus area, 25x1.5mm transverse slices were selected. As discussed in the previous sections, the slice thickness was kept small to minimize image distortions and signal loss, intrinsic to inhomogeneous field regions. The phase-encode direction was in the anterior-posterior direction to minimize phase variations across the imaging region and obtain the best image quality (refer to section 4.4.2). The number of slices was limited at 4.7T to allow for local shimming and restrain SAR (for SE-EPI). To keep the imaging region and SNR identical across imaging protocols with regards to hardware limitations, 18x2.0mm slices were chosen for GRE-EPI at 1.5T and SE-EPI at 4.7T.

Kanwisher measured the FFA areas as $1cm^2$ and $0.5cm^2$ in the right and left hemispheres respectively. Due to the small activation region and to minimize partial volume averaging effects, 128 x 64 images were obtained with 6/8 partial Fourier (to allow for TE used at 4.7T) with 23 cm isotropic FOV. A sampling bandwidth of 300 KHz was used at 4.7T for the fastest acquisition time to minimize the echo train length as necessitated by the intrinsic short T_2* decay. For comparison purposes, the highest available bandwidth (1955 pix/Hz) was chosen on the 1.5T system. The imaging parameters were: TR: 3sec, TE: 18/55/50ms for GRE /SE at 4.7T and GRE at 1.5T respectively. The long repetition time with respect to gray matter T_1 resulted in Ernst angles close to 90°. The long TR suppresses blood inflow effect. For 4.7T experiment, the echo time was reduced to 18ms to compensate for signal loss in the inferior brain regions associated with field inhomogeneities. Echo time was determined as outlined in section 5.2.1.

6.2 Results

To evaluate functional MRI performance at 4.7T, the BOLD signal change in addition to BOLD contrast to noise ratio were calculated as specified in the method section of this chapter. Echo planar images were also assessed across the two fields.

6.2.1 Flashing checkerboard

The following table lists the average BOLD signal change in an 8mm (radius) sphere, centered on the most statistically active voxel in the primary visual cortex (V1). Note that the activation clusters closely matched across the three imaging protocols for a subject. The results are shown at $p_{corr} < 0.01$.

Table 6.2.1: Average BOLD signal change (%) in an 8mm (radius) sphere in the V1.

	Subjects						
Method	1	2	3	4	5	6	Mean[b]
$GRE_{4.7T}$	5.1	4.8	3.0	4.7	3.0	3.5	4.0 ± 1.0
$GRE_{1.5T}$	1.6	N/S[a]	2.0	1.8	1.3	2.0	1.7 ± 0.3
$SE_{4.7T}$	3.6	N/S	N/S	2.8	N/S	N/S	3.2 ± 0.6
$GRE_{4.7T}/GRE_{1.5T}$	2.3 ± 0.7[c]						

[a] *N/S: Not statistically significant*
[b] *Mean calculated from successful trials*
[c] *Significant at p < 0.0104 (paired sample t-test)*

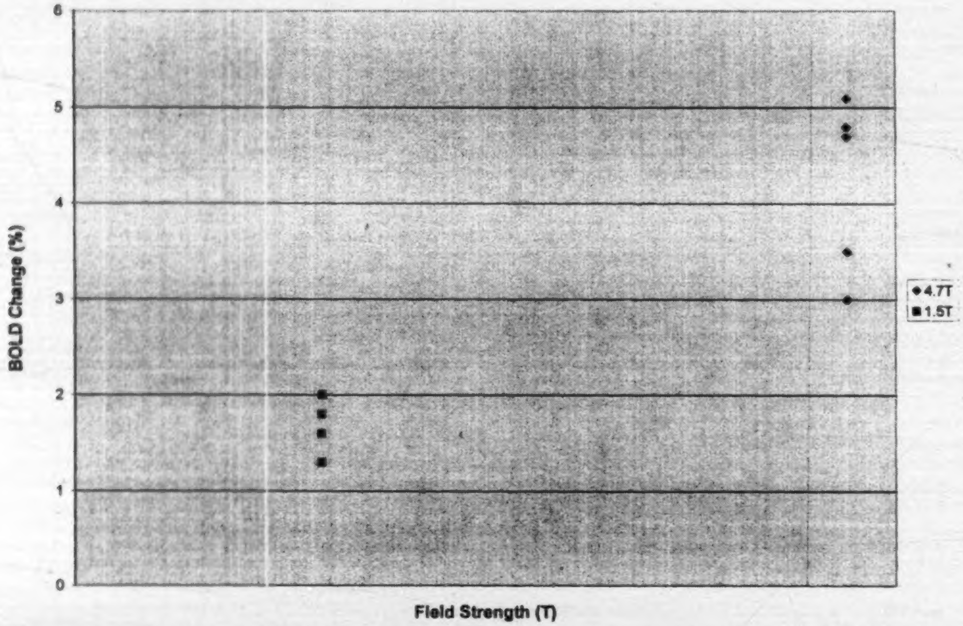

Figure 6.2.1: Scatter plot showing the BOLD signal change in the primary visual cortex across the 1.5T and 4.7T field strengths for six subjects. The BOLD signal change ranged from 1-2% and 3-6% at 1.5T and 4.7T respectively.

As seen from Table 6.2.1 , the average GRE BOLD signal change was 4.0% and 1.7% at 4.7T and 1.5T respectively. The SE imaging protocol did not produce statistically significant result for most subjects. Note that statistical insignificant does not imply the nonexistence of activation. The spin-echo sequence is not as sensitive to the BOLD signal as its GRE counterpart since the static component (large vessels) of the EV BOLD effect is refocused (refer to section 3.3.2). Thus, SE BOLD effect is smaller than the GRE BOLD effect and may require more volume acquisition for statistical significance. In fact, activation was found in SE results once the statistical threshold was significantly lowered ($p_{uncorr}<0.05$). Regardless, the average SE BOLD signal change was 3.2% across subjects 1 and 4 which is less than the average GRE BOLD signal change of 4.9% which has contributions from both large and small vessels.

The following figure shows the fMRI time-course for the most statistically significant voxel in the primary visual cortex. Note the clear distinction between the task and control conditions in all time-courses, and the higher BOLD effect at 4.7T.

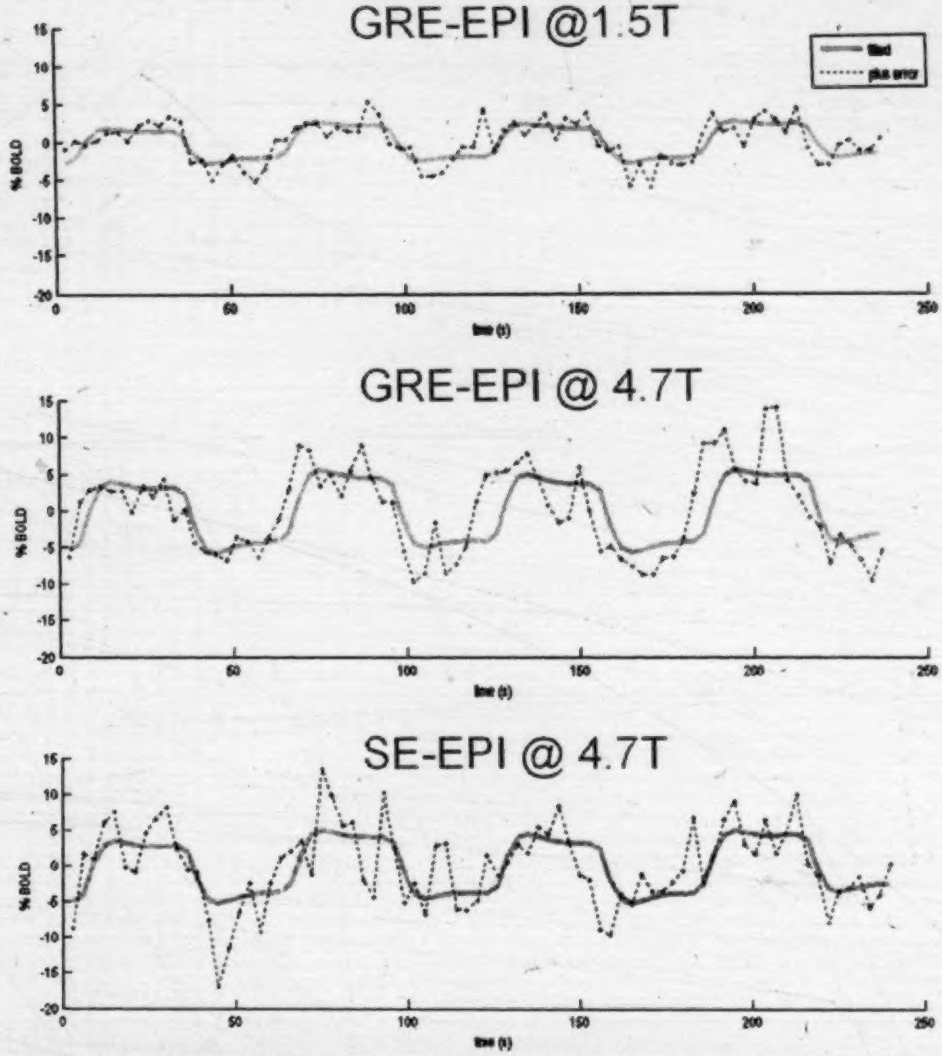

Figure 6.2.2: fMRI time-course for the most statistically significant voxel in the primary visual cortex. Shown is the BOLD signal change as the function of scan time.

It is usual practice to overlay functional maps on high resolution anatomical images. Since image quality is of concern in this thesis, the statistical functional maps (t-maps) are overlaid on EPI images instead.

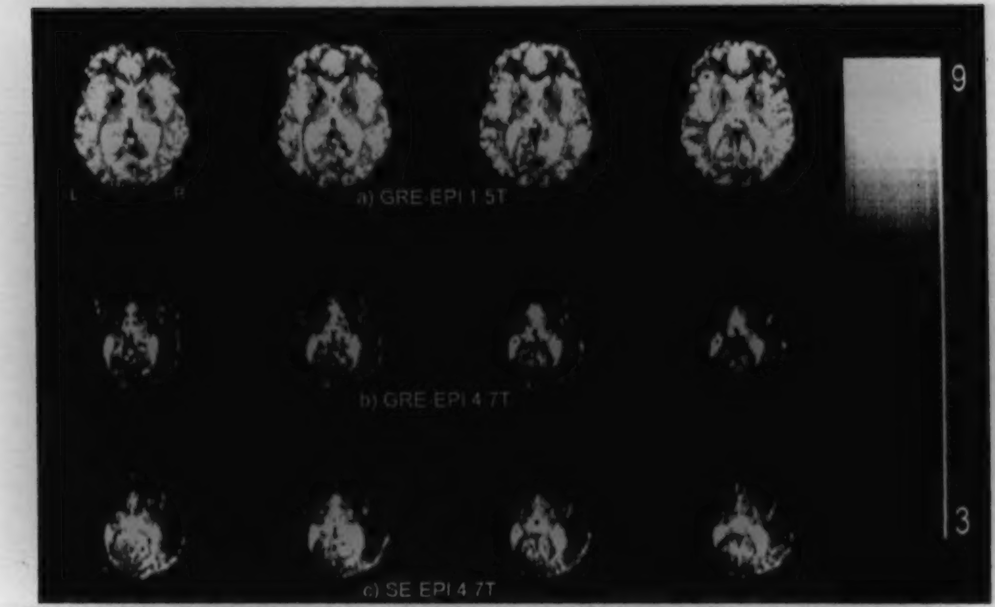

Figure 6.2.3: Activation map (t-statistics) overlaid on EPI images. The activation map is from the same subject with similar slices across the three imaging protocols. The BOLD signal change was 5.1/ 3.6% for GRE/SE at 4.7T and 1.6% for GRE at 1.5T.

Figure 6.2.3 shows that the anterior brain regions suffer from image distortions and poor shim at 4.7T. The spin echo sequence refocuses some of the field inhomogeneities in the anterior regions resulting in less image distortions. Note however that the SE sequence is more sensitive to the inhomogeneous RF field to the additional refocusing pulse as evident in signal intensity variations across the slice (refer to 4.4.3). The gradient echo images at 1.5T do not show any observable signs of image distortion. Since the primary visual cortex was of concern in this paradigm, SNR was calculated using the background estimation method (section 3.4).

Table 6.2.2: SNR calculations for a ROI in the primary visual cortex.

Subject	GRE 4.7T	SE 4.7T	GRE 1.5T
1	53	30	35
2	59	23	31
3	80	19	43
4	58	46	33
5	76	25	44
6	74	29	32
Mean	66.7 ± 11.3	28.7 ± 9.4	36.3 ± 5.7
$GRE_{4.7T}/GRE_{1.5T}$	1.85 ± 0.27[a]		

[a] *Significant at* $p < 0.0003$

As seen from Table 6.2.2, SNR is highest for gradient-echo images at 4.7T. The average GRE SNR increased by approximately two-folds at the higher field.

BOLD CNR

The BOLD CNR determines the sensitivity and thus the accuracy of the fMRI results. As discussed in section 3.4, ΔR_2^* and the maximum BOLD CNR is predicted to increase greater than linearly with field strength in GRE images. This would imply a CNR gain of $(4.7/1.5) = 3.1$ (linear) **up to** $(4.7/1.5)^2 = 9.8$ (quadratic) at the higher field. Since the actual fMRI performance (in EPI images) was of concern here, the BOLD CNR in the primary visual cortex was calculated using SNR calculations in Table 6.2.2, the BOLD signal change ($\Delta S/S$) measurements in Table 6.2.1, typical T_2^* values of 69.4ms and 22.6ms [12] at 1.5T and 4.7T and TE: 25ms/50ms at 4.7T/1.5T. The following table lists ΔR_2^* values (Eqn. 45):

Table 6.2.3: ΔR_2^* (s^{-1}) calculations in the primary visual cortex.

	Subjects						
Method	1	2	3	4	5	6	Mean[b]
$GRE_{4.7T}$	-2.04	-1.92	-1.20	-1.88	-1.20	-1.40	-1.61 ± 0.38
$GRE_{1.5T}$	-0.32	N/A[a]	-0.40	-0.36	-0.26	-0.40	-0.35 ± 0.059
$\Delta R^*_{2,4.7T}/\Delta R^*_{2,1.5T}$	6.38	N/A	3.00	5.22	4.62	3.50	4.54 ± 1.35[c]

[a] *N/A: Not available*

[b] *Mean calculated from successful trials*

[c] *Significant at $p < 0.003$*

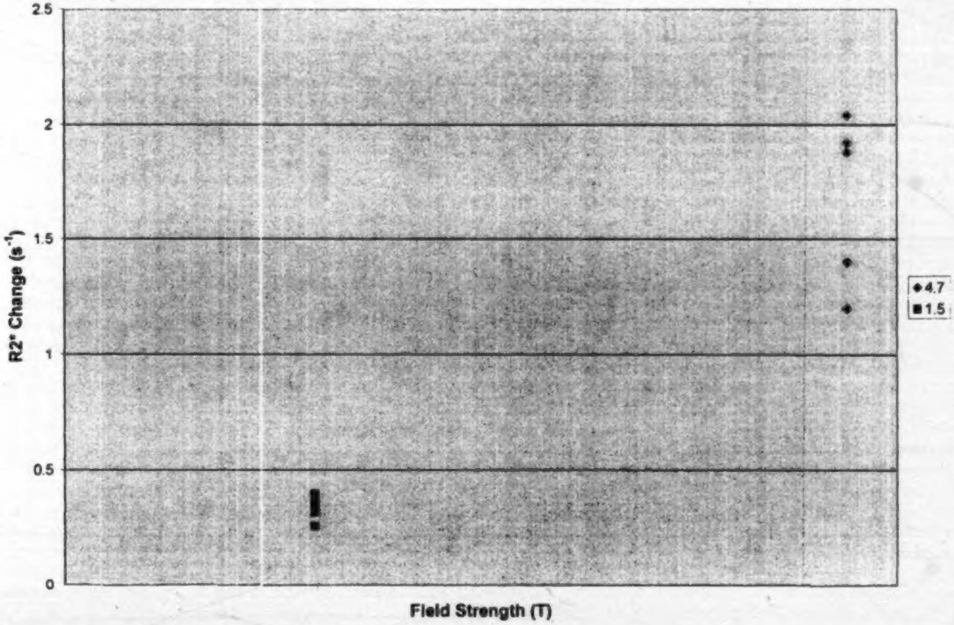

Figure 6.2.4: Scatter plot showing ΔR_2^* in the primary visual cortex across the 1.5T and 4.7T field strengths for six subjects.

The ΔR_2^* values calculated above agree well with $\Delta R^*_{2,1.5T} = -0.32 s^{-1}$ and $\Delta R^*_{2,4.7T} = -1.2625\ s^{-1}$, interpolated from 0.5T, 1.5T and 4T in the primary visual cortex [8], and indicates a greater than linear increase as predicted in previous models at higher fields. Using ΔR_2^* values, the BOLD CNR was calculated (Eqn. 44). The following table lists the BOLD CNR:

Table 6.2.4: BOLD CNR calculations in the primary visual cortex.

	Subjects						
	1	2	3	4	5	6	Mean[b]
$GRE_{4.7T}$	2.44	2.56	2.17	2.46	2.061	2.34	2.34± 0.19
$GRE_{1.5T}$	0.78	N/A[a]	1.19	0.82	0.79	0.89	0.89 ± 0.17
$CNR_{4.7T}/CNR_{1.5T}$	3.13	N/A	1.82	3.00	2.61	2.63	2.64 ± 0.51[c]

[a] *N/A: Not available*

[b] *Mean calculated from successful trials*

[c] *Significant at $p < 0.0004$*

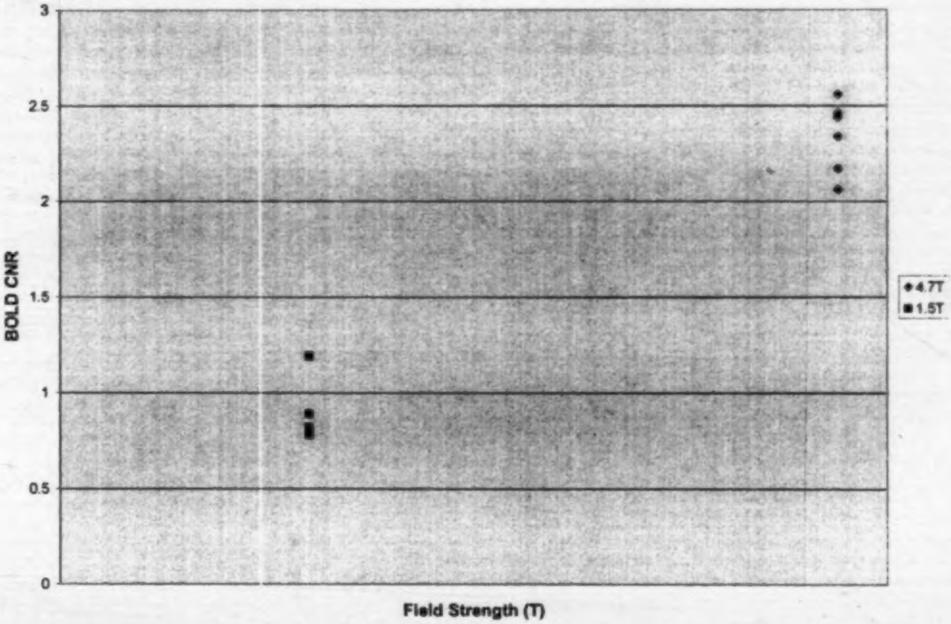

Figure 6.2.5: Scatter plot showing BOLD CNR in the primary visual cortex across the 1.5T and 4.7T field strengths.

The mean GRE BOLD CNR gain ranges from 2.13 to 3.15 at 4.7T, which indicates an utmost linear increase across the two fields. Since the maximum BOLD CNR increase is predicted as greater than linear at higher field in previous models using conventional GRE images, the actual BOLD CNR calculations here, using the suboptimal SNR in EPI images are very promising and nonetheless indicate an overall gain.

6.2.2 Verbal Fluency

The following table lists the average BOLD signal change in a 4mm (radius) sphere, centered on the most statistically active voxel in the left inferior frontal gyrus (IFG). Note that the activation clusters approximately matched across the three imaging protocols for a subject. The results are shown at $p_{corr} < 0.01$.

Table 6.2.5: Average BOLD signal change (%) in a 4mm (radius) sphere in the left IFG. Also included are the button responses, outlined below each session correspondingly.

	Subjects						
Method	1	2	3	4	5	6	Mean[b]
$GRE_{4.7T}$	2.8	2.1	3.7	1.7	1.4	N/S[a]	2.3 ± 0.9
Button Response	89	120	111	85	73	65	88 ± 21
$GRE_{1.5T}$	N/S	N/S	2.0	N/S	1.8	1.4	1.7 ± 0.3
Button Response	90	113	109	104	76	85	96 ± 15
$SE_{4.7T}$	3.4	N/S	N/S	N/S	2.4	N/S	2.9 ± 0.7
Button Response	74	105	106	71	71	76	81 ± 17

[a] *N/S: Not statistically significant*

[b] *Mean calculated from successful trials*

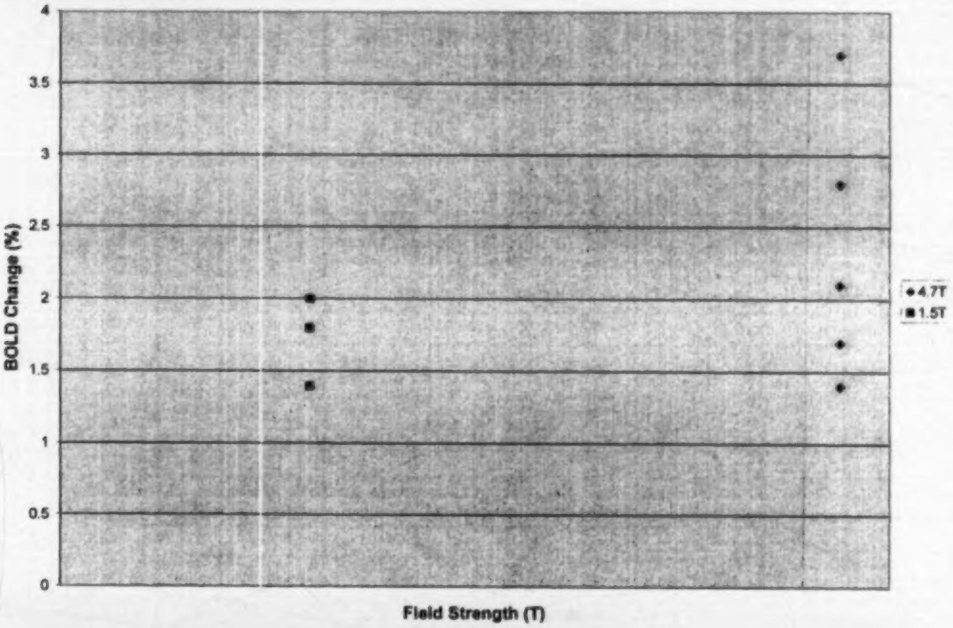

Figure 6.2.6: Scatter plot showing the BOLD signal change in the left IFG across the 1.5T and 4.7T field strengths for six subjects. The BOLD signal change ranges from 1-2% and 1-4% at 1.5T and 4.7T respectively. Note that only three subjects showed statistically significant activation at 1.5T.

As seen from Table 6.2.5, the average GRE BOLD signal change was 2.9% for the first three subjects and 1.5% for subjects 4 and 5 at 4.7T. Subject 6 did not show statistically significant activation in the region of interest. Coincidently, her button response was fewer than the other subjects which may indicate that she was not as involved in the fMRI study. Note in Table 6.2.5 that there are large variations in subject response due to differences in age, gender, intelligence, etc. The average SE BOLD signal change was 2.9% as compared to GRE BOLD signal change of 2.1% across subjects 1 and 5. Considering large amplitude variations in SE fMRI time-courses (refer to Figure 6.2.7), it is suspected that SE clusters were situated on large vessels which may also explain the unusual large change in the SE BOLD signal (IV BOLD effect). However, since relatively low resolution images (i.e. 128x64) were acquired, the IV and EV BOLD components can not be separated. The average GRE BOLD signal change was 1.7% across subjects 3, 5 and 6 at 1.5T.

The SNR was measured in the inferior frontal lobe (activation region) in addition to other brain regions for comparison purposes (for more information on SNR calculations, refer to section 3.4). The measurements are listed in the following tables:

Table 6.2.6: SNR calculations for a ROI in the inferior frontal lobe (activation region).

Subject	GRE 4.7T	SE 4.7T	GRE 1.5T
1	61	36	33
2	62	30	33
3	53	36	23
4	37	15	34
5	52	31	40
6	57	40	33
Mean	53.7 ± 9.1	31.3 ± 8.8	32.7 ± 5.5
$GRE_{4.7T}/GRE_{1.5T}$	1.69 ± 0.44^a		

[a] *Significant at $p < 0.006$*

Table 6.2.7: SNR calculations for a ROI in the most anterior-inferior frontal lobe.

Subject	GRE 4.7T	SE 4.7T	GRE 1.5T
1	22	28	32
2	39	23	34
3	30	29	27
4	30	17	36
5	17	24	44
6	18	32	38
Mean	26.0 ± 8.5	25.5 ± 5.3	35.2 ± 5.7
$GRE_{4.7T}/GRE_{1.5T}$	0.77 ± 0.32^a		

[a] *Significant at $p < 0.1$*

Table 6.2.8: SNR calculations for a ROI in the posterior-inferior regions.

Subject	GRE 4.7T	SE 4.7T	GRE 1.5T
1	74	42	32
2	72	43	35
3	78	49	29
4	50	37	34
5	78	47	43
6	51	61	38
Mean	67.2 ± 13.1	46.0 ± 8.2	35.1 ± 4.9
$GRE_{4.7T}/GRE_{1.5T}$	1.95 ± 0.51[a]		

[a] *Significant at $p < 0.003$*

As seen from Table 6.2.6, there is an overall gain in SNR in the activation region (left IFG) at 4.7T. Table 6.2.7 shows that there is severe signal loss in the most anterior regions of the frontal lobe at 4.7T. The measured SNR in that region actually falls below the 1.5T value for most subjects. For other regions, the GRE 4.7T images have higher SNR as expected (Table 6.2.8).

The following figure shows the time-course for the most statistically significant voxel in the left inferior frontal gyrus for the three imaging protocols. Note that SE resulted in a noisier time-course than GRE imaging protocols. As explained before, this may be attributed to a large IV component.

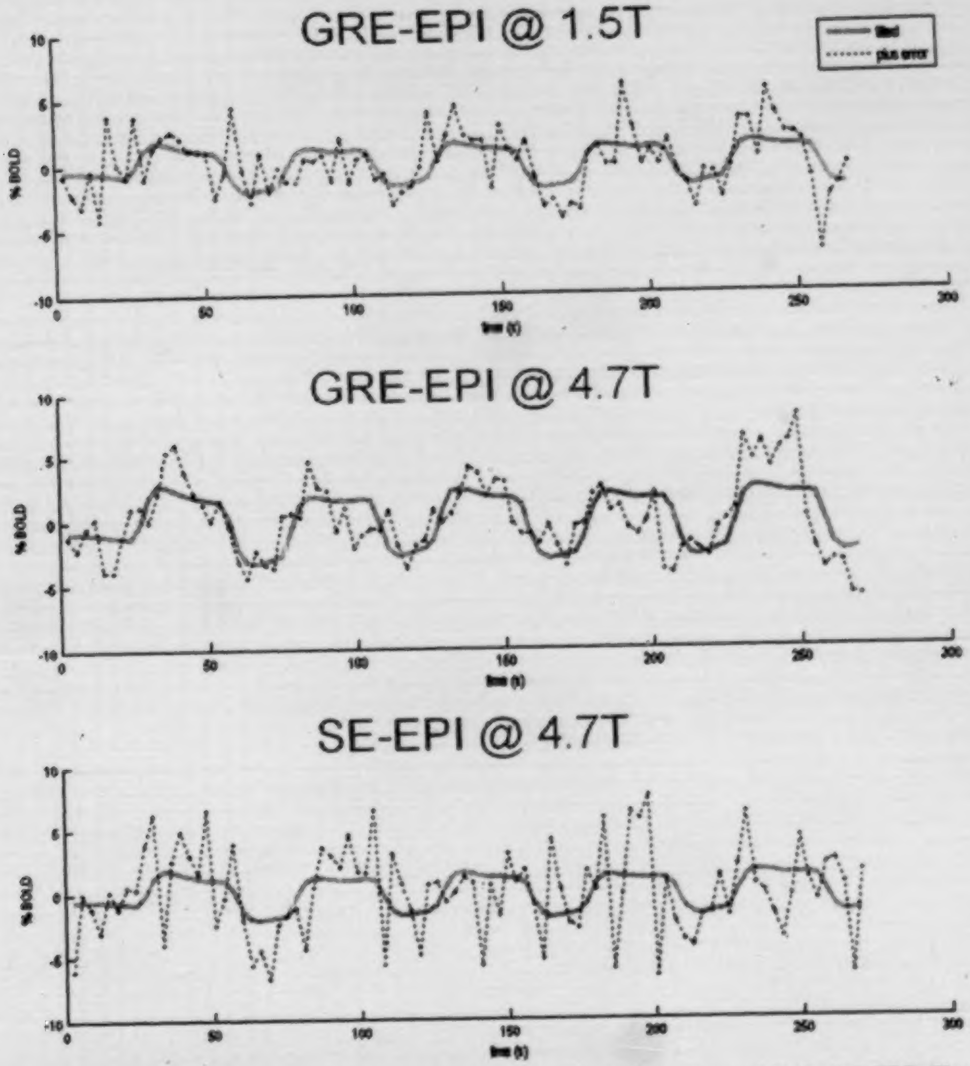

Figure 6.2.7: fMRI time-course for the most statistically significant voxel in the left IFG. Shown is the BOLD signal change as the function of scan time.

The following figure shows the activation map (t-statistics) overlaid on actual EPI images. Note the severe signal loss in the frontal cortex area in gradient echo images at 4.7T.

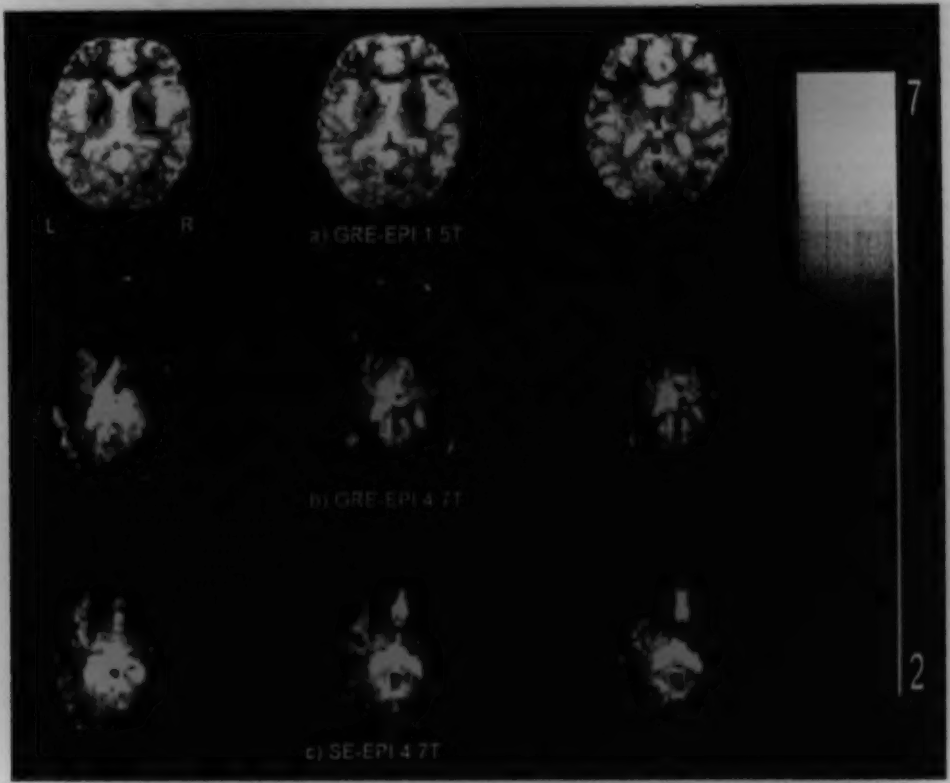

Figure 6.2.8: Activation map (t-statistics) overlaid on EPI images. The activation map is from the same subject with similar slices across the three imaging protocols. The red arrow indicates the activation region in the left IFG. The BOLD signal change was 1.4/2.4% for GRE /SE at 4.7T and 1.8% for GRE at 1.5T. Note that the single streak in the far left slice in b) is due to nonlinear phase correction for EPI image reconstruction.

BOLD CNR

As shown in the previous section, ΔR_2^* and GRE BOLD CNR increased greater than linearly and (at most) linearly with field strength respectively. However, the former study was based in the primary visual cortex, and the proposed SNR and CNR improvements at high field by such researchers as Gati and Menon [8, 21 and 24] are often based on homogeneous regions of the brain such the occipital and motor cortices as well. Thus, to test this hypothesis in the frontal lobe, the BOLD CNR was again calculated (refer to the previous section for more details) using SNR calculations in the activation region (Table 6.2.6).

Table 6.2.9: ΔR_2^* (s^{-1}) calculations in the frontal lobe.

	Subjects						
Method	1	2	3	4	5	6	Mean[b]
GR-EPI$_{4.7T}$	-1.40	-1.05	-1.85	-0.85	-0.70	N/A[a]	-1.17 ± 0.46
GRE-EPI$_{1.5T}$	N/A	N/A	-0.40	N/A	-0.36	-0.28	-0.35 ±0.061
$\Delta R^*_{2,4.7T}/\Delta R^*_{2,1.5T}$	N/A	N/A	4.63	N/A	1.94	N/A	3.28 ± 1.89

[a] *N/A: Not available*

[b] *Mean calculated from successful trials*

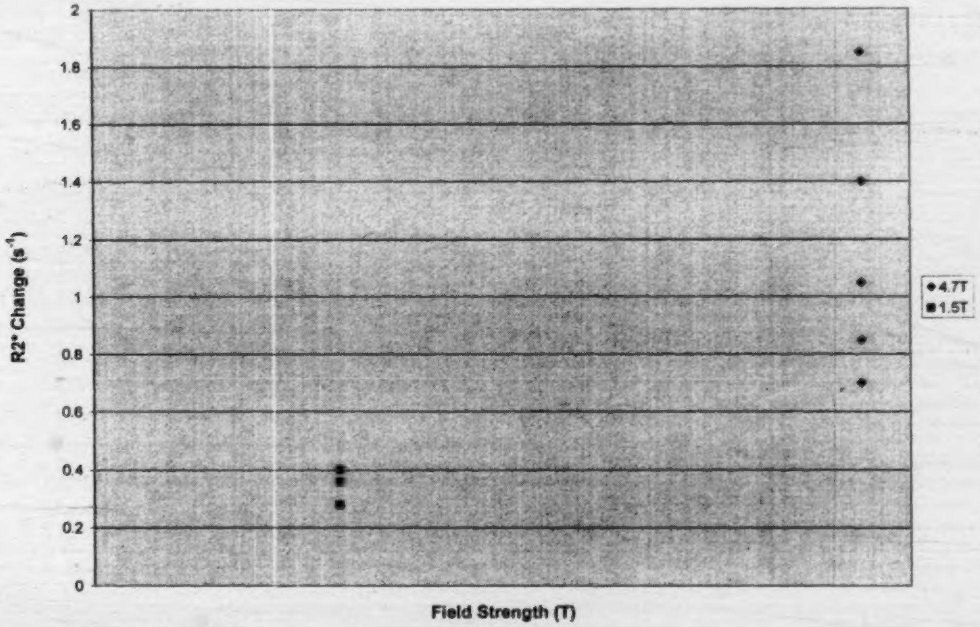

Figure 6.2.9: Scatter plot showing ΔR_2^* in the left IFG across the 1.5T and 4.7T field strengths for six subjects.

The following table lists the BOLD CNR (Eqn. 44):

Table 6.2.10: BOLD CNR calculations in the frontal lobe.

	Subjects						
	1	2	3	4	5	6	Mean[b]
GR-EPI$_{4.7T}$	1.93	1.47	2.22	0.71	0.82	N/A[a]	1.43 ± 0.66
GRE-EPI$_{1.5T}$	N/A	N/A	0.64	N/A	1.00	0.64	0.76 ± 0.20
CNR$_{4.7T}$/CNR$_{1.5T}$	N/A	N/A	3.47	N/A	0.82	N/A	2.14 ± 1.87

[a] *N/A: Not available*

[b] *Mean calculated from successful trials*

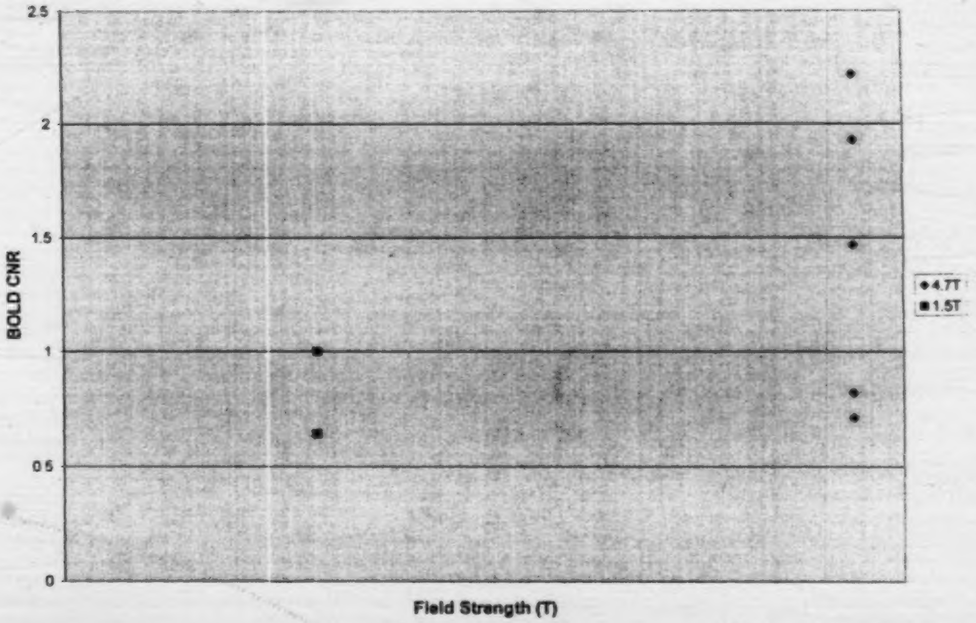

Figure 6.2.10: Scatter plot showing BOLD CNR in the left IFG across the 1.5T and 4.7T field strengths.

Table 6.2.10As seen from Figure 6.2.10, the GRE BOLD CNR increases for most subjects across the two fields. Note that if the desired activation region was in the most anterior regions of the frontal lobe where the SNR fell below the 1.5T values (Table 6.2.7), no gain in BOLD CNR would be expected since BOLD CNR is dependent on both SNR and the BOLD effect.

6.2.3 Face Perception

The following table lists the average BOLD signal change in a 2mm (radius) sphere, centered on the most statistically active voxel in the fusiform gyrus region. As pointed out in [14], the FFA area may be detected bilaterally in the fusiform gyrus area. Hence, the results are presented separately for the left and right FFA in the following tables, shown at $p_{unpcorr} < 0.0001$. Note that the activation clusters matched across the imaging protocols for a subject.

Table 6.2.11: Average BOLD signal change (%) in a 2mm (radius) sphere in the right FFA.

	Subjects						
Method	1	2	3	4	5	6	Mean[b]
GRE$_{4.7T}$	N/S[a]	1.8	N/S	1.5	N/S	1.2	1.5 ± 0.30
GRE$_{1.5T}$	N/S	N/S	N/S	2.6	N/S	3.6	3.1 ± 0.71
SE$_{4.7T}$	N/S						

[a] *N/S: Not statistically significant*

[b] *Mean calculated from successful trials*

Table 6.2.12: Average BOLD signal change (%) in a 2mm (radius) sphere in the left FFA.

	Subjects						
Method	1	2	3	4	5	6	Mean[b]
$GRE_{4.7T}$	N/S[a]	2.1	N/S	2.5	N/S	2.3	2.3 ± 0.33
$GRE_{1.5T}$	N/S	N/S	N/S	1.5	N/S	N/S	1.5
$SE_{4.7T}$	N/S						

[a] *N/S: Not statistically significant*

[b] *Mean calculated from successful trials*

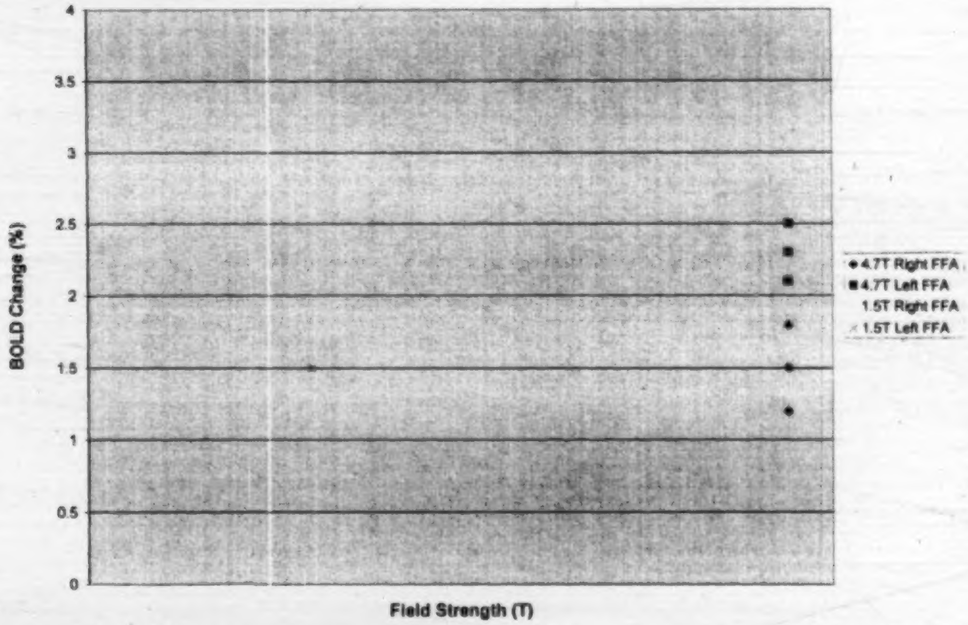

Figure 6.2.11: : Scatter plot showing the BOLD signal change in the right and left FFA across the 1.5T and 4.7T field strengths for six subjects.

The FFA area was detected in 50% and 33% of the subjects in the 4.7T and 1.5T GRE experiments. Since there were no visible signs of the FFA area in 20% (3/15) of the volunteers in [14], it is possible that this region may not be detectable in some normal subjects. The Kanwisher's 1.5T results were improved by using a surface coil and employing two averages and longer scan times. Kanwisher has previously demonstrated that the FFA is more lateralized to the right hemisphere. This was the case here for subjects 4 and 6 in the 1.5T results. The 4.7T results were lateralized to the left hemisphere however. Subject 4 was scanned twice for reliability and this was again the case. Even though no major conclusions can be made in this regard since the sample size is not large enough, the results can not be attributed to shim and SNR differences across the hemispheres as they are approximately equal (Table 6.2.13 and Table 6.2.14).

The GRE result clearly demonstrates that the 4.7T system may be used for higher cognitive studies. The SE protocol did not detect activation in the FFA which implies that SE is not as sensitive to the BOLD signal as GRE and may require longer scan times for statistical significance. The activation map (t-statistics), overlaid on EPI images is shown below. Note in Figure 6.2.13 that GRE images suffer from greater signal loss in the anterior brain regions at 4.7T due to larger susceptibility gradients.

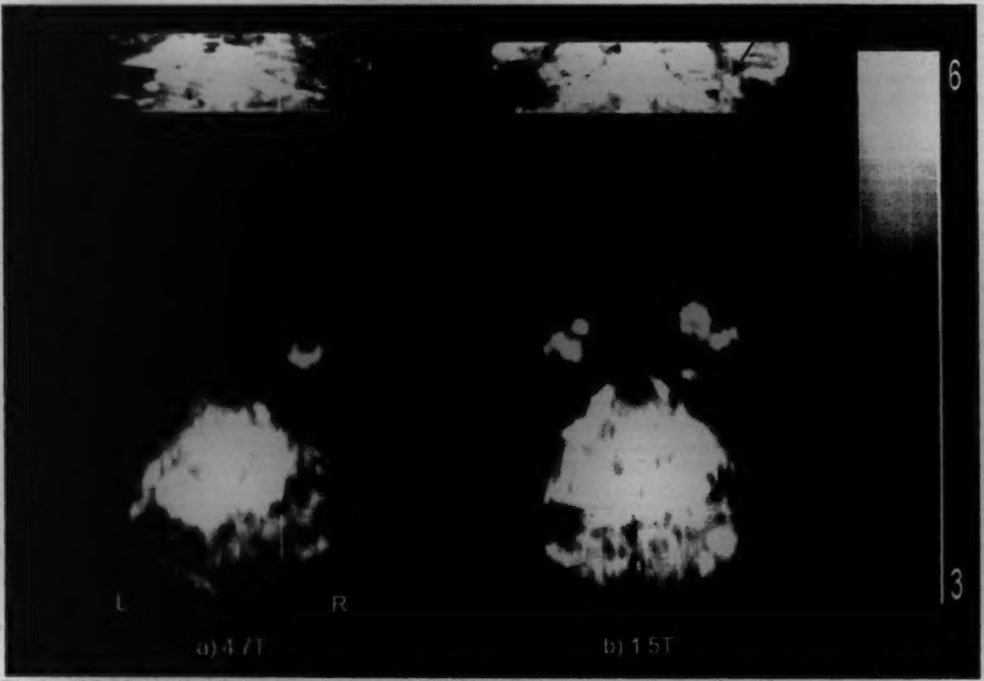

Figure 6.2.12: Activation map (t-statistics) overlaid on actual EPI images. The activation map is from the same subject with similar slices across the three imaging protocols. Note that the red arrow in the coronal slice indicates the activation region in the right fusiform gyrus area. The BOLD signal change was 1.2/3.6% for GRE at 4.7T and at 1.5T respectively.

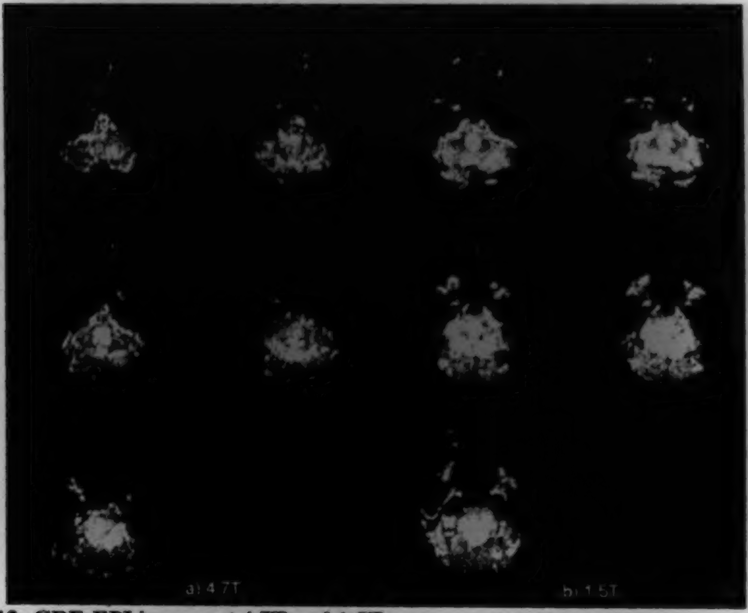

Figure 6.2.13: GRE-EPI images at 4.7T and 1.5T.

The following figures show the time-course for the most statistically active voxel in the right FFA.

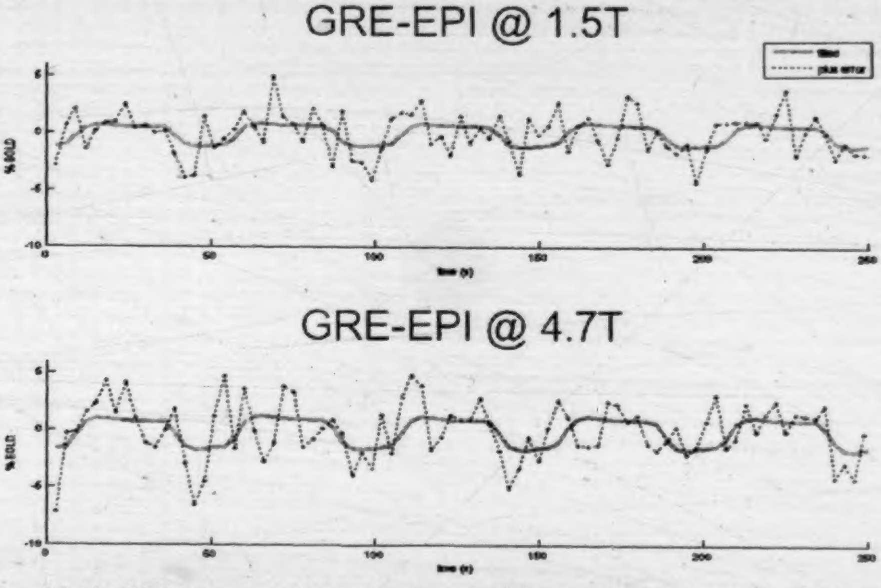

Figure 6.2.14: fMRI time-course for the most statistically significant voxel in the right FFA. Shown is the BOLD signal change as the function of scan time.

SNR was calculated in a slice for all three imaging protocols in the left and right FFA areas (for more information on SNR calculations, refer section 3.4).

Table 6.2.13: SNR calculations for a slice located in the right FFA.

Subject	GRE 4.7T	SE 4.7T	GRE 1.5T
1	88	14	35
2	69	19	40
3	82	22	49
4	73	N/A	41
5	75	20	50
6	79	16	40
Mean	77.7 ± 6.8	18.2 ± 3.2	42.5 ± 5.8
$GRE_{4.7T}/GRE_{1.5T}$	1.86 ± 0.36^a		

[a] *Significant at p <0.0003*

Table 6.2.14: SNR calculations for a slice located in the left FFA.

Subject	GRE 4.7T	SE 4.7T	GRE 1.5T
1	87	13	35
2	79	20	40
3	88	19	48
4	82	N/A	38
5	69	22	50
6	74	18	40
Mean	79.8 ± 7.4	18.4 ± 3.4	41.8 ± 5.9
$GRE_{4.7T}/GRE_{1.5T}$	1.95 ± 0.37^a		

[a] *Significant at p <0.0004*

The mean SNR increased by approximately two-folds in the GRE images at the higher field for both right and left FFA. This result which is comparable to the SNR calculations in Table 6.2.2 and Table 6.2.8 shows that lowering the echo time in addition to using smaller voxel dimensions compensate for some of the SNR loss, allowing for fMRI studies that cover the inferior regions of the brain. Also note that the fusiform gyrus region is not as inhomogeneous (field) as the anterior frontal lobule which is proximal to large susceptibility gradients (Table 6.2.7).

BOLD CNR

As shown in sections 6.2.1 and 6.2.2 , ΔR_2^* and BOLD CNR increased with field strength in GRE images. To test this in the fusiform gyrus region, the ΔR_2^* and actual BOLD CNR were calculated again using Eqn. 44-45 (refer to section 6.2.1 for details).

Table 6.2.15: ΔR_2^* (s^{-1}) calculations in the right FFA.

	Subjects						
Method	1	2	3	4	5	6	Mean[b]
$GRE_{4.7T}$	N/A[a]	-1.00	N/A	-0.83	N/A	-0.67	-0.83 ± 0.17
$GRE_{1.5T}$	N/A	N/A	N/A	-0.52	N/A	-0.72	-0.62 ± 0.14
$\Delta R^*_{2,4.7T}/\Delta R^*_{2,1.5T}$	N/A	N/A	N/A	1.60	N/A	0.93	1.27 ± 0.47

[a] *N/A: Not available*

[b] *Mean calculated from successful trials*

Table 6.2.16: ΔR_2^* (s^{-1}) calculations in the left FFA.

	Subjects						
Method	1	2	3	4	5	6	Mean[b]
$GRE_{4.7T}$	N/A[a]	-1.17	N/A	-1.37	N/A	-1.28	-1.30 ± 0.18
$GRE_{1.5T}$	N/A	N/A	N/A	-0.83	N/A	N/A	-0.30
$\Delta R^*_{2,4.7T}/\Delta R^*_{2,1.5T}$	N/A	N/A	N/A	4.57	N/A	N/A	4.57

[a] N/A: Not available

[b] Mean calculated from successful trials

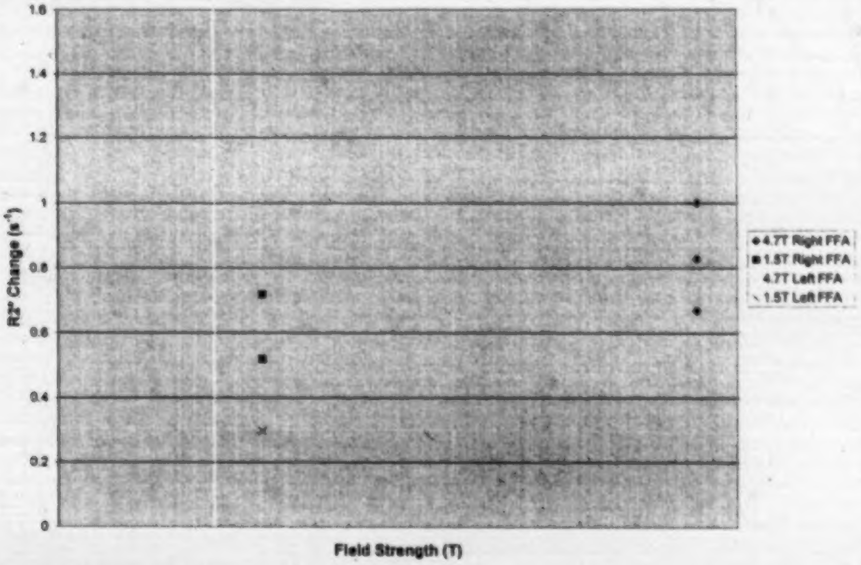

Figure 6.2.15: Scatter plot showing ΔR_2^* in the right/left FFA across the 1.5T and 4.7T field strengths for six subjects.

Table 6.2.17: BOLD CNR calculations in the right FFA.

	Subjects						
	1	2	3	4	5	6	Mean[b]
$GRE_{4.7T}$	N/A[a]	1.56	N/A	1.37	N/A	1.20	1.38 ± 0.18
$GRE_{1.5T}$	N/A	N/A	N/A	1.48	N/A	2.00	1.74 ± 0.37
$CNR_{4.7T}/CNR_{1.5T}$	N/A	N/A	N/A	0.93	N/A	0.60	0.77 ± 0.23

[a] N/A: Not available

[b] Mean calculated from successful trials

Table 6.2.18: BOLD CNR calculations in the left FFA.

	Subjects						
	1	2	3	4	5	6	Mean[b]
$GRE_{4.7T}$	N/A[a]	2.089	N/A	2.53	N/A	2.14	2.25 ± 0.24
$GRE_{1.5T}$	N/A	N/A	N/A	0.79	N/A	N/A	0.79
$CNR_{4.7T}/CNR_{1.5T}$	N/A	N/A	N/A	3.20	N/A	N/A	3.20

[a] N/A: Not available

[b] Mean calculated from successful trials

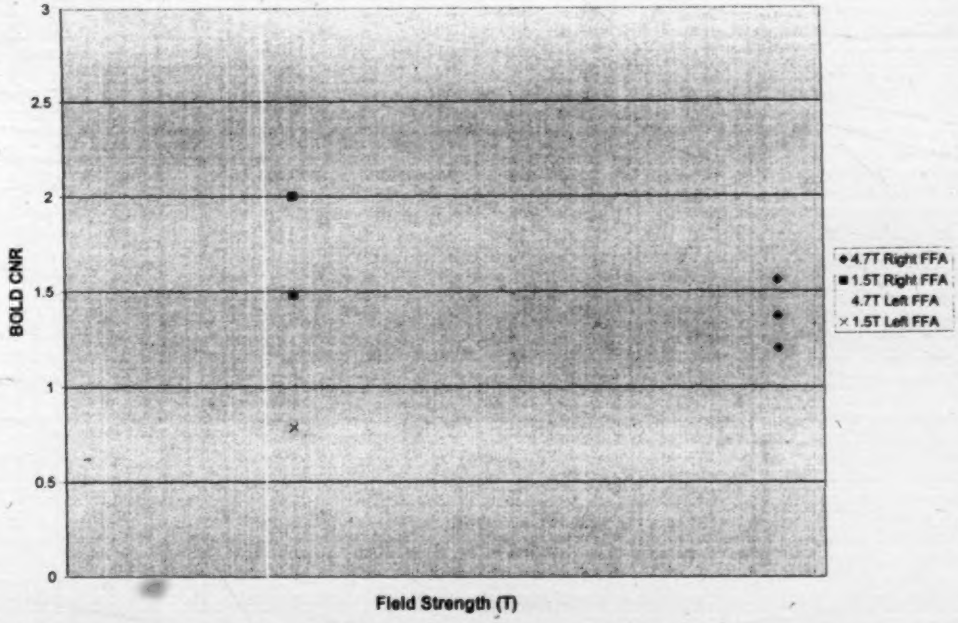

Figure 6.2.16: Scatter plot showing BOLD CNR in the right/left FFA across the 1.5T and 4.7T field strengths.

ΔR_2^* increased less than linearly in the right FFA and greater than linearly in the left FFA. As seen from
Table 6.2.17 and Table 6.2.18, the mean BOLD CNR was similar at both fields in the right FFA and increased greater than linearly in the left FFA at 4.7T, which once again indicates that the 1.5T and 4.7T results are not lateralized to the same hemisphere. The source of this discrepancy across the two fields is not known given that it can not be attributed to SNR differences across the two hemispheres (Table 6.2.13 and Table 6.2.14).

6.3 Discussion

6.3.1 Flashing checkerboard

The flashing checkerboard paradigm produced robust activation in the primary visual cortex. The ratio of average GRE BOLD signal change at 4.7T to 1.5T was 2.3 ± 0.7 across six subjects. This result is comparable to Gati [8] who measured an average GRE BOLD signal change ratio of 1.7 from 1.5T to 4T. In addition, the mean ΔR_2^* increased greater than linearly from 1.5T to 4.7T.

It has been predicted that SNR increases linearly with B_o (refer to section 3.4). Thus, SNR should increase by three folds at the higher field. However, in this study, the SNR gain was measured as roughly two-folds in the primary visual cortex at 4.7T.

The deviation from a linear model may be explained by first noting the RF field is more inhomogeneous at higher fields [4, 9]. Thus, standard power calibration methods across the imaging slab (using 1D projections) results in less than 90° and 180° flip angles (especially in brain peripheries) in transmission mode, and non-uniform signal intensity across the imaging region during reception mode (section 4.4.3). A surface coil can improve the sensitivity by coupling locally to the imaging region during receive mode. B_1 field mapping methods may also be employed to ensure 90° rotation in a local region during transmission. Gati [8] reported an SNR increase of 2.6 from 1.5T to 4T in fully-relaxed proton density weighted conventional GRE images using a T/R surface coil. Kruger [5] on the other hand measured an SNR increase of 1.7 in fully-relaxed GRE images from 1.5T to 3.0T which is less than the ideal two-fold increase with a standard head coil.

It is also important to consider magnetization and relaxation variations across fields for SNR considerations. At high field T_1 increases and T_2/T_2^* decreases. In regards to longitudinal relaxation, the repetition time of 3 seconds results in a full recovery of signal at 1.5T since $TR > 5T_1$ but not so at 4.7T due to a longer longitudinal relaxation. Finally, physiological noise which is the dominant noise source in fMRI studies (Jezzard '93) also scales with magnetic field due to greater susceptibility gradients caused by respiratory cycles for instance. The greater noise factor (physiological noise + thermal noise) may cause deviations in the predicted linear model of SNR with magnetic field.

Previous literature [8] predicts a greater than linear increase in maximum BOLD CNR with magnetic field in conventional GRE models. The actual BOLD CNR, using EPI images (with suboptimal SNR) increased up to linearly from 1.5T to 4.7T which shows the clear advantage of using high field fMRI for visual stimulation paradigms.

As observed in activation map figure, image quality is better in the superior parts of the brain. The image quality may be further improved by shimming locally on a small region (i.e. V1 region). It can thus be safely concluded that high field fMRI is not suitable for whole-head imaging and may not be used in novel fMRI studies where the activation region(s) is yet to be determined across the brain volume.

6.3.2 Verbal fluency task

The verbal fluency task produced dominant activation in the left inferior frontal lobe. The BOLD signal change in that region ranged from 1-4% and 1-2% at 4.7T and 1.5T respectively. The 1.5T system proved to be less sensitive to the BOLD signal (did not produce results for 50% of the subjects) as compared to the 4.7T system when similar imaging parameters and scan times were employed. Hinke [19] reported similar results (4%) using the FLASH sequence at 4T and Reuckert [10] measured a 2-6% change at 4T using the GRE-EPI sequence and a surface coil. The SE sequence produced comparable BOLD signal change to GRE for some subjects. However, due to noisy fMRI time-courses, it is suspected that the SE results have a large IV BOLD effect contribution, i.e. large veins, which is not desirable. The EV and IV BOLD components could not be separated in low resolution images.

In contrast to the primary visual cortex at the back of the head, the frontal lobe suffers from severe magnetic field inhomogeneity, due to its proximity to the nasal cavity, as evident in Table 6.2.6, Table 6.2.7 and Figure 6.2.8. Thus, the lower SNR relative to the primary visual cortex is attributed to intravoxel dephasing in the presence of large susceptibility gradients. The mean R_2^* contrast in the selected paradigm dropped relative to the primary visual cortex value. This is due to a reduction in echo time which compensates for SNR but reduces the EV BOLD effect. In regions such as the frontal lobe, the BOLD CNR is a compromise between SNR and the BOLD signal change. Even though the SNR measured in the activation region was lower than in the primary visual cortex (nonetheless higher than 1.5T values), the mean BOLD CNR increased across the two fields for most subjects. If the desired activation region involved the most anterior regions of the frontal lobe (Brodmann areas 9-11, Figure 6.1.1), which was not the case here with the selected verbal fluency paradigm, a gain in BOLD CNR would not be expected. Since BOLD CNR has dependencies on BOLD effect and SNR, it may not increase in areas with poor shim at high fields, unless *very* local shimming is employed.

6.3.3 Face Perception

More subjects showed the FFA activation at 4.7T than at 1.5T. This implies that even though FFA may not be identifiable in some subjects at 1.5T (due to the subtle nature of the paradigm), it may be so at higher fields. The BOLD signal change at 4.7T did not exceed the 1.5T results in the right FFA. The BOLD CNR was also variable across the two hemispheres with no gain in the right FFA and a greater than linear increase in the left FFA at 4.7T. No major conclusions can be made in regards to BOLD effect gains at 4.7T in this region however due to the variability of results. It is not certain why there is a disagreement in results across the two fields albeit the SNR measurements are identical across the two hemispheres (Table 6.2.13 and Table 6.2.14). The SNR measurements were comparable to the primary visual cortex in the fusiform gyrus region. The reduced TE (by 6ms) compensated for SNR loss which also indicates that the fusiform gyrus area does not suffer from as inhomogeneous field as the frontal lobe area. This is evident in the SNR calculations in Table 6.2.13 and Table 6.2.14 and image quality in Figure 6.2.13. The face perception results show that high field systems can be used in inferior brain regions for fMRI studies with relatively minor modifications to achieve an overall BOLD CNR gain.

6.4 Conclusions

The BOLD contrast to noise ratio is an important attribute which indicates the ultimate sensitivity, accuracy and statistical significance of fMRI results. Even though BOLD signal change increases with magnetic field, SNR may drop in some regions causing an overall BOLD CNR loss. The 4.7T system produced promising results for the three investigated brain regions in this thesis, indicating an overall gain in the BOLD CNR across the two fields. The 1.5T and spin-echo imaging protocols were not as sensitive to the BOLD signal as the 4.7T gradient-echo sequence which makes GRE the preferable fMRI tool at 4.7T. The good SNR achieved in the fusiform gyrus region is attributed to use of short echo times, thin slices and relatively small voxel dimensions. The relative SNR drop in the frontal lobe region (very inhomogeneous field) is attributed to the large susceptibility gradients in this region. The results presented here show that high field fMRI benefits from a higher BOLD CNR in homogeneous and inhomogeneous brain regions as long as the SNR losses are not severe. T_2^* variations and SNR loss may be minimized by very local shimming. As has been demonstrated here, high field fMRI is not suitable for whole-head imaging due to variable magnetic fields across the imaging region.

References

1. B. A. Poser, M. Barth, D. G. Norris, Evidence of functional activation in fusiform face area and amygdale using high-resolution single-shot GE-EPI at 7T, *ISMRM Workshop on Advances in High Field MR* (2007).

2. C. D. Frith, K. J. Friston, P. F. Liddle, R. S. J. Frackowiak, A PET study of word finding. *Neuropsychologia* **29**, 1137-1148 (1991).

3. C. G. Thomas, R. S. Menon, Amplitude response and stimulus presentation frequency response of human visual cortex using BOLD EPI at 4T. *Magn. Reson. Med.* **40**, 203-209 (1998).

4. D. L. Thomas, E. De Vita, S. Roberts, R. Turner, T. A. Yousry, R. J. Ordidge, High resolution Fast Spin Echo imaging of the human brain at 4.7T: Implementation and sequence characteristics. *Magn. Reson. Med.* **51**, 1254-1264 (2004).

5. G. Kruger, A. Kastrup, G. H. Glover, Neuroimaging at 1.5T and 3.0T: Comparison of oxygenation-sensitive magnetic resonance imaging. *Magn. Reson. Med.* **45**, 595-604 (2001).

6. I. L. Pykett, R. R. Rzedzian, Instant imaging of the body by magnetic resonance. *Magn. Reson. Med.* **5**, 563-571 (1987).

7. J. R. Binder, Functional magnetic resonance imaging of language cortex. *International Journal of Imaging Systems and Technology* **6**, 280-288 (1995).

8. J. S. Gati., R. S. Menon, K. Ugurbil, K. Rutt, Experimental determination of the BOLD field strength dependence in vessels and tissue. *Magn. Reson. Med.* **38**, 296-302 (1997).

9. J. T. Vaughan, M. Garwood, C. M. Collins, W. Liu, L. DelaBarre, G. Adriany, P. Andersen, H. Merkle, R. Goebel, M. B. Smith, K. Ugurbil, 7T vs. 4T: RF power, homogeneity, and signal-to-noise comparison in head images. *Magn. Reson. Med.* **46**, 24-30 (2001).

10. L. Rueckert, I. Appolonio, J. Grafman, P. Jezzard, R. Johnson, D. Le Bihan, R. Turner, Magnetic resonance imaging functional activation of left frontal cortex during covert word production. *J. Neuroimaging* **4**, 67-70 (1994).

11. M. C. Willson, A. H. Wilman, E. C. Bell, S. J. Asghar, P. H. Silverstone, Dextroamphetamine causes a change in regional brain activity in vivo during cognitive tasks: A functional magnetic resonance imaging study of blood oxygen level-dependent response. *Biol. Psychiatry* **56**, 284-291 (2004).

12. M. J. Silvennoinen, C. S. Clingman, X. Golay, R. A. Kauppinen, P. C. M. Van Zijl, Comparison of the dependence of blood R2 and R2* on oxygen saturation at 1.5 and 4.7 Tesla. *Magn. Reson. Med.* **49**, 47-60 (2003).

13. N. Kanwisher, G. Yovel, The fusiform face area: A cortical region specialized for the perception of faces. *Phil. Trans. R. Soc. B.* **361**, 2109-2128 (2006).

14. N. Kanwisher, J. McDermott, M. M. Chun, The fusiform face area: A module in human extrastriate cortex specialized for face perception, *J. Neuroscience* **17**, 4302-4311 (1997).

15. N. Kanwisher, M. M. Chun, J. McDermott, P. J. Ledden, Functional imaging of human visual recognition, *Cognitive Brain Research* **5**, 55-67 (1996).

16. P. Jezzard, S. Duewell, R. S. Balaban, MR relaxation times in human brain: Measurements at 4T. *Radiology* **201**, 637-648 (1996).

17. R. Cabeza, A. Kingstone, Handbook of Functional Neuroimaging of Cognition. Massachusetts Institute of Technology Cambridge, MA (2001).

18. R. K. Breger, A. A. Rimm, M. E. Fischer, R. A. Papke, V. H. Haughton, T1 and T2 measurements on a 1.5T commercial MR imager. *Radiology* **171**, 273-276 (1989).

19. R. M. Hinke, X. Hu, A. E. Stillman, S. G. Kim, H. Merkle, R. Salmi, K. Ugurbil, Functional magnetic resonance imaging of Broca's area during internal speech. *Neuroreport* **4**, 675-678 (1993).

20. R. S. Menon, S. Ogawa, D. W. Tank, K. Ugurbil, 4 Tesla gradient recalled echo characteristics of photic stimulation-induced signal changes in the human primary visual cortex. *Magn. Reson. Med.* **30**, 380-386 (1993).

21. R. Turner, P. Jezzard, H. Wen, K. K. Kwong, D. Le Bihan, T. Zeffiro, R. S. Balaban. Functional mapping of the human visual cortex at 4 and 1.5 Tesla using deoxygenation contrast EPI. *Magn. Reson. Med.* **29**, 227-229 (1993).

22. S. E. Peterson, P. T. Fox, M. I. Posner, M. Mintun, M. E. Raichle, Positron emission tomographic studies of the cortical anatomy of signal word processing. *Nature* **331**, 585-589 (1988).

23. S-G. Kim, J. Ashe, A. P. Georgopoulos, H. Merkle, J. M. Ellermann, R. S. Menon, S. Ogawa, K. Ugurbil, Functional imaging of human motor cortex at high magnetic field. *J. Neurophysiology* **69**, 297-302 (1993).

24. W. van der Zwagg, S. Francis, A. Peters, K. Head, P. Gowland, P. Morris, R. Bowtell, Field strength dependence of BOLD contrast in motor cortex. *ISMRM Workshop on Advances in High Field MR* (2007).

25. CVL FACE DATABASE, http://www.lrv.fri.uni-lj.si/facedb.html

7 Conclusions and Future Directions

This thesis explored echo planar imaging and its characteristics at 4.7T especially image artifacts such as ghosting, chemical shifting and geometric distortions. Even though there is intrinsic signal loss associated with fast sampling methods, EPI was investigated due to its fast acquisition speed which is absolutely necessary for functional studies. To get reasonable image quality, shimming is of paramount importance. FID shimming was performed in all experiments on the slices of interest using the PRESS sequence. It has been observed that second order shims are difficult to adjust using this procedure (across the slice) and may require field-mapping methods; even though the "current" field-mapping shim method on the Varian system is time-consuming and inadequate. In fMRI experiments presented here, the number of slices was limited to allow for good shimming. Shimming may be limited to a very small region to allow for more accurate water frequency adjustments and better image quality in that region. Very local regions are not desirable however for novel fMRI studies where the site of activation is yet to be determined across the brain volume.

To achieve the best feasible image quality with high field systems, it is important to pay close attention to key EPI parameters such as the sampling bandwidth, the phase-encoding direction, the voxel dimension as well as echo time. Hardware limitations (RF coils, shim and gradient coils) play a key role in EPI image quality and are important factors to consider when purchasing or upgrading an MRI system, especially if the main focus is functional MRI. In this thesis, only basic echo planar imaging reconstruction/image processing tools were developed. To correct for image distortions, especially in the frontal lobe area, the future course of action should be focused on developing more advanced software solutions. Of paramount importance is B_0 field mapping algorithms where "the distorted pixels can be relocated and intensity-corrected" [16] using a residual field map.

Image quality may further be improved by utilizing parallel imaging methods such as GRAPPA [15] to shorten the echo train length in single-shot EPI. SENSE [12] was initially tested on the 4.7T system; however, due to poor image quality, the presence of additional artifacts, i.e. unfolding residuals and the inability to obtain artifact-free reference scan, it was deemed inappropriate. K-space auto-calibration methods such as GRAPPA are more appropriate for echo planar images at high fields since they eliminate the need for the acquisition of a separate reference scan. Since the prism goggle did not fit inside the available four element coil, further investigation of parallel imaging for fMRI at this field strength was abandoned. With the availability of an open head coil, GRAPPA may be investigated.

Echo planar image quality especially in the language cortex may be improved by utilizing multi-shot methods [6, 7, 11], where the raw data is acquired with multiple, separate RF excitations. Although temporal resolution is reduced, multi-shot methods may be useful in frontal lobe areas where the signal drop is severe, and provide high resolution images (i.e. 128x128) not possible with single-shot methods. Limitations with multi-shot methods include amplitude and phase discontinuities across k-space and subject motion variations which in turn cause motion artifacts in functional maps. Asymmetric spin-echo (ASE) EPI [13] has also been utilized to improve image quality with a shifted refocusing pulse. The biggest downfall for ASE is reduced BOLD signal sensitivity due to different degrees of T_2 and T_2^* contrast. As another option, non-rectilinear k-space sampling methods such as spiral EPI [3, 8] may be developed on the Varian 4.7T system. Spiral EPI is more prone to signal blurring but less susceptible to image distortions. It however requires advanced hardware and software (reconstruction algorithms) developments and needs adequate commitment which was not possible here due to focus on single-shot EPI.

Since the 4.7T system had not been used previously for fMRI experiments, several hardware/software tools had to be installed and tested. First, a digital projection system was setup. The shielded T/R head coil used on the 4.7T system does not allow for a mirror system; therefore, a prism goggle was built to enable the subject to view the fMRI screen. The prism goggle caused some discomfort for the subjects as they were in the magnet for 40-55 minutes at times and had to tilt their head back to view the screen. In the future, the NMR lab may receive an open head coil which would allow for a mirror system. Fiber optic buttons were also setup to record subject responses. In addition, Estudio [18, 19] software was installed to program the fMRI paradigms. These initial setup steps were necessary to prepare the 4.7T system for future fMRI research. In addition, offline processing tools were developed for EPI image reconstruction and phase-correction. To utilize statistical fMRI software, additional tools were developed to convert the raw k-space data to the standard ANALYZE75 format.

Several echo planar imaging parameters, namely repetition (TR) and echo (TE) times were investigated and optimized for fMRI studies. Echo time is of key importance in maximizing the BOLD signal change between task and control conditions. For regions such as the frontal lobe that are in proximity of sinuses and nasal cavity however, the echo time has to be lowered to account for the more inhomogeneous field, and compensate for signal loss. This reduced echo time causes a reduction in BOLD sensitivity.

Previous literature has often portrayed high field fMRI as favorable in terms of BOLD CNR and SNR. In those studies however, the main focus was small homogeneous regions that do not suffer from poor EPI image quality and SNR. For the three brain regions investigate here (homogeneous and inhomogeneous regions), it was found that the BOLD CNR and SNR increased at the higher field. In the most anterior regions of the language cortex where the magnetic field is very inhomogeneous however, the SNR loss may be severe enough to predict no gain in BOLD CNR at 4.7T. The face perception results showed that high field may be used for higher cognitive studies in the inferior regions. The FFA area was identified in more subjects than at 1.5T which may help in identifying and comparing activation sites across field strengths. The spin echo sequence produces better image quality due to the refocusing pulse. However, the current results here have shown that spin-echo is not as sensitive to the EV BOLD signal as its gradient-echo counterpart at 4.7T and may either require longer scan times for statistical significance at this field strength or be employed in ultra-high fields.

Since most literature in high field fMRI has focused on classic paradigms such as simple photic stimulations, this thesis is the first of its kind to combine different cognitive tasks at high field to assess BOLD effect, SNR and image quality in broad regions of the brain. It has been observed here that high field systems are not suitable for whole-head fMRI imaging due to large magnetic field differences across the brain. Since relatively reasonable results were achieved here with standard imaging techniques, it is expected that high field systems will produce "superior" results to clinical 1.5T for studies that zoom in on a local brain region with minor modifications (i.e. very local shimming).

Even though high field fMRI may benefit from higher BOLD contrast in some areas of the brain (as was the case here), few publications have actually explored this possibility across different regions of the brain. Higher cognitive fMRI studies that for instance investigate the human ability to memorize information [1], experience reward or punishment [9] among others [2, 4, 10] should be explored to further evaluate BOLD sensitivity at 4.7T. The initial plan was to collaborate with the psychiatry department for clinical research to further evaluate fMRI at 4.7T. Even though this arrangement did not materialize, the future course of action should focus on collaborations with the medical community as the foundation for fMRI research at 4.7T has been laid in this thesis. Research areas such as drug treatment [14], stroke rehabilitation [17] and schizophrenia [5] would give further insights into the capabilities and limitations of high field fMRI and should be pursued.

References

1. A. M. Owen, Memory: Dissociating multiple memory processes. *Curr. Biol.* **8**, 850-852 (1998).

2. A. R. Hariri, A. Tessitore, V. S. Mattay, F. Fera, D. R. Weinberger, The Amygdala response to emotional stimuli: A comparison of faces and scenes. *NeuroImaging* **17**, 317-323 (2002).

3. C. B. Ahn, C. Y. Rew, J. H. Kim, O. Nalcioglu, Z. H. Cho, A new high speed spiral-scan echo planar (SEPI) NMR imaging. *Proc. Fourth Ann. Meeting SMRM*, London (1985).

4. C. Morawetz, C. Lange, P. Holz, J. Baudewig, G. Weniger, E. Irle, P. Dechent, Functional MRI of the human amygdala avoiding susceptibility artefacts. *ISMRM Workshop on Advances in High Field MR* (2007).

5. D. R. Weinberger, V. Mattay, J. Callicott, K. Kotrla, A. Santha, P. Van Gelderen, J. Duyn, C. Moonen, J. Frank., fMRI application in schizophrenia research, *NeuroImage* **4 (3 SUPPL. 2)**, S118-126 (1996).

6. F. Hennel, Multi-shot echo-planar imaging. *Concepts in Magn. Reson.* **9**, 43-58 (1997).

7. G. C. McKinnon, Ultrafast interleaved echo-planar imaging. *Magn. Reson. Med.* **30**, 609-616 (1993).

8. G. H. Glover, A. T. Lee, Motion artifacts in fMRI: Comparison of 2DFT with PR and spiral scan methods. *Magn. Reson. Med.* **33**, 624-635 (1995).

9. J. O'Doherty, M. L. Kringelbach, E. T. Rolls, J. Hornak, C. Andrews, Abstract award and punishment representations in human orbitofrontal cortex. *Nat. Neurosci.* **4**, 95-102 (2001).

10. J. R. Binder, K. A. McKiernan, M. E. Parsons, C. F. Westbury, E. T. Possing, J. N. Kaufman, L. Buchanan, Neural correlates of lexical access during visual word recognition. *J. Cogn. Neuroscience* **15**, 372-393 (2003).

11. K. Butts, S. J. Riederer, R. L. Ehman, R. M. Thompson, C. R. Jack, Interleaved EPI on a standard MRI system. *Magn. Reson. Med.* **31**, 67-72 (1994).

12. K. P. Pruessmann, M. Weiger, M. B. Scheidegger, P. Boesiger, SENSE: Sensitivity encoding for fast MRI. *Magn. Reson. Med.* **42**, 952-962 (1999).

13. L. A. Stables, R. P. Kennan, J. C. Gore, Asymmetric spin-echo imaging of magnetically inhomogeneous systems : theory, experiment, and numerical studies. *Magn. Reson. Med.* **40**, 432-442 (1998).

14. M. C. Willson, A. H. Wilman, E. C. Bell, S. J. Asghar, P. H. Silverstone, Dextroamphetamine causes a change in regional brain activity in vivo during cognitive tasks: A functional magnetic resonance imaging study of blood oxygen level-dependent response. *Biol. Psychiatry* **56**, 284-291 (2004).

15. M. A. Griswold, P. M. Jakob, R. M. Heidermann, M. Nittka, V. Jellus, J. Wang, B. Kiefer, A. Haase, Generalized autocalibrating partially parallel acquisitions (GRAPPA). *Magn. Reson. Med.* **47**, 1202-1210 (2002).

16. P. Jezzard, R. S. Balaban, Correction for geometric distortion in echo planar images from B_0 field variations. *Magn. Reson. Med.* **34**, 65-73 (1995).

17. R. Pineiro, S. Pendlebury, H. Johansen-Berg, P. M. Matthews, Functional MRI detects posterior shifts in primary sensorimotor cortex activation after stroke: Evidence of local adaptive reorganization? *Stroke* **32**, 1134-1139 (2001).

18. W. Schneider, A. Eschman, A. Zuccolotto. EPrime User's Guide. Psychology Software Tools Inc. Pittsburgh, USA (2002).

19. W. Schneider, A. Eschman, A. Zuccolotto. EPrime Reference Guide. Psychology Software Tools Inc. Pittsburgh, USA (2002).

Appendix A: EPI Reconstruction

Method 1: Nonlinear image reconstruction

```
function [recon krec] = img_con_v2(dirnm, par, ni, ni_t, np_t, nv_t, proc_mode)
%******************************img_con_v2***************************
%  Purpose:
%  Reconstructs Varian raw k-space data
%     Features: 1) multi-img, multi-slice, multi-receiver raw data
%               2) EPI and GEMS sequences
%               3) Phase-corrects EPI raw data
%               4) Partial-fourier reconstruction option (zerofill or
%               homodyne)
%
%  Usage: [recon krec] = img_con(dirnm, par, ni, ni_t, nv_t, proc_mode)
%
%  Calls several functions:
%  readprocpar
%  load_fid
%  img2ANA75
%
%  Input:
%  dirnm: directory name without the .fid extension
%  par: a Varian text file containing the imaging experiment parameters
%  ni: actual no. of images
%  ni_t: specified no. of images for output
%  np_t: specified no. of fe points for output
%  nv_t: specified no. of pe lines for output
%  proc_mode: 'z': zerofill, 'h': homodyne
%
%  Output:
%  seqfil: 'GEMS': reconstructed GEMS images/ANALYZE75 img, hdr files
%  seqfil: 'EPI':  reconstructed EPI images/phase-corrected k-space
%  data/ANALYZE75 img, hdr files
%
%  Written by: Farnaz Khosrow-Khavar April 2007
%  Nonlinear phase correction (same performance as Varian's processing)
%     Refer to Echo Planar Imaging Theory, Techniques and Application
%        by F. Schmitt, M.K. Stehling and R. Turner
%        Chapter 5, pp.167-168

%****************************Input*************************************
%  Check user inputs
```

```
if ~exist('par','var') || isempty(par)
   par = readprocpar(dirnm);
end

%  Adjust some parameters
ns = par.ns;
nv = par.nf/ns; %actual pe lines acquired
np = par.np/2;
nc = par.nrcvrs;
seqfil = par.seqfil;

if ~exist('ni','var')
   ni = 1;
end

if ~exist('ni_t','var')
   ni_t = ni;
end

%  Determine no. of desired pe lines
if ~exist('nv_t','var')
   nv_t = 2^nextpow2(nv);
end

if ~exist('np_t','var')
   np_t = np;
end

if ~exist('proc_mode','var')
   proc_mode = 'z';
end

%  Read the fid file
[kraw,hdr] = load_fid(dirnm);

%  DC correction
dc_lvl = hdr(17) + sqrt(-1)*hdr(18);
kraw = kraw - dc_lvl;

%***************Reconstruction and Phase Corrections*******************
if strcmp(seqfil(1),'g')

   GE = reshape(kraw, [nv ns np nc]);
   GE = permute(GE, [1 3 2 4]);

   krec = zeros(np,nv_t,ns,nc);
   krec(:,1:nv,:,:) = GE;
   recon = abs(ifftshift(ifft2(krec)));

   %  if the specified nv_t and np_t is greater than the acquired nv and
   %np, adjust par.nv and par.np parameters for the ANALYZE75 header files
   par.np = 2*np_t;
   par.nv = nv_t;
   %  convert to ANALYZE75 format
   img2ANA75(recon,ni_t,par)
```

```
    clear GE

elseif strcmp(seqfil(1),'e')

    EPI = reshape(kraw, [np nv size(kraw,2)/nv]);

    %  Reference scan -> first block (contains all slices)
    refl = EPI(:,:,1:nc*ns);
    kdata1 = EPI(:,:,1+nc*ns:size(EPI,3));

    clear EPI kraw  %free up memory

    refl = reshape(refl, [np nv nc ns]);
    kdata1 = reshape(kdata1, [np nv nc ns ni]);

    refl = permute(refl, [1 2 4 3]);
    kdata1 = permute(kdata1, [1 2 5 4 3]);

    %  Do phase-corrections on the acquired pe lines
    ref = refl;
    kdata(:,:,1:ni_t,:,:) = kdata1(:,:,1:ni_t,:,:);

    %  Sort even no. lines
    ref(:,2:2:nv,:,:) = refl((end:-1:1),2:2:nv,:,:);
    kdata(:,2:2:nv,1:ni_t,:,:) = kdata1((end:-1:1),2:2:nv,1:ni_t,:,:);

    clear refl kdata1

    % Allocate memory
    recon = zeros(np_t,nv_t,ni_t,ns,nc);
    krec = zeros(np_t,nv_t,ni_t,ns,nc);

    for nii = 1:ni_t,
        for nsi = 1:ns,
            for nci = 1:nc,
                k = kdata(:,:,nii,nsi,nci);
                %  FT the reference scan along the fe direction
                %  Obtain the phase for each pixel
                phase = angle(ifft(ref(:,:,nsi,nci),[],1));

                %  FT the k-space raw data along the pe direction
                  %  Subtract the phase calculated from the reference scan (pixel  by  pixel)
                k = ifft(k,[],1).*exp(-sqrt(-1)*phase);

                %  Back to k-space
                k = fft(k,[],1);

                %  homodyne partial-fourier reconstruction
                if strcmp(proc_mode,'h')
                    krec(:,:,nii,nsi,nci) = pifft2(k,2^nextpow2(nv),1);
                elseif strcmp(proc_mode,'z')
                    %  zerofill for partial fourier
                    krec(1:np,(2^nextpow2(nv)-nv)+1:2^nextpow2(nv),nii,nsi,nci) = k;
                    %  zerofill for smoothing (interpolation)
                    %krec(1:np,1:nv,nii,nsi,nci) = k;
                else
            error('processing mode is either "z" or "h" ')
          end

          %  Output
          recon(:,:,nii,nsi,nci) = abs(ifftshift(ifft2(krec(:,:,nii,nsi,nci))));

          %  Convert to ANALYZE75 format
          if nsi == ns,
            % modify nv if zerofill or homodyne && np if zerofill
            par.nv = nv_t;
            par.np = 2*np_t;
            % convert to ANALYZE75 format
            img2ANA75(recon(:,:,nii,:,nci),nii,par)
          end

          clear k phase
        end
      end
    end
    clear ref kdata
end

krec = squeeze(krec);
recon = squeeze(recon);
```

Method 2: Linear and constant image reconstruction

```
%**************************img_con_v1***************************
function [recon krec] = img_con_v1(dirnm, par, ni, ni_t, nv_t, proc_mode)
%
%  Purpose:
%  Reconstructs Varian raw k-space data
%     Features: 1) multi-img, multi-slice, multi-receiver raw data
%               2) EPI and GEMS sequences
%               3) Phase-corrects EPI raw data
%               4) Partial-fourier reconstruction option (zerofill or
%               homodyne)
%
%  Usage: [recon krec] = img_con(dirnm, par, ni, ni_t, nv_t, proc_mode)
%
%  Calls several functions:
%  readprocpar
%  load_fid
%  img2ANA75
%
%  Input:
%  dirnm: directory name without the .fid extension
%  par: a Varian text file containing the imaging experiment parameters
%  ni: actual no. of images
%  ni_t: specified no. of images for output
%  np_t: specified no. of fe points for output
%  nv_t: specified no. of pe lines for output
%  proc_mode: 'z': zerofill, 'h': homodyne
%
```

```
% Output:
% seqfil: 'GEMS': reconstructed GEMS images/ANALYZE75 img, hdr files
% seqfil: 'EPI': reconstructed EPI images/phase-corrected k-space
% data/ANALYZE75 img, hdr files
%
% Written by: Farnaz Khosrow-Khavar Feb 2007
% Modified code for linear phase correction April 2007
%    Originally shifted echoes physically in k-space
%    New version does does this as a phase correction
%    Refer to Echo Planar Imaging Theory, Techniques and Application
%       by F. Schmitt, M.K. Stehling and R. Turner
%       Chapter 5, pp.165-167

%**********************Input************************************
% Check user inputs
if ~exist('par','var') || isempty(par)
   par = readprocpar(dirnm);
end

% Adjust some parameters
ns = par.ns;
nv = par.nf/ns; %actual pe lines acquired
np = par.np/2;
nc = par.nrcvrs;
seqfil = par.seqfil;

if ~exist('ni','var')
   ni = 1;
end

if ~exist('ni_t','var')
   ni_t = ni;
end

% Determine no. of desired pe lines
if ~exist('nv_t','var')
   nv_t = 2^nextpow2(nv);
end

if ~exist('np_t','var')
   np_t = np;
end

if ~exist('proc_mode','var')
   proc_mode = 'z';
end

% Read the fid file
[kraw,hdr] = load_fid(dirnm);

% DC correction
dc_lvl = hdr(17) + sqrt(-1)*hdr(18);
kraw = kraw - dc_lvl;

% ****************Reconstruction and Phase Corrections*******************
tic; % Start the timer
```

```
if strcmp(seqfil(1),'g')

   GE = reshape(kraw, [nv ns np nc]);
   GE = permute(GE, [1 3 2 4]);

   krec = zeros(np,nv_t,ns,nc);
   krec(:,1:nv,:,:) = GE;
   recon = abs(ifftshift(ifft2(krec)));

   % if the specified nv_t and np_t is greater than the acquired nv and
   %np, adjust par.nv and par.np parameters for the ANALYZE75 header files
   par.np = 2*np_t;
   par.nv = nv_t;
   % convert to ANALYZE75 format
   img2ANA75(recon,ni_t,par)

   clear GE

elseif strcmp(seqfil(1),'e')

   EPI = reshape(kraw, [np nv size(kraw,2)/nv]);

   % Reference scan -> first block (contains all slices)
   refl = EPI(:,:,1:nc*ns);
   kdata1 = EPI(:,:,1+nc*ns:size(EPI,3));

   clear EPI kraw %free up memory

   refl = reshape(refl, [np nv nc ns]);
   kdata1 = reshape(kdata1, [np nv nc ns ni]);

   refl = permute(refl, [1 2 4 3]);
   kdata1 = permute(kdata1, [1 2 5 4 3]);

   % Do phase-corrections on the acquired pe lines
   ref = refl;
   kdata(:,:,1:ni_t,:,:) = kdata1(:,:,1:ni_t,:,:);

   % Sort even no. lines
   ref(:,2:2:nv,:,:) = refl((end:-1:1),2:2:nv,:,:);
   kdata(:,2:2:nv,1:ni_t,:,:) = kdata1((end:-1:1),2:2:nv,1:ni_t,:,:);

   clear refl kdata1

   % Allocate memory
   recon = zeros(np_t,nv_t,ni_t,ns,nc);
   krec = zeros(np_t,nv_t,ni_t,ns,nc);

   for nii = 1:ni_t,
      for nsi = 1:ns,
         for nci= 1:nc,
            k = kdata(:,:,nii,nsi,nci);
            % peakloc_fe: echo peak along fe direction
            % peakloc_pe: highest intensity peak of all k-space
            [max_fe peakloc_fe] = max(abs(ref(:,:,nsi,nci)),[],1);
```

```
                [max_pe peakloc_pe] = max(max_fe);
                phase_lin = peakloc_fe(peakloc_pe) - peakloc_fe;

                %  FT the reference scan along the fe direction
                %  Obtain the phase for echo peaks
                for cols=1:nv,
                    phase_const(1,cols) = angle(ifft(ref(peakloc_fe(cols),cols,nsi,nci),[],1));
                end

                %  Do a constant and linear phase correction to the projections along fe direction
                k = ifft(k,[],1);
                for cols = 1:nv,
                    k(:,cols) = k(:,cols)*exp(-sqrt(-1)*phase_lin(cols))*exp(-sqrt(-1)*phase_const(cols));
                end

                %  Back to k-space
                k = fft(k,[],1);

                %  homodyne partial-fourier reconstruction
                if strcmp(proc_mode,'h')
                    krec(:,:,nii,nsi,nci) = pifft2(k,2^nextpow2(nv),1);
                elseif strcmp(proc_mode,'z')
                    %  zerofill for partial fourier
                    krec(1:np,(2^nextpow2(nv)-nv)+1:2^nextpow2(nv),nii,nsi,nci) = k;
                    %  zerofill for smoothing (interpolation)
                    %krec(1:np,1:nv,nii,nsi,nci) = k;
                else
                    error('processing mode is either "z" or "h" ')
                end

                %  Output
                recon(:,:,nii,nsi,nci) = abs(ifftshift(ifft2(krec(:,:,nii,nsi,nci))));

                %  Convert to ANALYZE75 format
                if nsi == ns,
                    % modify nv if zerofill or homodyne && np if zerofill
                    par.nv = nv_t;
                    par.np = 2*np_t;
                    % convert to ANALYZE75 format
                    img2ANA75(recon(:,:,nii,:,nci),nii,par)
                end

                clear max_fe max_pe peakloc_fe peakloc_pe phase_lin phase_con k
            end
        end
    end

    clear ref kdata
end
```

Appendix B: File conversions

```
%*******************img2ANA75**********************************
% Purpose: Converts .mat image file to ANALYZE75 format
%
% Usage: img2ANA75(img, imno, par)
%
% Calls several functions:
% avw_hdr_make
% avw_img_write
%
% Input:
% img: image (in .mat format)
% imno: image no.
% par
%
% Written by: Farnaz Khosrow-Khavar Feb 2007

function img2ANA75(img, imno, par)

% Check user inputs
if ~exist('par','var') || isempty(par)
   error('Must input the par variable')
end

if ~exist('imno','var')
   imno = 1;
end

if ~exist('img','var')
   error('Must input the image data for conversion to ANALYZE format')
end

img = squeeze(img);

% .hdr file parameter adjustments
np = par.np/2;
nv = par.nv;
ns = par.ns;
ro_vox = par.lro * 10 / np;
pe_vox = par.lpe * 10 / nv;
thk = par.thk;

% Make the .hdr file
avw = avw_hdr_make(ro_vox,pe_vox,thk,np,nv,ns);
```

```
% Make the .img file
avw.img = img;
filenm = sprintf('img%03d', imno);
avw_img_write(avw, filenm, 0, 'ieee-be', 0);

clear avw.img filenm img
```

Appendix C: fMRI paradigms

Flashing checkerboard

```
a = [0 1;1 0];
b = [1 0;0 1];

c = zeros(64,64);

d = zeros(64,64);
d(28:36,32) = 1;
d(32,28:36) = 1;

e = repmat(a,4,4);
f = repmat(b,4,4);

%   Gray Screen
imagesc(c)
colormap gray
M(1) = getframe;

%   Black screen with white cross in the center
imagesc(d)
colormap gray
M(2) = getframe;

%   Flashing Checkerboard
imagesc(e)
M(3) = getframe;

imagesc(f)
M(4) = getframe;

%Create the video file
aviobj = avifile('check_530.avi','fps',8,'quality',100);

%   To synchronize the 4.7T scanner with the visual presentation
%   Insert a gray screen for 30 sec
for i = 1:240,
   aviobj = addframe(aviobj,M(1));
end

%Checkerboard Paradigm
```

```
for blocks = 1:5,
   for i=1:120,
      aviobj = addframe(aviobj,[M(3) M(4)]);
   end

   for i=1:240,
      aviobj = addframe(aviobj,M(2));
   end
end
aviobj = close(aviobj);
```

Face perception

```
warning('off')
%Create the video file
aviobj = avifile('face_perc2.avi','fps',1,'quality',100);

white_fr = zeros(64,64);
imagesc(white_fr,[0 1]); colormap gray
M = getframe();
for i = 1:16,
   aviobj=addframe(aviobj,M);
end

gray_fr = ones(64,64);
imagesc(gray_fr,[0 1]); colormap gray
M = getframe();
for i = 1:15,
   aviobj=addframe(aviobj,M);
end

filename1 = 'D:\face perception preliminary\face database\Face DB\database';
filename2 = 'D:\face perception preliminary\face database\Object-Face DB\MANMADE\IMAGES';
filename3 = 'D:\face perception preliminary\face database\obj\image';

facefile_index=1;
objfile_index=1;
block_cyc=1;
while (block_cyc <= 6)
   %first block the same as fourth block
   if block_cyc == 4,
      facefile_index=1;
   end
   %second block the same as fifth block
   if block_cyc == 5,
      facefile_index=31;
   end
   %third block the same as sixth block
   if block_cyc == 6,
      facefile_index=62;
   end
   % face viewing block
   % 1 photograph per second
   % 30 sec block
   for i = 1:30,
      face_file = sprintf('%s%c%01d%c%s',filename1,'\',facefile_index,'\','MVC-003F');
      face_ph = imread(face_file,'JPG');
      % convert to gray scale
      face_ph = 0.299*face_ph(:,:,1) + 0.587*face_ph(:,:,2) + 0.144*face_ph(:,:,3);
      imagesc(face_ph)
      M = getframe;
      aviobj=addframe(aviobj,M);
      facefile_index=facefile_index+1;
   end

   % object viewing block
   % 1 photograph per second
   % 20 sec block
   for i = 1:10,
      obj_file1 = sprintf('%s%c%03d%c%c',filename2,'\',objfile_index,'.','i');
      obj_file2 = sprintf('%s%c%04d',filename3,'_',objfile_index);
      obj_ph1 = imread(obj_file1,'gif');
      obj_ph2 = imread(obj_file2,'JPG');
      obj_ph2 = 0.299*obj_ph2(:,:,1) + 0.587*obj_ph2(:,:,2) + 0.144*obj_ph2(:,:,3);
      imagesc(obj_ph1)
      M(1) = getframe;
      imagesc(obj_ph2)
      M(2) = getframe;
      aviobj=addframe(aviobj,[M(1) M(2)]);
      objfile_index=objfile_index+1;
   end
   block_cyc=block_cyc+1;
end

aviobj=close(aviobj);
```

Appendix D: BOLD signal change calculations

```
function pc = percent_change(e,e_dur)

%Purpose: To calculate BOLD signal percentage change using MARSBAR toolbox
%Usage: pc = percent_change(e,e_dur)
%Inputs:
%   e --> time_courses variable
%   e_duration --> fMRI time-course scan time (in sec)

%Note: BOLD percentage change is the average response of the plateau
%portion of the HRF, 8 secs after stimulus onset to stimulus termintation.

plot(e{1,1})
ind = find(e{1,1} == median(e{1,1}));
scale_f = floor(size(e{1,1},1)/e_dur);
pc = mean(e{1,1}(8*scale_f:ind(end)));
```